

# POLITECNICO DI TORINO

**Master degree  
in civil engineering**

**Master's degree thesis**

**Structural Health Monitoring of civil engineering construction with an  
innovative device**



Supervisor

*prof. Francesco Tondolo*

*Eng. Pierclaudio Savino*

Candidate

*Luca Delle Castelle*

Academic year 2021/2022



# Contents

<b>Table of figures</b>	<b>III</b>
<b>Table of table</b>	<b>V</b>
<b>Abstract</b>	<b>1</b>
<b>Introduction</b>	<b>2</b>
<b>Chapter 1</b>	<b>3</b>
<b>1. Structural Health monitoring in civil engineering</b>	<b>3</b>
1.1. Choose of the best strategy for SHM	4
1.1. Non-destructive method	5
1.1.1. Acoustic method	5
1.1.2. Electromagnetic method: Ground Penetration Radar ( <i>GDR</i> )	6
1.1.3. Optical method	7
1.2. Classical devices for <i>SHM</i>	7
1.2.1. Metallic Strain Gauges	7
1.2.2. Linear Variable Differential Transducer ( <i>LVDT</i> )	9
1.2.3. Accelerometers	10
1.2.4. Wireless vibrating wire system	12
1.3. Fibre Optic System ( <i>FOS</i> )	13
1.3.1. <i>SOFO</i>	14
1.3.2. Fabry – Perot interferometric sensor	14
1.3.3. Fibre Bragg Grating Sensor	15
1.3.4. Distributed sensor	17
1.4. Innovation with piezoelectric sensor in <i>SHM</i>	19
1.4.1. Smart aggregate in a steel fibre concrete specimen	19
1.4.2. Doped concrete with Carbon Nanotube for <i>SHM</i>	20
1.4.3. Piezoelectric sensor embedded into steel rebars	21
1.5. Sensitivity	23
1.5.1. Strain gauge	24
1.5.2. Fibre optic system ( <i>SOFO</i> )	25
1.5.3. Fibre optic system (Smartfibres)	26
<b>Chapter 2</b>	<b>28</b>
<b>2. Smart Steel System</b>	<b>28</b>
2.1. Explanation of the type of innovation	28
2.2. Difference with the standard devices	28
2.3. Progress during the study	30
2.4. Sensitivity of S3	36
2.5. Comparison between the sensitivities	39
<b>Chapter 3</b>	<b>41</b>
<b>3. Case study</b>	<b>41</b>
3.1. Description of the bridge	41
3.2. Installation phase	42
<b>Chapter 4</b>	<b>46</b>
<b>4. Experimental phase</b>	<b>46</b>

4.1.	Mechanical characterization of the instrumented rebars _____	46
4.2.	Monitoring of the instrumented rebar in the bridge _____	57
4.3.	Finite Element Model _____	62
4.4.	Application of the structural and non-structural loads _____	69
4.4.1.	Self-weight and reinforcement rebar load _____	69
4.4.2.	Curbs _____	69
4.4.3.	Barriers _____	70
4.4.4.	Binder _____	70
4.4.5.	Wearing layer _____	70
4.5.	Short and long term effects _____	71
4.6.	Geometrical characteristics _____	76
4.7.	Analysis of the results from the model _____	79
4.7.1.	Evaluation of the model _____	79
4.8.	Determination of the solicitation and stresses _____	80
4.8.1.	Self-weight and reinforcement _____	81
4.8.2.	Short and long term effects _____	82
4.8.3.	Curb load-case _____	85
4.8.4.	Barrier load-case _____	87
4.8.5.	Binder load-case _____	89
4.8.6.	Wear layer load-case _____	90
4.9.	Application of traffic loads _____	91
4.9.1.	Four trucks load-case _____	91
4.9.2.	Car Load-case _____	93
<b>Chapter 5</b> _____		<b>96</b>
<b>5. Conclusions</b> _____		<b>96</b>
<b>References</b> _____		<b>98</b>

## Table of figures

Figure 1.1: The principle of a) ultrasonic pulse velocity; b) impact echo; c) acoustic emission (Zaki et al., 2015)	6
Figure 1.2: Scheme of the metallic foil [5]	8
Figure 1.3: Wheatstone Bridge	8
Figure 1.4: Scheme of a LVDT [8]	10
Figure 1.5: Scheme of a piezoelectric capacitor [7]	10
Figure 1.6: Scheme of a capacitive piezometer [7]	11
Figure 1.7: Scheme of a force balanced accelerometer (Enckell, 2006)	11
Figure 1.8: Vibrating Wire System [9]	12
Figure 1.9: Scheme of SOFO [11]	14
Figure 1.10: Scheme of a FP interferometric sensor [12]	15
Figure 1.11: Fibre Bragg Grating Scheme [13]	16
Figure 1.12: a) Smart Patch; b) Smart Rebar (Corvaglia, et al., 2010) [15]	16
Figure 1.13: Functioning of a DFOS [16]	17
Figure 1.14: Structure of the DFOS used in the experiment [17]	18
Figure 1.15: Rebar grooved for the implementation of the FOS (Quiertant, et al., 2012)	18
Figure 1.16: Smart Aggregate Composition (Wang, et all. , 2018)	19
Figure 1.17: Spring-mass-dumper EMI measurement [18]	20
Figure 1.18: Procedure for the preparation of a sample with MWCNTs [14]	20
Figure 1.19: Schematization of a steel reinforced bar with the application of a PZT sensor [15]	22
Figure 2.1: Axis of the cavity [12]	33
Figure 2.2: Elliptical and slotted hollow comparing [12]	33
Figure 2.3: Comparison of the different models studied [12]	34
Figure 2.4: Comparison of pressure recorded by the MEMS with an increasing percentage of fluid in the cavity [12]	35
Figure 2.5: Dimension of the cavity [6]	38
Figure 3.1: Photo of the bridge where the application is carried out	41
Figure 3.2: Image of the scheme of the deck of the bridge	42
Figure 3.3 Data logger used in the application	43
Figure 3.4 Reinforcement displaced in the slab	43
Figure 3.5 Longitudinal beam number one	44
Figure 3.6: Position of the instrumented rebar with respect to the reinforcement	45
Figure 3.7: Position of the data logger with respect to the instrumented rebars	45
Figure 4.1 Hydraulic machine used for the tensile test	47
Figure 4.2 Full equipment used to perform the test on the rebars	47
Figure 4.3 Detail of the rebars undergoing to the test	48
Figure 4.4: Sensor 11 in position 2 in rebar 2	49
Figure 4.5: Sensor 14 in position 3 in rebar 2	49
Figure 4.6: Sensor 2 in position 4 in rebar 2	50
Figure 4.7: Sensor 5 in position 5 in rebar 2	50
Figure 4.8: Sensor 7 in position 1 in rebar 2	51
Figure 4.9: Sensor 7 in position 1 on rebar 2	51
Figure 4.10: Sensor 11 on position 2 in rebar 2	52
Figure 4.11: Sensor 14 in position 3 in rebar 2	52
Figure 4.12: Sensor 2 in position 4 in rebar 2	53
Figure 4.13: Sensor 5 in position 5 in rebar 2	53
Figure 4.14: Monitoring of pressure of the rebar number 2	55
Figure 4.15: Final trend of the sensors 2, 11, 14	56
Figure 4.16: Monitoring of temperature of the rebar number 2	56
Figure 4.17: Monitoring of pressure before the installation	57
Figure 4.18: Monitoring of pressure before the installation	58
Figure 4.19: Monitoring of pressure after the installation in the construction site	59
Figure 4.20: Monitoring of temperature after the installation in the construction site	59

Figure 4.21: Monitoring in pressure after the concrete casting	60
Figure 4.22: Average temperature per instrumented rebar;	61
Figure 4.23 Reference axis of the deck	62
Figure 4.24 Cross section of the longitudinal beams	63
Figure 4.25 Cross section of the transverse beams	63
Figure 4.26: Cross section of the edge transverse beam	63
Figure 4.27 Modelling of the main structure of the bridge	64
Figure 4.28: Modelling of the slab	64
Figure 4.29: Modelling of the constrains	65
Figure 4.30: Transverse scheme of the deck	65
Figure 4.31: Points where the sensors are displaced	68
Figure 4.32: Self-weight and reinforcement	69
Figure 4.33: Right curb	69
Figure 4.34: Left curb	69
Figure 4.35: Right barrier	70
Figure 4.36: Left barrier	70
Figure 4.37: Binder	70
Figure 4.38: Wear layer	70
Figure 4.39: Cross section considered for the calculation of the loads	71
Figure 4.40: Definition of the coefficient $kh$	72
Figure 4.41: Cross-section of the single beam	79
Figure 4.42: Deformation in correspondence of the beam	80
Figure 4.43: Diagram of moment [kNm] expected with self-weight of the slab and the reinforcement displaced	81
Figure 4.44: Stresses in the instrumented rebars	83
Figure 4.45: Right curb load-case	85
Figure 4.46: Left curb load-case	85
Figure 4.48: Right barrier load-case	87
Figure 4.49: Left barrier load-case	87
Figure 4.51: Binder load-case	89
Figure 4.53: Wear layer load-case	90
Figure 4.55: Static load of the trucks	91
Figure 4.58: Scheme of the application of the car load	93
Figure 4.59: Moment generated by the car on the structure	94

## Table of table

Table 1.1: Characteristics of the MWCNTs [14]	21
Table 1.2: Characteristics of the Strain Gauges	24
Table 1.3: Performance of the Smart Patch [16]	26
Table 1.4: Performance of the Smart FBG [17]	27
Table 2.1: Characteristics of the digital barometric air pressure sensor	37
Table 2.2: Sensitivity comparison	39
Table 4.1: Summary of the tensile test in the rebar number 2	54
Table 4.2 Structural material used in the calculations	66
Table 4.3: Non-structural material used in the calculation	66
Table 4.4: Geometry of the deck	66
Table 4.5: Permanent load applied to the structure	67
Table 4.6: Static traffic load	67
Table 4.7: Load applied to the model	68
Table 4.8 Long and short term effects	72
Table 4.9: Creep values	74
Table 4.10: Shrinkage values	76
Table 4.11: Table of the first load-case	81
Table 4.12: Stress expected at the interface in between the longitudinal beams and the slab	82
Table 4.13 Strain expected at the interface in between the longitudinal beams and the slab	82
Table 4.14: Value at one day of the casting of the concrete	82
Table 4.15: Stress and strain due to shrinkage at 1 day in beam 23	84
Table 4.16: Stress and strain due to shrinkage at 1 day in beam 64	84
Table 4.17: Stress and strain due to shrinkage at 16 day in beam 23	85
Table 4.18: Stress and strain due to shrinkage at 16 day in beam 64	85
Table 4.19 Right curb load moment	85
Table 4.20 Left curb load moment	86
Table 4.21: Stress and strain generated by the right curb on beam 23	86
Table 4.22: Stress and strain generated by the right curb on beam 64	86
Table 4.23: Stress and strain generated by the left curb on beam 23	86
Table 4.24: Stress and strain generated by the left curb on beam 64	87
Table 4.28 Right curb load moment	87
Table 4.29 Left curb load moment	88
Table 4.30: Right barrier stresses and strains on beam 23	88
Table 4.31: Right barrier stresses and strains on beam 64	88
Table 4.32: Left barrier stresses and strains on beam 23	88
Table 4.33: Left barrier stresses and strains on beam 64	88
Table 4.37 Binder load moment	89
Table 4.38: Binder stresses and strains on beam 23	89
Table 4.39: Binder stresses and strains on beam 64	89
Table 4.43 Wear layer load moment	90
Table 4.44: Wear layer stresses and strains on beam 23	90
Table 4.45: Wear layer stresses and strains on beam 64	90
Table 4.49: Moment generated by the static load of four trucks	91
Table 4.50: Stresses and strain generated on the beam number 23	92
Table 4.51: Stresses and strain generated on the beam number 64	92
Table 4.52: Moment acting on the two beams considered from the moving load	94
Table 4.53: Car load-case stresses and strain on beam 23	94
Table 4.54: Car load-case stresses and strain on beam 64	94



# Abstract

In this thesis will be treated one of the key points of innovation in the structure these days. Structural Health Monitoring has had an exponential increase in the evaluation of deformation, stresses, and remaining life of the structure. In particular, a new branch of this field is dedicated to innovation and to different methods that can increase the efficiency in the collection of data from new or existing structures and convert this into forecasts for the performance of the buildings. This paper will focus in particular on one of them which is a new device called Smart Steel System (S3) (Tondolo, 2016) that is a low cost-high performance device able to convert local variations into the evaluation of stress and deformation of the structure. These elements consist of a Micro Electro-Mechanic System installed into a cavity dig into the rebars dislocated in the reinforcement of a reinforced concrete element. This system through the evaluation of the variation of pressure and temperature, using the simple ideal gas law, is able to convert these values into strain deformations, obtaining the state of stress and solicitations from them. A comparison between the different innovative systems for monitoring will be discussed in the first chapter, followed by comparison of the sensitivity of the principal systems alongside the S3. After an experimental phase, the new system has been evaluated through a tensile test where the improvements have been classified and paired with the previous analysis (Battistoni, 2018; Bandinelli, 2020). The application of the technology in a real structure has been carried out on a bridge in order to have data from the monitoring that will be helpful in the development of this technology but also to understand the progress made up to this moment. To quantify the data collected a model has been realised in order to evaluate the stresses and deformation that the construction phases of the bridge will produce on the structure. This has been helpful to understand the potential of the technology and to compare the results with the sensitivity calculated in the first paragraphs. Furthermore, it has been tested the model with loads come from a vehicle in two conditions obtain the expected strain and in order to evaluate the efficiency of the model in the cases evaluated.

# Introduction

Deterioration, damaging, deformation of the structures in civil engineering are part of the service life of any building. Service loads, sudden horizontal loads as an earthquake, corrosion, fatigue cycles are just some of the effects that a construction needs to bear under its entire life. The task of an engineer is to design the structure in order to withstand to these effects. Although the degradation of the structure is something natural that happen during the years. For this reason, each building needs to be in constant monitoring during and after the ultimation of the construction. In this scenario, Structural Health Monitoring (SHM) founds its roots.

In the field of civil engineering, a big challenge for the constructions have always been the control of the deformation and the stress in order to programme the maintenance and avoid the collapse of the structure. During the history, several instruments have been developed in order to accomplish to this task. SHM is a technology which is developing in the recent years that involves the use of devices to continuously monitoring the structure and obtain the information about the response of the structure during its entire life.

SHM is an important tool that need to be used nowadays in every field of engineering. In fact, there are a lot of sources that demonstrate applications in aerospace, mechanical and many other fields in engineering. In civil engineering it is mainly used for the evaluation of the state of fact of the infrastructures, such as bridges, buildings, dams, retaining structures and so on. The principle of work of SHM is the acquisition of data from a structure in order to quantify and state the integrity of a structure.

Nowadays, SHM is being developed and improved through the utilization of new technologies that aims to improve the local and global detection of the integrity of a structure. These technologies have been implemented by using sensor and devices that can be applied on the surfaces or embedded in the sections of the elements (embedded elements). In this paper, an innovative concept of sensor is discussed, called Smart Steel System (S3) [1], providing a cheap, robust and durable strain-measurement device. The S3 is an embedded system able to calculate constantly the response in terms of strain of new and existing structure. In this paper it will be treated the application of this technology in a practical case. In particular, the technology will be tested in a bridge in order to understand the expected stresses and strain that will be obtained from the application of the structural and life load. It will be discussed about the feature and characteristics of the devise and compared the result with the most diffused technology for the monitoring of a structure

# Chapter 1

## 1. Structural Health monitoring in civil engineering

The evaluation of the integrity of a structure in civil engineering has been taken more importance in the recent years. The possibility of having a solution that can continuously monitor the response of the infrastructures that every day serve millions of people gives to the experts the ability of understanding what is the response and how far is the end of the service life. Structural Health Monitoring is a source that allows the acknowledge of the current state of degradation of the structure in order to prevent sudden failures.

In the beginning, SHM was based on methodologies that used visual inspection in order to verify the damages that occurred to a specific structure after a particular event. With the years, SHM have been developed in a direction which aims to the construction of smart buildings, with the possibility of reading data and monitoring possible unexpected deterioration or deformation of the structure. The main problems to be solved in order to encourage the construction of smart structures are the high cost that the different technologies have to face to be implemented in the structure and the difficult application that some systems required.

The aim of SHM is the use of a mix of hardware and software that helps the evaluation of damages and irregularities of the structure with the purpose of monitoring the response and the reliability of each element and estimate the remaining service life of the construction. SHM is developed following some specific principles regarding the identifications of the damage. In particular there are five levels which describes with an increasing degree of acknowledge the state of the construction [2]. In particular it is possible to identify:

- Level 1, Level I: Damage detection, giving a qualitative indication that damage might be present in the structure;
- Level II: Damage localisation, giving information about the probable position of damage;
- Level III: Damage classification, giving information about the type of damage;

- Level IV: Damage assessment, giving an estimate of the extent of damage;
- Level V: Damage prognosis, giving information about the safety of the structure, e.g. estimate of remaining useful life.

Historically, SHM has been used since the early 80s, where there was an interest of the application of a monitoring programme in order to evaluate the health of offshore platforms and aerospace structures. During those years, in the civil engineering field there has been developed methods based on the vibration in order to investigate on infrastructure and provides modal properties and dynamic indices. With the implementation of the equipment, other properties have been monitored such the environmental and operational conditions. The technology enhancement also corresponded to an increase of SHM application costs. The goal is to develop new cost-effective devices that can be implemented in every structure [2].

SHM consists in a series of actions able to identify different common properties from which is possible to retrieve the estimation of the structure's health. The large is the infrastructure the high is the number of variables and properties that need to be evaluated. The general procedure that describes a common SHM of a structure is differentiated in 4 different steps that can be classified in: *observation*, collection of data from the structure, *evaluation*, monitoring of the structure executed in real time or quasi real time, *rating*, ranking of the health of the structure and classification of the action that occur, and *management*, processing of the data collected to perform an analysis and programme an intervention on the structure [2].

The classification of action showed above is carried out with different tools that go from the simple visual inspection to the characterization of a specific properties of the structures. According to the goal of the observation we can distinguish devices depending on the quantity that it possible to record with and the specific purpose for which it is designed for.

The sensors have the possibility to detect quantities such as acceleration, velocity, displacement, strain, stresses, and other physical quantities. There are some other that are referred to the environmental behaviour and these are corrosion, wind, temperature, pressure, moisture. All of these quantities have been registered with the goal of monitoring the structure. In particular, if the quantities are recorded to evaluate the damage in a small part of the structure it is called local monitoring; on the other hand, if the monitoring is performed on the entire structure, it is a global monitoring.

### 1.1. Choose of the best strategy for SHM

The purpose of the analysis is a concept of absolute important to understand the methodology of the evaluation of the integrity of the structure. Typology, state, and integrity of the monitored element must be considered to select the optimal tools to carry out the SHM. As first consideration it is possible to distinguish different families of method of evaluation that are related to the approach to the structure considered.

The Non Destructive Evaluation (NDE) is the first procedure addressed in this thesis. It has been largely used from the 19<sup>th</sup> century onwards and its purpose was the assessment of the quality and integrity of the structure. This method, as the name suggests, imply a sequence of operation, that will not affect the damaging of any portion of the element tested. In fact, this method is mainly used to obtain coefficients that attests the integrity of the structure and can help to identify the remaining life of it. Among this method it is possible to distinguish:

- Acoustic methods, which through the propagation of waves are able to detect discontinuities and evaluate the acoustic resonant frequencies;
- Electromagnetic methods, that concerns the propagation of waves in a dielectric material carried out through instruments as radar, antenna;
- Optical method, all the methods that involves the use of images, impulses, laser which are able to obtain the conservation state and geometry of the structure.

## 1.1. Non-destructive method

### 1.1.1. Acoustic method

The method of acoustic emission is mainly used in civil engineering for the evaluation of presence of cracks and damages inside the structure. This problem can usually be the results of presence of corrosion and may lead to a further development of the cracks and a failure of the element. Corrosion is one of the principal causes of failure in Reinforced Concrete (*RC*) and can easily provoke a trigger to a crack that will develop into a failure if subjected to external loading if it is not reported on time. Elastic wave method is one of the best methods to individuate these defects and report them in time. In particular, this NDE comprehend 3 different but similar approaches. It is possible, in fact, to distinguish:

- Ultrasonic Speed Velocity (*UPV*), in which steel corrosion is evaluated through the calculation of the speed of sound into a member of RC. This is a quite sensitive method and it is possible to report the presence of a possible trigger point of corrosion if it is recorder an *UPV* attenuated;
- Stress Wave Method (*IE*), is a slightly different method which imply the application of an external force and it is able to evaluate deformation and strain by considering the repulse of the wave when it encounters a discontinuity;
- Acoustic Emission, an intersection between *UPV* an *IE* and the best option for revealing the presence of a crack due to corrosion; *AE* is a totally non-intrusive method, widely use in field of civil engineering, that imply the usage of a piezoelectric material (*PZT*) which is able to convert the energy variation generated by the presence of a crack or a discontinuity into a signal;

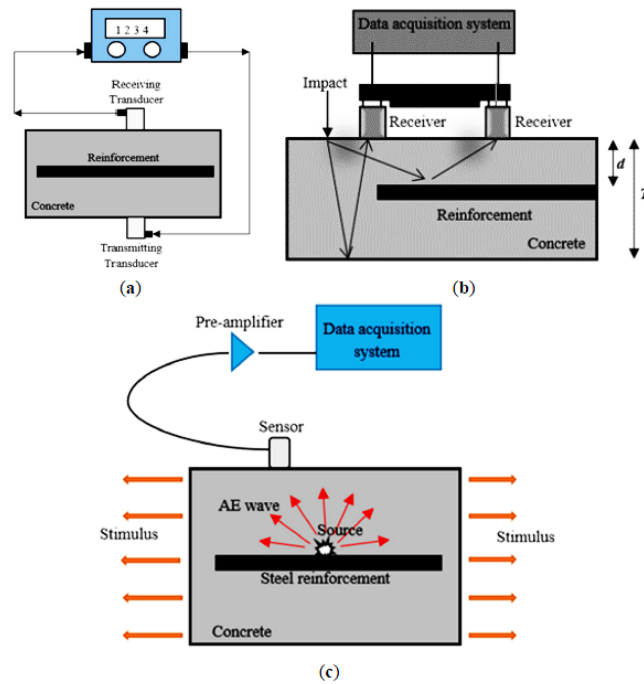


Figure 1.1: The principle of a) ultrasonic pulse velocity; b) impact echo; c) acoustic emission (Zaki et al., 2015)

Different studies demonstrate how the usage of *AE* method is important to early interventions in those RC elements affected by corrosion. This is possible to do it with a real simple technique which does not imply the failure of the sample during the process. (Zaki et al., 2015).

#### 1.1.2. Electromagnetic method: Ground Penetration Radar (*GDR*)

One of the most common methods for the concrete assessment is the use of the Ground Penetration Radar (*GPR*). It is a *NDE* which is used not only for concrete but for different applications. *GPR* uses the electromagnetic wave that travels in a mean of transport using the principle of the dielectric materials. The signal is emitted by a transmitter and recorded by an antenna. This technique exploits the change in wavelength of the signal emitted when it encounters a material with a different value of dielectric. With this principle it will be easy to evaluate the presence of cracks and it is appropriate and very spread the evaluation of the level of corrosion with the *GPR* [3].

*GPR* need to be coupled with a data recorder which is able to back-calculate the quantities and evaluate the assessment of the reinforced concrete element. Such models are difficult to implement and need an accurate discussion. Many studies have been developed on this sense, with the purpose to implement the analysis and improve the properties evaluations [4]. Moreover, the signal is of course affected by the type of dielectric and the environmental conditions that can influence the different read values. These parameters are temperature, pressure, chloride, microstructure of the pore and so on. So *GPR* method is a good way to assess the structure of the concrete but needs a set of equipment and software able to read the data collected.

### 1.1.3. Optical method

In the huge field of applications of *SHM* visual and optical method have a big role in evaluation of acceleration and velocities. These methods are developed in order to detect multiples local values and coupling to create a model that can be used for software applications. So, this approach cannot be used for global interpretation of damages but just for a focus and better acknowledgement of a local disturbance in the structure. The most common instruments that are used in this configuration are the Laser Doppler Vibrometer (*LDVM*), *GPS*, optical marker tracking, interferometry and so on. The problem of these sort of applications is that it is not possible to directly calculate the displacement. So, it is necessary to retrieve them from the velocities, accelerations and models generated with respect to the monitoring evaluations retrieved on the field.

## 1.2. Classical devices for *SHM*

The main goal of *SHM* is the calculation of the remaining life of the structure. Since the early 80s, civil engineers have been looking for new technologies that were able to collect the data from the structure and gives back deformations and strains. These are fundamental in the determination of the stresses and the consequence evaluation of the remaining life of the structure.

The main advantage of the use of health monitoring is the reduction of the control of what is happening in the structure. This concept takes an important role in the decisions and lead to a programming and intervention on the structure as it is thought to be. In fact, knowing the response to a given solicitation is fundamental to forecast the behaviour of the structure. Thus, health monitoring can be an important tool for an engineer that if it is used properly can provide warnings and possibly prevent a failure. In this sense, *SHM* can be seen not only as a method to ensure a safer structure but also as a cost-effective operation which increase the probability of surviving of a building.

In the next paragraph there will be listed and described some of the common equipment that are used for monitoring and some of the more innovative.

### 1.2.1. Metallic Strain Gauges

The metallic strain gauges are the most diffused tools used for the control of the straining of an element. They have a long history in the applications in civil structures and generally to a lot of structures with applications in engineering. It was invented in 1938 by Edward E. Simmons and Arthur C. Ruge and it finds a huge field of applications in all the structures and infrastructures. It is largely use in several applications mainly due to its ease of application and accuracy. The metallic strain gauge is a metallic foil applied on the surface of the element to determine the elongation and retrieve the tension inside. The metallic foil is a conductor. When the foil is subjected to a stress, that can cause either tension or compression, it leads to a change in resistivity that is converted into a tension evaluation. The change in resistivity is detected through

electrical wires that are applied on the foil. Strain gauges have different configuration according to the direction of the deformation that can be detected and the number of grids that contains.

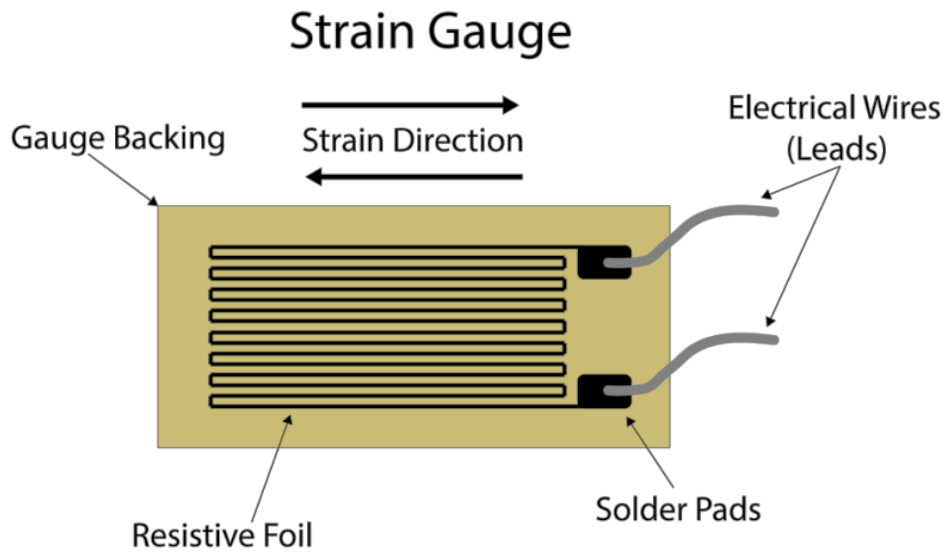


Figure 1.2: Scheme of the metallic foil [5]

The working principle of the strain gauge is the application of the Wheatstone Bridge which is a circuit with four branches of resistance, where the elongation is given by one or multiple variable resistances according to the application.

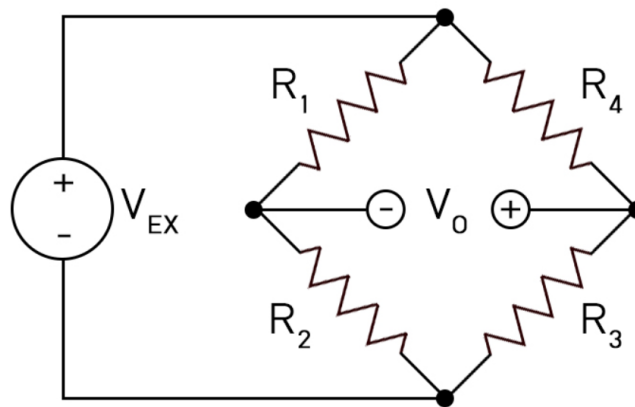


Figure 1.3: Wheatstone Bridge

The Wheatstone Bridge works using the variable resistances. The most simple and general application consists in an element that alimentes the circuit which is indicated in the figure by the  $V_{EX}$  while the variation of resistance is measured in correspondance of the  $V_0$ . The principle of working of this instrument follows the evaluation of resistance by considering a change in volume. Generally, an elongated element can be seen as mono-dimensional sample. A tension or compression stress correspond to a variation of length and a corresponding deformation of the section. In particular, with a tension stress the area of the cross section undergoes to reduction in cross section that depends

on the Poisson ratio of the element, which depends on the constitution material of the gauge. Generally the resistance of the strain gauge can be calculated as:

$$R = \rho \frac{L}{S}$$

Where:

- $\rho$  is the resistivity of the material;
- $L$  is the length of the element;
- $S$  is the surface of the cross section.

Considering the material with a constant resistivity, so it does not depend upon the deformation of the material. As the formula shows, an elongation corresponds to an increase of resistance and the same happens with a decrease of the area of the cross section. Generally, it is possible to express the variation of resistance as:

$$\frac{\Delta R}{R} = \frac{\Delta L}{L} - \frac{\Delta S}{S}$$

Following this concept, the number of resistances that varies in a Wheatstone Bridge is the key in the application of this methodology. There are three different configurations that can be used according to the number of varying resistances: quarter-bridge strain gauge, half-bridge strain gauge and full-bridge strain gauge. The configuration used allows the calculation of the resistance and the straining that can be evaluated with either an axial or a bending solicitation. [6].

#### 1.2.2. Linear Variable Differential Transducer (*LVDT*)

The *LVDT* is a different type of instrument with respect to the strain gauges. It calculates strains of an element using the principle of the mutual inductance. The scheme of the *LDVT* consists in a hollow core shaft where a metallic mass lies. Surrounding the shaft there are two different coils, that are called primary and secondary coils, that have the purpose of measuring the inductance generated in the core of the shaft. This inductance is generated, either in static or dynamic conditions, by the displacement of the metallic core inside the element. The read in voltage generated by the tool needs at first to be calibrated and this is done by moving the core by a definite distance and calculate the relative initial voltage. [7]

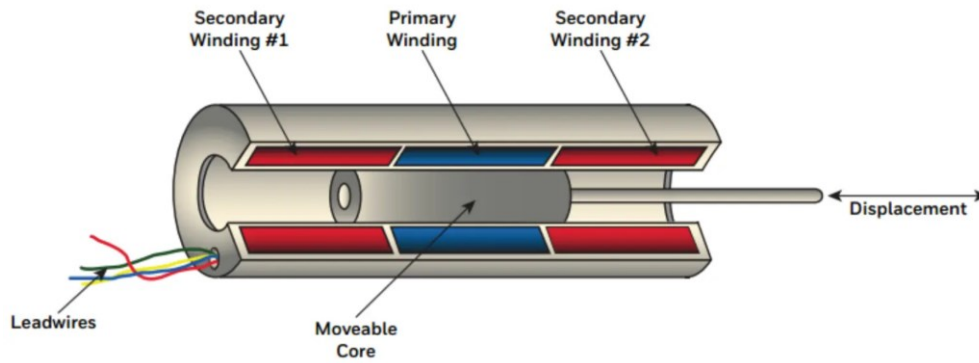


Figure 1.4: Scheme of a LVDT [8]

### 1.2.3. Accelerometers

The most common element used for dynamic evaluation is the accelerometer. Measurement of acceleration gives important sources of data for what concerns the *SHM* in dynamic or static loading conditions. Traditional accelerometers develop a large use with the new technologies in the civil engineering field. The concept of the acceleration is based on the reading of mechanical or thermal vibration that occurs to an element when a stress is applied. Moreover they also have embedded a calibration system that helps the user during the applications. Different types of accelerometers have been used for civil engineering purposes. The most common accelerometers used are:

- Piezoelectric accelerometers (*PZT*): very commonly used to detection of speed and displacements; the *PZT* uses the piezoelectric properties of any material, which subjected to mechanical stress are able, by the application of a transducer, to retrieve the electrical signal of the element; the principle used by the element follows the second Newton's rule and it is applicable with all the simple solicitations, which are axial, shear and bending forces [7];

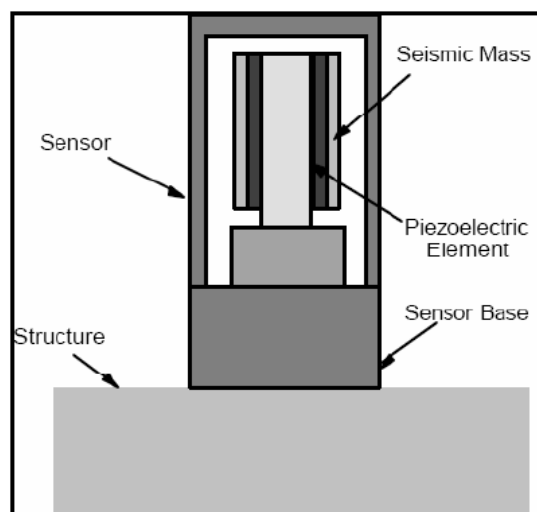


Figure 1.5: Scheme of a piezoelectric capacitor [7]

- Capacitive accelerometers: differently from the piezoelectric these elements are used to calculate static deformations; the scheme of the tool consists in a seismic mass put in between two different dielectric materials. The mass is suspended between the two electrodes, linked to the structure by a flexible element in order to detect the displacements.

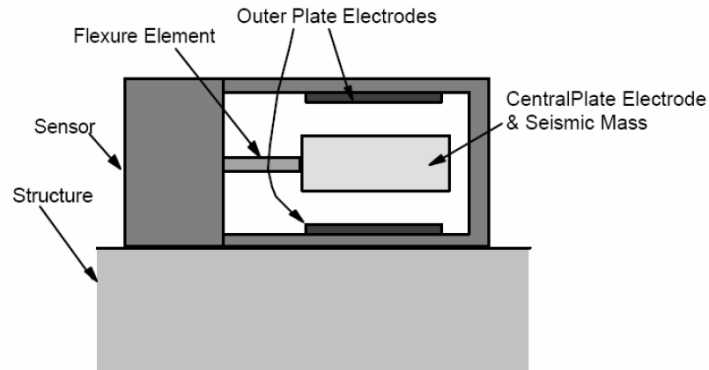


Figure 1.6: Scheme of a capacitive piezometer [7]

- Force balanced accelerometer: the evaluation of the acceleration or displacement in this instrument is carried out by a central axis linked to four supports on the edge; the structure is also linked to a capacitor which is able to measure the displacement; this measurement is carried out by applying an acceleration to the structure, hence the inertial force will allow the displacement of the central axes of the structure which will be converted in a change of capacitance in the element; in this way it is possible to estimate acceleration with very low frequency [7];

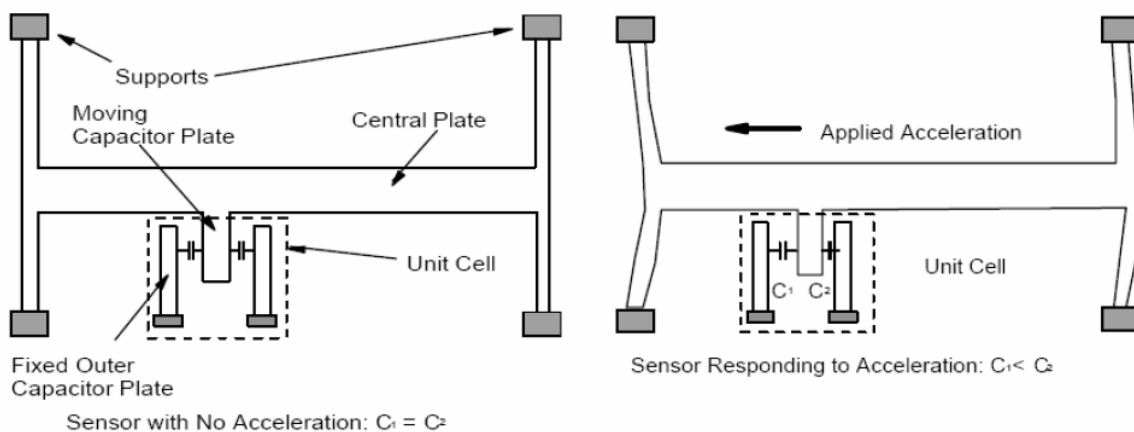


Figure 1.7: Scheme of a force balanced accelerometer (Enckell, 2006)

#### 1.2.4. Wireless vibrating wire system

Another important application for *SHM* that concerns the strain measurement is the vibrating wire sensor. This method is one of the most classical used for the evaluation of the responses to the stress of single element. The Vibrating Wire System (*VWS*) uses the principle of vibration and changing in resonant frequencies to read the responses to an external action. In fact, with a solicitation of compression or tension the beam results in a change of the natural frequencies of the element. The response depends on many actions such us length of the wire, material of the wire, timing of the action, elastic modulus. The problem of the implementation of the *VWS* is the impossibilities of retrieving a multiple reading from the same device since every point and every wire is capable of the reading of just one resonant frequency. To improve the sensor it has been developed a system which is based on the *VWS* but with the purpose of performing a more global evaluation method without the costs of the wires and with multiple acquisition points [9]. In this method, using a module has been possible to retrieve from a single point of application different frequencies and implement a long term-evaluation of the structure. The system can work on several different frequencies thus is really versatile as a tool for monitoring.

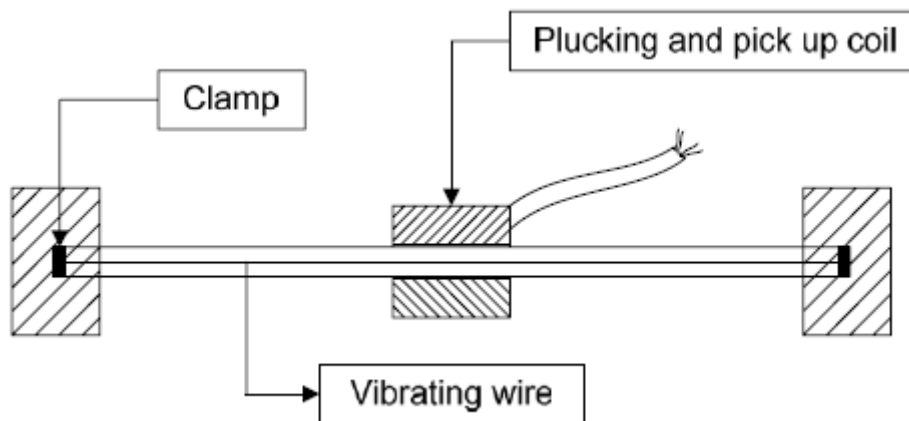


Figure 1.8: Vibrating Wire System [9]

### 1.3. Fibre Optic System (*FOS*)

Fibre optic system (*FOS*) find a vast field of application in monitoring for civil engineering constructions. The system gives its versatility to safeness and stability of the measurement performed on the field. The classical scheme of a *FOS* consists in an application of a wire extended for all the length of the element. This wire can be applied outside of the material or embedded into it. The wire contains a core made by a material with dielectric properties and it is coated by a polymer and other layers in order to protect the cable from impact and isolate the signal transmitted in the core from the interferences reducing the noise in the measurement.

Transmission of signals using the light gives the possibility to have a *SHM* with several advantages, that helps the latest spreading of this technique in the monitoring of the structure. Among all the advantages it is important to point out the resistance to corrosion. The cable is insulated from the outside thus the galvanic cell is not triggered and the possibilities of failure due to this mechanism are very low. Moreover, most of the time *SHM* has the limit of monitoring on specific and local point of the structure. The possibility of distributing the cable upon the element gives consequently a package of data that is more consistent than other devices. Nevertheless, the transmission of the information along the cable with this solution is really enhanced, thus, the procedure of data collecting is fast and it can be done remotely [2].

*FOS* is based on measuring the variation of the properties of the material according to how the light travel in the cable and is reflected by the device. According to the deployment of the systems it is possible to distinguish:

- Point measuring, the sensor is placed in a specific point and the measuring happen according to the property variation of that sensor with a single channel of communication for every point;
- Integrated, obtaining one single value by merging the values that come from the element;
- Semi-distributed, similar to the point measuring but the cable is unique;
- Distributed, they allow a continuous and accurate evaluation of the structure allowing the “spatial mapping” of the element [10].

In a *FOS* system is possible to analyse and varying 4 different parameter that are the characteristic of the light propagating in the cable. Those parameters are *phase*, *polarisation state*, *intensity*, *wavelength*. Therefore, the variation of every parameter leads to a different type of modulation of the signal and in particular they are named respectively *interferometric*, *Polarimetric*, *Intensity modulated*, *Spectrometric*.

### 1.3.1. *SOFO*

This typology of fibre optical sensor uses the modulation on phase of the light to measure displacements and deflections. *SOFO* used a cable in which two fibres are positioned. The fibres are fixed to two anchorages placed at a determinate distance. The working principle of this solution consists in one of the two fibres which is pre-tensioned while the other one is let loose inside the cable. The displacement is measured inside the tensioned fibre while the loose one is called “reference fibre”. The measurements are detected in the element by referring to the coherence of the light. The phase coherence between the two cables is measured by a demodulator which the element is linked at. Hence, *SOFO* is classified as an interferometric optical sensor. The measuring part, the one between the two anchorages is the active part. This is coupled to a passive part which is responsible of collecting the data, modulate the signal and calculate the displacement due to a mechanical or thermal effect. *SOFO* is a really stable and accurate instrument since its precision does not depends on the intensity of the light but on the coherence of the signals in the two fibres [2].

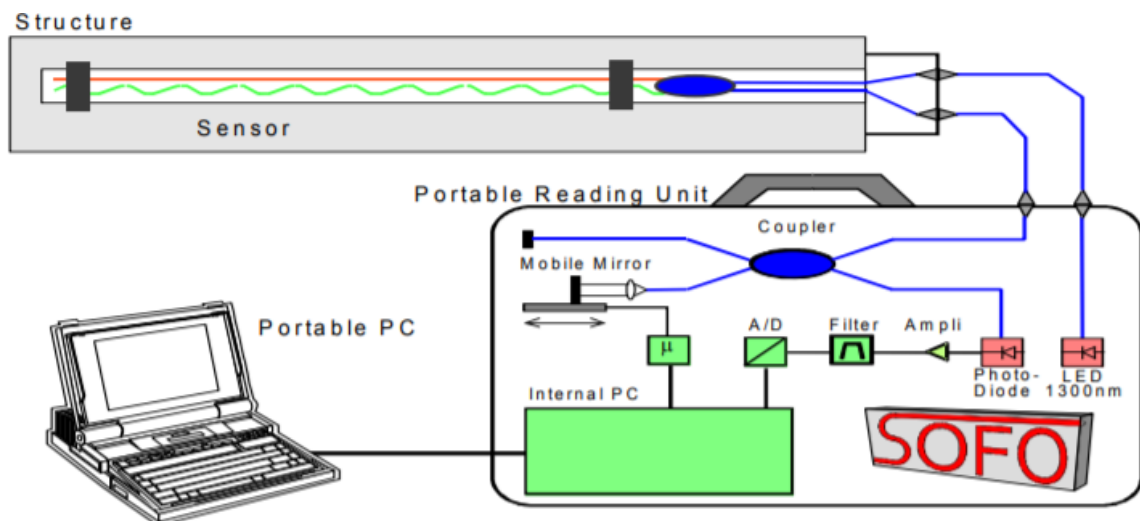


Figure 1.9: Scheme of *SOFO* [11]

### 1.3.2. Fabry – Perot interferometric sensor

A Fabry – Perot interferometric sensor is an instrument that use the same principle of the *SOFO* to calculate the change in strain of the element. It is formed by a long cable distributed in the structure. This cable has a cavity that host two partially mirrored fibre with the mirrors facing each other that leaves an air gap between them. The light is launched inside the cavity and is reflected by the mirrors. The strain in the *FP* sensor is read by a change of distance in this air gap that will be measured as a change of phase measured by the digital unit which carries the role of a passive unit. Thus, the *FP* sensor is a localize sensor and it is possible to calculate the strain by averaging the strain calculated in different points where the cavities are located [11].

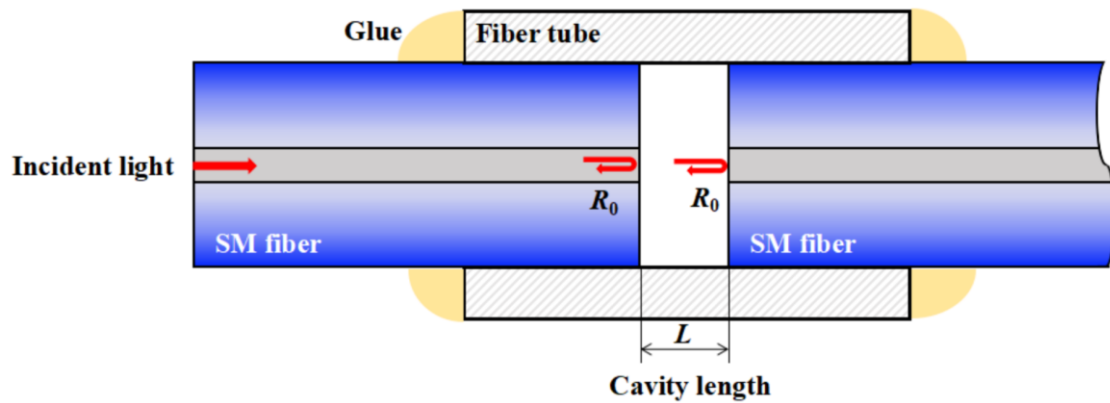


Figure 1.10: Scheme of a FP interferometric sensor [12]

The principle used by the sensor is the change of phase when the light is transmitted through the glass. In particular part of the light is back reflected into the tube while the part which passes through undergoes to a change in inclination. The light that impacts on the second mirror and is reflected is affected by this change in phase, hence when it is back reflected is possible to retrieve the variation in phase and consequently calculate the displacement.

### 1.3.3. Fibre Bragg Grating Sensor

Grating sensor are really used in the field of civil engineering *SHM* these days. It consists in a 10 mm longer grating where the light is partially reflected in order to calculate the displacement of the element. Fibre Bragg Grating (*FBG*) sensors are a particular type of sensor displayed into the core of a fibre cable. The sensor is cladded to protect the core from the environment and coated to prevent the corrosion of the instrument. Along this grating, only one portion of the light is reflected while the other part is let passing through. This portion of light have a specific wavelength indicated by  $\lambda_B$  and it is called Bragg wavelength. It is reflected back, while the rest of the light continues his path along the cable. The wave reflected depends upon a specific period of modulation called Grating Period. It is possible to calculate the wavelength by considering this formula:

$$\lambda_B = 2n_{eff}P$$

Where:

- $n_{eff}$  is the effective refraction index of the core;
- $P$  is the grating Period.

The application of an external mechanical stress in the element lead to a shift of the reflected wavelength. From this shift is possible to recalculate the straining of the element. That is possible to retrieve for both static and dynamic load but it needs a different approach and a calibration when it deals with temperature stresses.

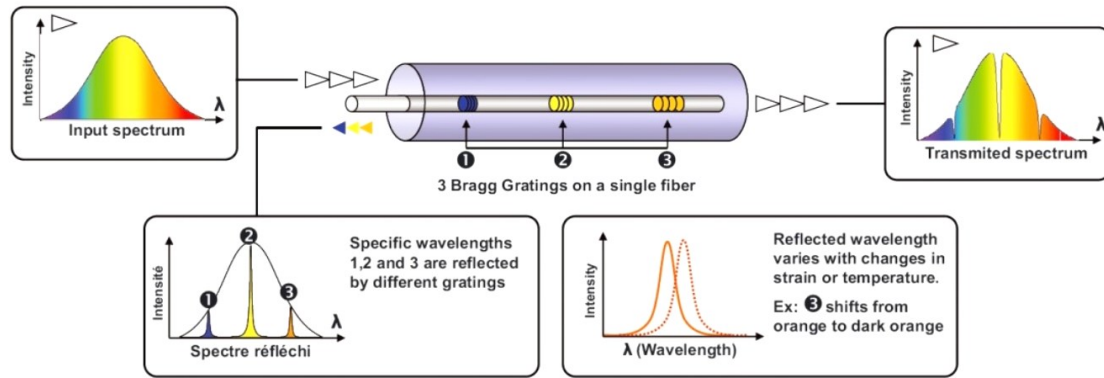


Figure 1.11: Fibre Bragg Grating Scheme [13]

Once the wavelength has been identified, from the shift in the wavelength, as it is shown in the graph above, it is possible to retrieve the straining of the element subjected to the mechanical or thermal stress. In particular, it needs to be said that thermal stresses need a calibration if the wavelength has high incidence [11]. The equation from where to start in order to calculate the strain is the following.

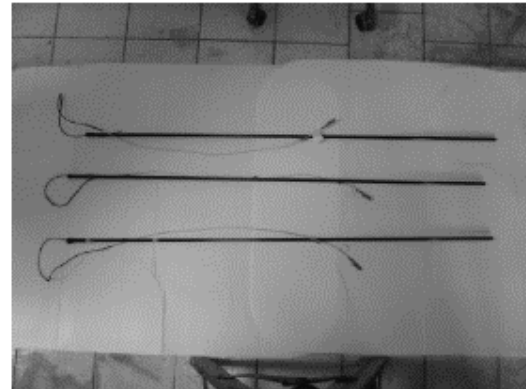
$$\Delta\lambda_B = \lambda_B [(\alpha + \xi)\Delta T + (1 - p_e)\Delta\varepsilon]$$

Where the components are:  $\Delta\lambda_B$ , wavelength shift,  $\lambda_B$ , Bragg wavelength,  $\alpha$ , coefficient of thermal expansion,  $\xi$ , thermo-optic coefficient,  $\Delta T$ , variation of temperature,  $p_e$ , strain-optic coefficient and  $\Delta\varepsilon$ , strain variation.

An example of a particular application of the *FBG* in the *SHM* is carried out in a study of Corvaglia *et al.*, 2010 [15]. In This application, it has been carried out the concept of introducing Fibre Reinforced Polymer (*FRP*) on the surface or in the matrix of the element. In particular two applications were proposed. The first one concerned the implementation of a fibre optic device inside a *FRP* reinforcing sheet which is called Smart Patch (*SP*). The second and more innovative application is called Smart Rebar (*SR*). This consists in a pultruded *FRP* rebar with a modification carried out during the process of pultrusion. In fact, during the production a fibre optic element was inserted in the rebar promoting the final result to obtain a *SR* used for both reinforcing and monitoring purposes.



a)



b)

Figure 1.12: a) Smart Patch; b) Smart Rebar (Corvaglia, et al., 2010) [15]

### 1.3.4. Distributed sensor

The main limit about the *FOS* listed above is that they need a specific device located in a point. Hence, the strain variation is always measured in that single point and the general displacement must be retrieved starting from a set of discrete data.

A distributed fibre optical sensor (*DFOS*) overcomes to this problem since it works using all the length of the fibre optic cable to scatter the light that comes from the emitter. From this point the light travel with a certain wavelength and it will be reflected at each and every single point in the cable. The scattering occurs in every direction but only a portion of it will be retransmitted to the starting point where a receiver is capable to demodulate the information contained in the signal. In particular, it is possible to retrieve the value of the strain that happens in that point and the temperature of each point transmitted. This information is contained in the output graph where it can be distinguished three main points that correspond to three different wavelengths. In particular, it is possible to distinguish:

- Rayleigh scattering, it has the same wavelength of the emitted light and it contains the same information; it can be used for applications where the cable is long less than 70 m with a resolution of about  $1\mu m/m$  ;
- Brillouin scattering, it has different wavelength with respect to the Rayleigh. It contains information about the point where the light is reflected. The information is about straining and temperature changes and in particular these are given by the change in frequency of the wavelength; it is capable of long distance measurement but the resolution decrease up to 10 m with the increase of the distance;
- Raman scattering, as for Brillouin it has a different wavelength. In this case the information is all about the temperature changes that occur in the element and are expressed through the variation of amplitude of the signal.

Many applications have been used in order to measure strain and temperature. In particular, this sensor's technique has been used for long term strain and temperature measurement with the cables embedded in driven piles for geotechnical applications [16].

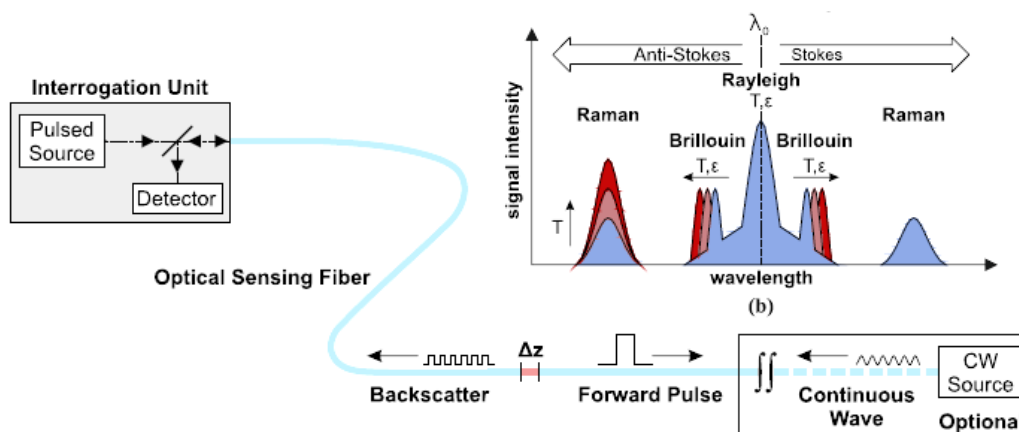


Figure 1.13: Functioning of a DFOS [16]

The *DFOS* available in commerce are called Optical Backscatter Reflectometer (*OBR*). On example of applications is provided by using the Optical Rayleigh Frequency-Domain Reflectometer (*OFDR*). In the implementation of this technique it has been used a new way of protecting the cable. This in order to overcome to a problem related to a non-correspondence in the strains measured in the cement matrix and in the cable. In particular the two solutions proposed were:

1. The former one, where the core and cladding were encapsulated with a layer of polyimide primary coating, with a diameter of approximate  $250\ \mu\text{m}$ ;
2. The proposed one, where the core and cladding were encapsulated with a layer of acrylate primary coating, with a diameter of approximate  $190\ \mu\text{m}$ .

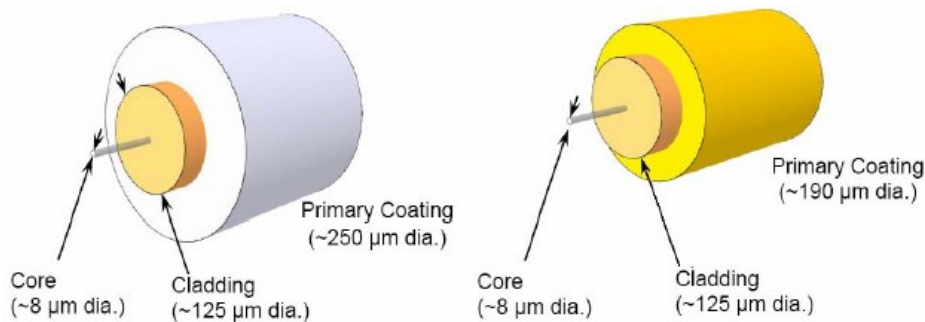


Figure 1.14: Structure of the *DFOS* used in the experiment [17]

The cable has been implemented in two configurations in order to analyse the strain of the element. The first methodology proposed the *FO* bonded to the surface of the rebars. The new innovation was the second one where the cable was embedded into a groove positioned inside the rebar. Here following the scheme of the application for the embedded *DFOS* used for this implementation [17].

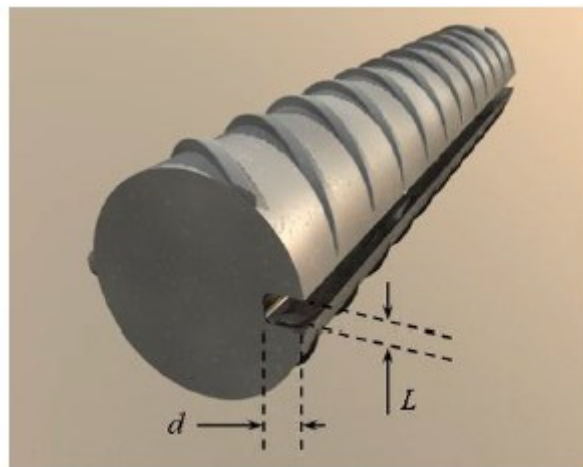


Figure 1.15: Rebar grooved for the implementation of the *FOS* (Quiertant, et al., 2012)

## 1.4. Innovation with piezoelectric sensor in *SHM*

*SHM* is a field which is continuously in development. The research of a cost-effective materials is leading to look forward to element which are less expensive, small and are capable of a real time monitoring. This leads to embedded solutions which uses the piezoelectric properties of the material in order to collect information about straining and state of stress of the material. Here below are reported some of the latest innovation in the scenario of *PZT* material.

### 1.4.1. Smart aggregate in a steel fibre concrete specimen

Reinforced concrete elements have been a source of interest for the engineers in the years. The principle of improving the strength of a structural element has been enhanced through a series of techniques. One of this technique is the distribution in the matrix of the specimen a determined quantity of fibres which aim to increase the bendability of the element. Fibres made by different material have been used, such as carbon, polymer, steel, and many others. The technique reported here shows how the usage of steel fibre not only help the reinforcement of the specimen but is also capable of helping in the *SHM* of the structure. In fact, the steel fibre inside the specimen helps to collect the Electromechanical Impedance (*EMI*) for the different specimen providing the evaluation of the resistance of the material and so really important in terms of Structural Health Monitoring.

Alongside to the fibre, a smart aggregate (*SA*) was embedded in the middle of each specimen. The smart aggregate has the shape of a disc with a diameter of  $25\text{ mm}$  and a height of a  $20\text{ mm}$ . This element is made of marble and a *PZT* element is set in the middle of it. The marble offers a protection to the *PZT* and it clads it in order to be casted later in the concrete specimen to allow measurement. Inside the marble, the *PZT* is applicated on an epoxy resin and a lead wire is attached to transmit the data. The *SA* is coupled with the steel concrete specimen in order to measure the *EMI* related to the change in load which has been experienced during the experiment. Here below a scheme of the *SA* is shown.

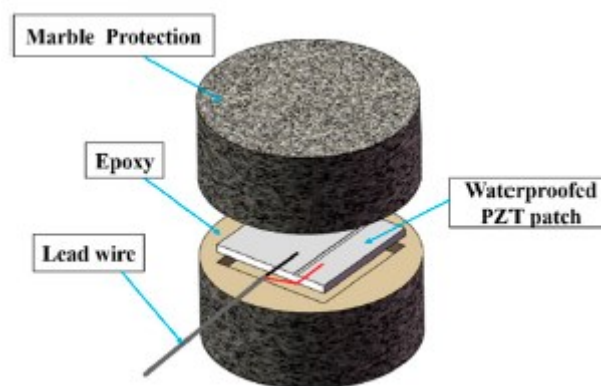


Figure 1.16: Smart Aggregate Composition (Wang, et al. , 2018)

The principle of the *EMI* measurement is to obtain the data from any deformation, crack or change that affect the structure. The coupling effect between the smart aggregate

and the steel fibre concrete allows the measurement of the acceleration and can be visualized as a system composed by a spring-mass dumper. Varying the quantity of the steel fibre the study reports the change in resistance and frequency of the specimen [18].

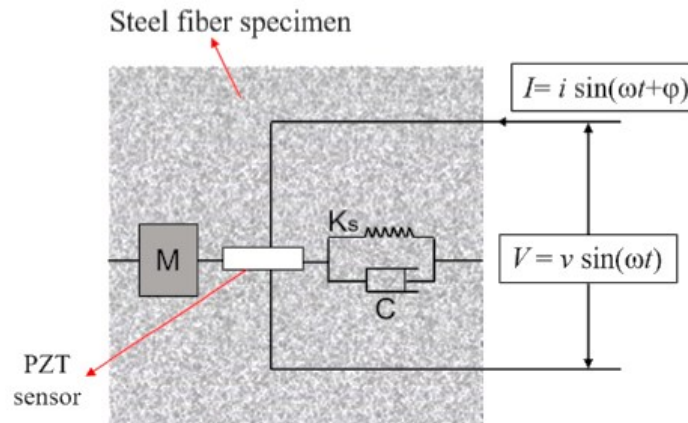


Figure 1.17: Spring-mass-dumper EMI measurement [18]

#### 1.4.2. Doped concrete with Carbon Nanotube for SHM

A way in between the smart aggregate and the reinforcing fibre casted in the matrix of the concrete element is the dispersion of Carbon Nanotubes (CNTs) particles. This technique takes the name as Multi Walled Carbon Nanotubes (MWCNTs) and it consists in a dispersion in a specimen of concrete of particles that are capable of measuring the resistivity of these elements to calculate the straining and the stress state of the sample. This solution is an efficient and cost-effective method to promote the SHM.

The particularity of this method is the possibility to self-sensing the strain of the material along all the element subjected to the test or the field applications. In order to evaluate the efficiency of the method a study has been carried out by Meoni *et al.* in 2018 [14]. The CNTs are dispersed in samples with different quantities and density and they are a good material to provide the sensitivity or the conductivity of the element subjected to the load. The straining of the element corresponds to a change of resistivity of the material similar to what happened for the strain gauges previously treated in this thesis. In particular, the study has been focused on understanding how much the variation of quantity of MWCNT affects the measurement of strain.

The material used for the tests was *Arkema Graphistrength C100*, which has the characteristics reported in the table 1.1. The building procedure of the sample cubes with the side of 5 cm is represented below.

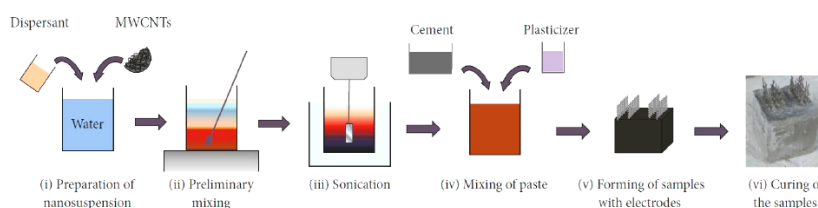


Figure 1.18: Procedure for the preparation of a sample with MWCNTs [14]

Table 1.1: Characteristics of the MWCNTs [14]

MWCNTs characteristics	
Colour	Black
Carbon content	>90%
Apparent density	50-150 kg/m <sup>3</sup>
Average number of walls	5-15
Diameter	10-15 nm
Length	0,1-10 μm
Surface area	100-200 m <sup>2</sup> /g
Elastic modulus	1 TPa
Tensile strength	150 GPa

To calculate the straining of the element a simple formula is used.

$$\frac{\Delta R}{R_0} = GF \cdot \varepsilon$$

Where:

- $\Delta R$  is the variation in resistance;
- $R_0$  is the initial resistance;
- $GF$  is the gauge factor;
- $\varepsilon$  is the strain along the loading axis.

The method proposed shows a good relationship between the change in resistivity and the measurement of strains in the cube. Moreover, the addition of the *MWCNTs* provides an enhancement of the strength of the plain concrete sample that means they have a double positive effect on the element.

#### 1.4.3. Piezoelectric sensor embedded into steel rebars

Piezoelectric (*PZT*) sensors are not only used to create *SA*. In fact, embedding this material into the steel rebars has been proved as really useful in detection of damages and *SHM* of beams. This technique has been implemented and improved by *Karayannis et al.* in 2015 [15]. The study presents the integration of *PZT* sensors in the rebars with the purpose of evaluation damages or potential damages by the variation of admittance of the element. It has been proved that elaboration of this kind of signal from a structural element exposed to mechanical load generates variation of admittance or impedance and this can be used as real-time monitoring for *SHM* purpose.

This technique has been implemented on single steel reinforced bars and steel reinforcing bars embedded in two typical large scale RC beams. *PZT* are used during the experiment as both actuators and sensor. It means that they are used, respectively, to transduce a mechanical stress to an electrical signal or vice versa. In particular, the signal measured with this method is the admittance that is function of the frequency of the application of the load. This is the fundamental parameter in the evaluation of the

efficiency of the load and the excitation can be expressed through a harmonic function with the following expression.

$$V_{PZT} = 10 \sin(2\pi\omega t)$$

From this excitation the admittance is recorded in two separated form that can be expressed by conductance, which correspond to the real part of the signal, and susceptance, that is the imaginary part of it. These two quantities are summed up together to reach the absolute value of the admittance.

$$|Y(j\omega)| = \sqrt{G^2(\omega) + B^2(\omega)}$$

The formula above contain:  $V_{PZT}$ , the excitation in voltage,  $\omega$ , the angular frequency,  $t$ , the time domain range,  $Y$ , the admittance obtained by the test,  $j$ , the imaginary unit,  $G$ , the real part of the excitation (conductance) and  $B$  the imaginary part of the excitation (susceptance).

The calculated admittance is than converted on estimated damage by approaching a statistical method named Root Mean Square Deviation (*RMSD*), which express the variation of the admittance in a damaged sample with respect to an undamaged one.

$$RMSD = \sqrt{\frac{\sum(|Y(j\omega)|_D - |Y(j\omega)|_0)^2}{\sum(|Y(j\omega)|_0)^2}}$$

Where:

- $|Y(j\omega)|_D$  is the absolute value of the admittance of the *PZT* at the examined damage state;
- $|Y(j\omega)|_0$  is the baseline value of the admittance (healthy state).

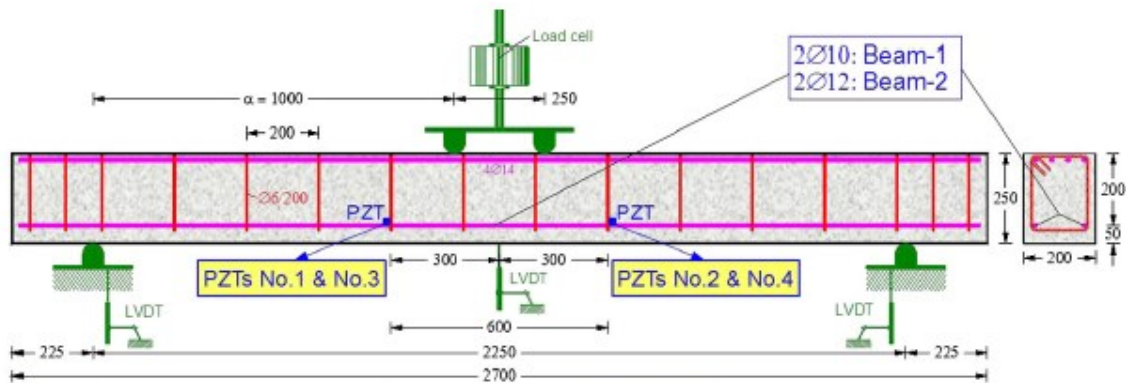


Figure 1.19: Schematization of a steel reinforced bar with the application of a PZT sensor [15]

## 1.5.Sensitivity

An important factor in the evaluation of the health of the structure is the precision and accuracy that the instruments offer. This is important to understand the performance of the devices that are used in the *SHM* evaluation. In the engineering field, every detection that is carried out it must be such that guarantee an adequate level of trustfulness. Different terms are related to this aspect and each of them expresses a different feature of the instrument. From this point of view, they can be seen under different perspectives, for example if the readings are close to a certain value or if different measurements have to be similar one with another in order to evaluate the consistency of the analysis. With this mind, in general applications, it's possible to distinguish four different terms that can be applied to the measurement of a physical quantity. These are:

- Accuracy, it measures how far a measurement is from a standard value; it depends most of the time on the range of measurement of the instrument; high accuracy means that the average between different measurement is close to the correct or standard value;
- Precision, represents the possibility to obtain a consistent value among several repetitions; high precision means a small difference between several measurement considered; in statistical terms it corresponds to a low standard deviation;
- Resolution, can be intended as the range that can be measured over the minimum quantity that can be detected by the instrument; So this quantity is strictly related to the principle of working of the device and it aims to evaluate the smallest theoretical variation on the full scale of the tool;
- Sensitivity, it deals with the capability to detect changes in the measurement; the smallest possible absolute quantity that is possible to be read corresponds to the sensitivity of the instrument, considered as the variation of the physical quantity measured those changes with respect to the real variation of the same.

The goal of *SHM* is to evaluate the health of a structure and to estimate the remaining life of it. In this sense, the parameters that among the others are valuable for this analysis are strains and state of stress within the element. The methods described in the previous paragraph are not built to cope directly with elongations and stresses but these parameters can be indirectly obtained by considering the electric signals. The working principle of the instruments is different one from another but everyone processes electrical signal that gives a response with respect to a solicitation. In order to have a uniform parameter to evaluate the sensitivity, the different readings in the unit of measure compatible with the principle of working of it are converted in strain related to the minimum value that is detected by the instrument.

In this thesis, as first approach to evaluation of the sensitivities of the instruments, it has been considered a comparison between sensitivities of the same typology of instrument. This kind of comparison has been carried out to assume an interval where

the instrument lays for the measurement and according to it classify the quality of the instrument.

### 1.5.1. Strain gauge

The sensitivity of a strain gauge is calculated according to a factor that is called *Gauge Factor (GF)*. The *GF* is a measure of the variation of resistance that occur with a variation in terms of elongation. When a tensile or a compressive stress arose within a beam it undergoes to deformation. This deformation is collected by the strain gauges as a change of resistivity along the plan where these are applied. It is possible to express the *GF* as it is showed in the following equation.

$$GF = \frac{\Delta R/R_0}{\varepsilon}$$

Hence, the smaller this number it is the better is the quality in the evaluation of the strain related to changes in resistance. To consider the difference in the calculation of sensitivity some examples of strain gauges are reported below.

Table 1.2: Characteristics of the Strain Gauges

		Models				
Producer	-	Zemic Europe			HBM	
Model	-	ZMY120-3AA	ZMY350-2AA	ZMY1000-5AA	LY11-1,5/120	LY11-6/120
Grid Length	m m	3	2	5	1,5	6
Stain range	%	2			5	
Nominal Resistance	Ω	120	350	1000	120	120
Resistance tolerance	%	0,10			0,30	0,30
Gauge Factor	-	1,80-2,20			2	2
GF tolerance	%	<±1			±1,5	±1
Reference temperature range	°C	-20 to +200			-10 to +120	

For the evaluation of the tolerance expressed in strain, it has been reported some examples of two companies that produces stain gauges model. The two companies taken as example are the *ZEMIC Europe* and the *HBM*. In order to understand the importance of the sensitivity it has to be considered the length of the grid. This is important since it has been taken in consideration the axial elongation of the strain gauges. Furthermore, the length of the strain gauge is important to understand the maximum elongation that can be registered from the devices. The strain limit is also reported in the table above.

A value which is important to point out in the evaluation of this device is the resistance measured by the strain gauge. This is important to understand how the instrument works and the range measured by the device. The resistance tolerance is the error recorded by the instrument during the elongation measurement. The sensitivity of the instrument is strictly correlated to the resistance and the strain measured as it is displayed in the previous paragraph. For example, considering the *LY11 – 1,5/120*, the resistance used by this model is  $120 \Omega$ . To understand the minimum reading that can be operated in an application of a strain gauge it is necessary to consider the reading instrument that is operated alongside the strain gauge. This minimum value corresponds to the resolution that is used to perform the calculation. The resolution is intended as the minimum value that can be detected by the device that is used to obtain the reading of the variation of resistance corresponding to an elongation. This is usually equal to tens of milliohms. So, it has been assumed a variation of resistance equal to

$$\Delta R = 0,1 \text{ m}\Omega$$

Once that the variation of resistance has been defined it is possible to consider the straining corresponding to this variation. This is carried out considering the  $GF = 2$  and the  $GF$  that considers the tolerance of  $1,5\%$ . The calculations are reported below.

$$\varepsilon = \frac{\Delta R}{R_0} \cdot \frac{1}{GF} = \frac{0,0001}{120} \cdot \frac{1}{2} = 0,000000416 \varepsilon = 0,416 \mu\varepsilon$$

$$\varepsilon_{1,5\%} = \frac{\Delta R}{R_0} \cdot \frac{1}{GF \pm 1,5\%} = \frac{0,0001}{120} \cdot \frac{1}{2,015} = 0,000000413 = 0,413 \mu\varepsilon$$

The difference between the value with the standard  $GF$  and the one with the error express the sensitivity in microstrain.

$$\Delta\varepsilon = \varepsilon - \varepsilon_{1,5\%} = 0,416 - 0,413 = 0,003 \mu\varepsilon$$

#### 1.5.2. Fibre optic system (SOFO)

The *FOSs* are different from the strain gauge in terms of sensitivities. The functioning of the system gives back measurement in strain. Hence, it does not record a measurement in  $\Omega$  as it happened for the device seen in the previous paragraph but they evaluate changes in length read by the modification of the wavelength of the light that run across the cable. The difference in terms of sensitivity is related to the typology of *FOS* used and the way it works. The most common *FOS* used in the market nowadays and analysed in this paper are described here below.

*SOFO* sensors are largely used nowadays in the health monitoring field. Some of the characteristics of the *SOFO*, produced by *SMARTEC SA*, are reported below.

- Length of active zone (*LA*): 25 cm to 10 m;
- Length of passive zone (*LB*): 1 m to 100 m;
- Measurement range: 0,5% of *LA* in shortening, 1% of *LA* in elongation;
- Measurement precision: 0,2% of the measured deformation or better;
- Measurement resolution: 2  $\mu\text{m}$  RMS;

- Operating temperature for standard active zone:  $-50\text{ }^{\circ}\text{C}$  to  $+110\text{ }^{\circ}\text{C}$ ;
- Operating temperature for standard passive zone:  $-40\text{ }^{\circ}\text{C}$  to  $+80\text{ }^{\circ}\text{C}$ .

As first comparison with the characteristics of the *SOF0* with respect to the accelerometer, for example, it is possible to understand that the range of measurement is different. Small and even imperceptible deformation can be detected in a more sensible way considering the *SOF0* sensors.

Considering the maximum length of the active zone  $L = 10\text{ m}$  it is possible to understand the precision that is possible to retrieve with respect to the maximum elongation of the element. Considering an element deformed in tension, the maximum possible elongation of the *SOF0* sensor is  $0,1\text{ m}$ . The precision on this value is calculated by simply multiply:

$$P_{0,1m} = 0,1 \cdot 0,2\% = 0,0002\text{ m}$$

This corresponds to the precision on the maximum measurement possible.

The minimum measurement on the full scale range of the instrument is the resolution. In this sense, if a measurement corresponding to the resolution is carried out the precision on that evaluation is calculated with the same procedure.

$$P_{2\mu m} = 2 \cdot 0,2\% = 0,004\text{ }\mu\text{m}$$

In order to be compared with the other values this should be converted in strain. Hence, this value corresponds to the error due to the smallest measure that can be obtained. The sensitivity can be measured with the ratio between the precision calculated with respect to the smallest possible value that the device can measure over the length of the active zone. For this example, it has been considered a length of  $25\text{ cm}$ . Hence the sensitivity is:

$$\varepsilon_{\pm} = \frac{P_{2\mu m}}{LA} = \frac{0,004}{250000} = 0,016\text{ }\mu\varepsilon$$

### 1.5.3. Fibre optic system (Smartfibres)

Another *FOS* is the *FBG* system that is available in different configurations according to where it is displays in the structure. Two typologies of *FBG* systems are represented below. It has been considered one *SmartPatch* and one *SmartFBG* produced by *Smartfibres*.

Table 1.3: Performance of the Smart Patch [16]

	SmartPatch
Gauge length	6 mm
Strain range	$\pm 5000\text{ }\mu\text{strain}$
Strain sensitivity	$1,2\text{ pm}/\mu\text{strain}$
Strain resolution	$0,4\text{ }\mu\text{strain}$
Temperature range	$-30\text{ to }+60\text{ }^{\circ}\text{C}$
Temperature sensitivity	$11\text{ pm}/^{\circ}\text{C}$
Temperature resolution	$0,05\text{ }^{\circ}\text{C}$
Fibre type	Single Mode SMF

Table 1.4: Performance of the Smart FBG [17]

	SmartFBG			
Centre Wavelength	1528 to 1608 nm			
FBG Length	1mm	2 mm	5 mm	10 mm
Peak reflectivity	>-50%	>-50%	>-70%	>-80%
Strain range	$\pm 9000 \mu\epsilon$			
Strain sensitivity	1,2 pm/ $\mu\epsilon$			
Strain resolution	0,4 $\mu\epsilon$			
Temperature range	-270 to +85 °C (Acrylate coating) -270 to +300 °C (Acrylate coating)			
Temperature sensitivity	11 pm/°C			
Temperature resolution	0,05 °C			
Fibre type	Single Mode SMF			

The sensitivity of the *SmartPatch* is expressed in  $pm/\mu\epsilon$ . To express the sensitivities related to the smallest possible measure it is necessary a proportion considering the value of the sensitivities related to  $1\mu\epsilon$  of elongation. Hence, to obtain the corresponding sensitivity related to  $0,4 \mu\epsilon$  it is sufficient to multiply it to this value.

$$s_{0,4 \mu\epsilon} = 0,4 \cdot 1,2 = 0,48 \text{ pm} = 0,48 \cdot 10^{-9} \text{ mm}$$

This value has to be related to the initial length of the patch that corresponds to  $6 \text{ mm}$ . The strain sensitivity corresponding is reported below.

$$\epsilon = \frac{0,48 \cdot 10^{-9}}{6} = 0,08 \cdot 10^{-3} \mu\epsilon$$

The sensitivity of the *SmartFBG* is the same as for the *SmartPatch*. What changes is the length of the element that is variable. The sensitivity in terms of strain is expressed by considering the same formula used above.

$$\epsilon = \frac{0,48 \cdot 10^{-6}}{1} = 0,48 \cdot 10^{-3} \mu\epsilon$$

So it corresponds to 6 times the sensitivity calculated for the *SmartPatch*.

# Chapter 2

## 2. Smart Steel System

### 2.1. Explanation of the type of innovation

The SHM of existing structures is a procedure that requires the usage of several devices to accomplish in the process of evaluation of the health of the structure. In the years, the research has been developed in order to enhance procedures and tools for the evaluation. This copes with both the technical and economic aspects that aim to obtain a more performant device able to collect data with a low impact on the costs. The introduction of the *Smart Steel System (S3)* aims to a continuum recording of the data using a low-cost and very small device such as a *MEMS (Micro Electro Mechanical System)*. Thanks to this device it is possible to measuring the deformation of a structure in every moment from the application of the load by monitoring simple parameters, such as pressure and temperature, and evaluating the changing in volume of the device.

### 2.2. Difference with the standard devices

The advantages on the use of this element are several. First of all it is possible to embed the device into the structure. This was not possible for all the devices seen in the previous chapter. Most of the devices described in this thesis are largely used in the field of *SHM*. Every single device has different peculiarities and principle of working. Hence, it needs to be applied differently in order to collect the data from the structure. For example, the strain gauges are nowadays used everywhere in both research and practical field. These devices are cheap and accurate but the problems are that they are surface devices that need to be glued on the element. This entails the *SG* are not protected, hence they cannot be used in a field application to monitor constantly the deformation of an infrastructure. *Accelerograms* are optimum devices in the measurement of quantities with extreme precision. The limit in this case can be represented by the cost of the instrumentation needed to monitor the structure equipped with the accelerogram. Nevertheless, collecting data will be difficult to be performed on all the structure continuously since the accelerogram are scattered on critical point of the building. *FOS* are the most effective in the evaluation of the deformation of an element continuously. The problem is that the cost for the application

is high and most of the time cannot be afforded to have a full scale analysis of the building.

In this view, a low-cost embedded piezoresistive *MEMS* allows to balance all of these characteristics and collect deformation and state of stress of the structure through a strain-sensitive sensor which is embedded into the steel rebars. This guarantee to the sensor protection against the aggressive corrosive environment and avoid the noises generated by possible loss of friction [23].

The *S3* is a new way of monitoring the health of the structure by exploit the possibility of calculating the changes in temperature and pressure inside the cavity where the sensor is embedded. This method allows the calculation of the variation of volume that occurs in the bars by simply applying the law of the ideal gas.

$$\frac{\Delta V}{V_0} = \left(1 + \frac{\Delta T}{T_0}\right) / \left(1 + \frac{\Delta p}{p_0}\right) - 1$$

Performing the tests allows the evaluation of the axial straining only after an important phase of calibration. The basic concept beyond the calibration is constituted by distinguish the two different sollicitation that can determine the axial deformation of the cavity. In fact, this is the result of a combination of mechanical stresses and thermal stresses. This can be expressed by the following formula.

$$\frac{\Delta V}{V_0} = \left(\frac{\Delta V}{V_0}\right)_M + \left(\frac{\Delta V}{V_0}\right)_T$$

The first operation that is carried out on the rebar is the thermal calibration. This is carried out by determine the quantity of axial deformation which is affected by a variation of temperature in an unloaded phase.

$$\left(\frac{\Delta V}{V_0}\right)_T = \left.\frac{\Delta V}{V_0}\right|_{unloaded} = f(\Delta T)$$

After this first step is possible to proceed with a mechanical sollicitation of the beam in order to evaluate the axial deformation by considering a multi-step increasing load. In the first applications of this innovative techniques two approaches have been used to perform and quantify the mechanical stresses on the rebar. This cope with evaluation of the axial force  $F$  and the evaluation of the corresponding strain. Hence, two function have been introduced, these are:

$$\begin{aligned} \left(\frac{\Delta V}{V_0}\right)_M &= g_1(F) = \frac{F}{k_1} \\ \left(\frac{\Delta V}{V_0}\right)_M &= g_1(\varepsilon) = \frac{\varepsilon}{k_2} \end{aligned}$$

Where  $k_1$  and  $k_2$  are respectively two mechanical calibration coefficients [23].

The mechanical calibration is a uniaxial tensile stress where the loads is applied in cycle of 8 steps with an increment of 5  $kN$  each in condition where the temperature condition

were uncontrolled in the first application. The load is considered in order to maintain the bar and the region around the hole applied in it in an elastic state, avoiding the formation of plastic deformation. The thermal and mechanical calibration are the most important passages to complete before performing the experimental test to check the deformation of an element subjected to external load. It is important to highlight that, without a calibration, massive errors would have been registered, in order to understand the behaviour of the *MEMS* under environmental modification during the tests.

### 2.3. Progress during the study

The first approach in the study of this device was carried out in laboratory with the performing of a 4 point bending test with the purpose of comparison with the most commonly used devices for structural monitoring that are the strain gauges. Both were used and positioned along the beam in order to explore the truthfulness of the recording made by the *S3*. The experiment was successful and provides differences in results according to the position of the device and according to the intensity of the load. In particular, the result shown as the repetition of the load with an increasing value of the maximum effort at each cycle produced a very reliable result at high value of tensile stresses while it is recorded a noise, that can be neglected, when the value of the effort is maintained low.

Furthermore, during the experiment it has been recorded a failure of several gauges due to their detachment related to the increase of the load. Instead, it is possible to affirm that the failure of the *MEMS* do not deal with the failure of the device. It is reached because the cavity enters in a plastic deformation stage that leads to the loss of the sealant that hold the volume of the cavity and provokes a wrong reading in the variation of linear elongation of the element.

The development of the device has been focused on the robustness and durability of the *MEMS*, obtaining solution that aims to reduce the noise at low level of straining deformation and implementing the deformation reading. Furthermore, an analysis of the shape and the presence of the ribs has been performed in the next sections in order to improve the reading and aims to the standardization and commercialization of the devices.

The first study that aims to improve the research to adapt the device to a wide and simpler use has been focused on the elaboration through software [6]. The analysis has been elaborated through Finite Element Method software which considered the geometries and the properties of the material used. Many constitutive laws have been tried in order to obtain the optimal configuration that gives results that are comparable with the real behaviour of the beam. The analysis has been carried out exploiting different constitutive laws for the material and evaluating the variation of pressure in the air cavity. Furthermore, a field test evaluation has been performed.

As a first operation the model through the software has been developed by using the software *ADINA 9.4* in order to create the element and analyse the action and the

deformation. This has been than compared to a Matlab script where the element studied are function of the quantity of the nodes that define each finite element. The definition of the element was fundamental to describe the structure and define the responses in terms of stresses. Once that the structure has been defined the study continues by analysing the constitutive law of the steel rebar. At first the rebar has been analysed without any cavity and it has been tested in order to understand the deformation of it under an axial load. The element is analysed with the FEM software and only an eight of the rebar is considered. The deformation on the rebar is applied considering a displacement of 5 *mm* along the longitudinal axis. This allowed to calculate the first deformed shape and to analyse the constitutive load of the FEM element, which results very similar to the constitutive low of the *B450C* until the fracture of the rebar.

The first application of the cavity in the finite element model of the rebar has been carried out on the same rebar with a  $\Phi 20$  diameter. The cavity has been properly shaped and the boundary conditions are defined in order to obtain the correct deformation and data when the deformations will be imposed. It has been modelled one eight, one quarter and an entire smart steel rebars in order to consider the shape and geometry of the cavity in the element. The deformed shape of the beam has been evaluated in order to obtain the variation of geometry of the cavity. This implies a variation of volume and pressure that corresponds to a variation of volume following the equation of the ideal gas. The results have been carried out considering the cavity containing only uncompressible air in a first approach. This test has been followed by the analysis of the cavity containing an object with a different density compared to the air and this corresponds to the *MEMS* contained in the hole. During the study it has been demonstrated that it is possible to proceed with the analysis by neglecting the presence of an extra undeformable steel element inside the cavity. In fact, it is necessary to account for a reduction of reduction of pressure considering the fact that the deformable volume is reduced due to the presence of this element.

After a first phase of calibration, thermal and mechanical, it has been proved that the device gives valid results under the elastic regime and can withstand to a tensile load application to an early plastic deformation. The results up to this step of study shows that the device is not able to respond in a proper way under plastic deformation. Furthermore, this study brought an evaluation of the sensitivity considering 4 different constitutive lows for the steel. The summary of the results obtained are reported in the following bullet list:

- The elastic branch of the curves of the transducers placed in the first and third hole are really similar to the elastic branch of all the 4 constitutive lows experienced with the FEM model, while they are slightly different from the behaviour in elastic deformation of the transducer in the second cavity;
- The force-displacement diagram shows that the behaviour described by the transducers in the three cavities can be approximated to the second model where it has been selected a yielding stress with a reduction of the 4% with respect to the first and original model;

- The three models have different behaviour according to the variation of the maximum straining selected for the experiment. In particular, the maximum strain increasing shows a reduction of the ultimate value at failure and a corresponding increase of the ductility of the element.

After the tensile test calibration of the rebars it has been performed the 4 point bending beam test, in order to understand at which point the beam will failure and what is the response of the devices under the external load. To highlight the response of the device 18 cycles have been performed in order to understand how the *S3* devices record the straining and deformations. The study [6] compare three different level of load pointing out the influence of the noises that influences the readings of the instrument. It is possible to see a decrease in the influences of the noise by an increasing the value of the load applied to the sample.

The second study focused of the air cavity and the possibility of filling the cavity for future field application in order to improve the sensibility of the bar. Nonetheless, it also focussed on the shape of the hole and how much a different shape can affect the local stress concentration on the edges of the hole. In particular, the shape analysis has been carried out considering a coefficient  $K_T$  which is expressed by:

$$K_T = \frac{\textit{Highest value of stress at a discontinuity}}{\textit{Nominal stress at minimum cross – section}}$$

It was also demonstrated that not only the shape but thickness and width influence the value of this coefficient. On the other hand, the presence of fluid inside the cavities improved the sensibility of the instrument in order to improve the variation of pressure read. The main reason is to assume a strain variation of  $1 \mu\epsilon$  with at least an increase of  $1 Pa$ , which is the minimum read that the sensor can accomplish.

The first part of this research focused on the relationship between the stress along the two directions in the cavity. In particular, how the increment of the dimension of the hole, initially considered in a plate, influence the variation of the response of the element in correspondence to edges of the hole. It is important to consider the inclination of the hole, in case of non-circular shape, with respect to the application of the load. For simplicity the application considered the hole with the load parallel to the biggest axis of the element. In this case, the peak of the load is considered in the intersection between the axis perpendicular to the load and the edges of the cavity.

Furthermore, the study focused on the amplifications of the stresses in the edges of the cavity and the variation of the conditions by varying the dimension of the two principal axis. The initial dimensions consider the shape of the cavity as a circle, so the axis have the same shape. The vertical axis of the hole remained constant along the different dimensions taken while the variation is recorded in the horizontal one.

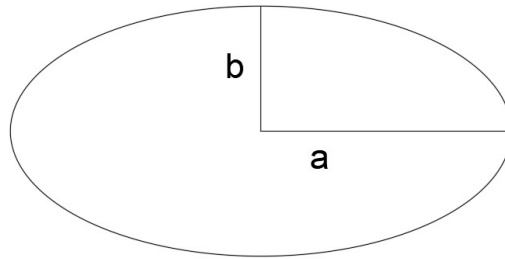


Figure 2.1: Axis of the cavity [12]

This implies a variation of  $K_T$  as it is possible to understand from the formula above. Particularly, it has been registered a decrease in the value of the  $K_T$  corresponding to an increase of the value of the semiaxis  $a$ . The study registered the deformation of a quarter of a beam in order to measure the stress and the plasticization of the element due to the presence of tensile load.

The problem with the elliptical hollows dug into the rebar is that with the tools available it is complicated to perform a hole with such a shape. To obtain a typology that can be realised easily and give the possibility to optimize the commercialization of the system, it has been studied the slotted cavity which are much easier to perform and obtain. The dimensions used for the holes are the same used for the elliptical cavity but this time it has been registered different stresses and a variation of the concentration of the stress on the internal perimeter of the cavity.

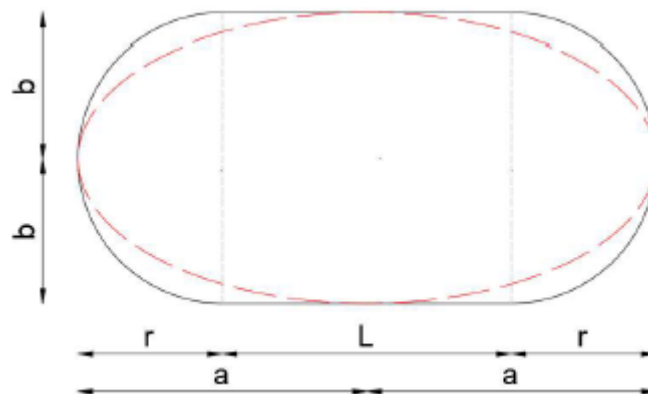


Figure 2.2: Elliptical and slotted hollow comparing [12]

The comparisons between the three different configurations (circular, elliptical and slotted) show some differences in the response of the cavity and in the stress concentration. As it has been explained and demonstrated in the study [12] the higher stress concentration is for the circular holes. In particular, the smaller the cavity the lower is the stress concentration. Among the three the elliptical hole resulted as the optimal one but on the counter side it results as the most complicated to be realised. Hence, it is the most expensive to realise. The slotted hollow shows an average behaviour in between the circular and elliptical hole, with the highest stress concentration that is located in the point corresponding with the change in concavity between the straight part and the circular part of the cavity, in the perpendicular direction of the load. The values of the stress are although comparable and competitive with those registered with in the elliptical cavity.

For the three types of cavities it has been registered a decrease of the stress going from the top to the bottom of the cavity. Thus, if it is considered a point in the cavity, the closer that it is along the x axis to the sealant, the higher the concentration of the stress is.

The same analysis has been carried out both in plate and bar. It aimed to obtain the evaluation of the  $K_T$  for both plate and rebars, with respect to the changes of dimensions. Here below the comparison of the studies is shown.

Plate with radius hole of 2 mm	$K_{t,average}$	$K_{t,max}$
Plate circular hole (a=2; b=2)	2.97	3.29
Plate elliptical hole (a=3; b=2; L/2=1)	2.42	2.56
Plate elliptical hole (a=4; b=2; L/2=2)	2.14	2.22
Plate slotted hole (a=3; b=2; L/2=1)	2.46	2.70
Plate slotted hole (a=4; b=2; L/2=2)	2.36	2.59

Steel bar with radius hole of 2 mm	$K_{t,average}$	$K_{t,max}$
Bar circular hole (a=2; b=2)	2.98	3.44
Bar Elliptical hole (a=3; b=2; L/2=1)	2.58	2.77
Bar Elliptical hole (a=4; b=2; L/2=2)	2.31	2.44
Bar slotted hole (a=3; b=2; L/2=1)	2.42	2.74
Bar slotted hole (a=4; b=2; L/2=2)	2.27	2.58

Plate with radius hole of 1.5 mm	$K_{t,average}$	$K_{t,max}$
Plate circular hole (a=1.5; b=1.5)	2.84	3.09
Plate elliptical hole (a=2.5; b=1.5; L/2=1)	2.23	2.34
Plate elliptical hole (a=3.5; b=1.5; L/2=2)	1.93	2.00
Plate slotted hole (a=2.5; b=1.5; L/2=1)	2.26	2.47
Plate slotted hole (a=3.5; b=1.5; L/2=2)	2.17	2.37

Steel bar with radius hole of 1.5 mm	$K_{t,average}$	$K_{t,max}$
Bar circular hole (a=1.5; b=1.5)	2.82	3.32
Bar Elliptical hole (a=2.5; b=1.5; L/2=1)	2.42	2.63
Bar Elliptical hole (a=3.5; b=1.5; L/2=2)	2.15	2.27
Bar slotted hole (a=2.5; b=1.5; L/2=1)	2.28	2.48
Bar slotted hole (a=3.5; b=1.5; L/2=2)	2.10	2.31

Figure 2.3: Comparison of the different models studied [12]

As it is possible to understand from the values of  $K_T$  the smaller is the hole the lower is the shape coefficient. A different behaviour can be seen if it is compared the holes with the same radius if they are in a plate or in a rebar. In particular, it is possible to see that

in a plate the elliptical holes are more efficient in terms of  $K_T$ . In the meanwhile, the rebars registered the opposite behaviour.

A further consideration has been made also in order to consider the position and the dimension of the ribs of the bars in the element.

The study focused mainly on another aspect of the interaction between the cavity and the rebars. In particular, it focused on the sensitivity of the *MEMS* that is located in the element with respect to a possible fluid contained in the element. Up to this point it has been studied the variation of pressure and volume inside the cavity with only the presence of air. The focus has been shifted to the possibility of insert another incompressible fluid in order to increase the pressure and improve the sensibility of the instrument. The presence of this has been simulated in this study by change the density and the elastic characteristics of the potential fluid.

At the beginning it has been considered a quantity of material such as the minimum variation of pressure measured by the *MEMS*, that for the device used is equal to  $1 Pa$ . The first steps aim to find the configuration and balance of incompressible fluid and air in order to obtain the equivalence  $1 \mu\varepsilon = 1 Pa$ . After the trial with only air and the application of a simple proportion it has been found that the quantity of fluid and air inside the cavity should be 77,50% and 22,50%, respectively.

This configuration can be improved by increasing the level of incompressible fluid inside the cavity that will result in a better sensibility of the instrument. The study [12] shows that the proportion between the increment of fluid and pressure is not directly proportional. Instead, it has a hyperbolic increase as it is shown by the following image, that is implied by the fact that the fluid is incompressible. Hence, it has been focused on the calibration of the quantity of fluid in order to have the best sensibility of the element.

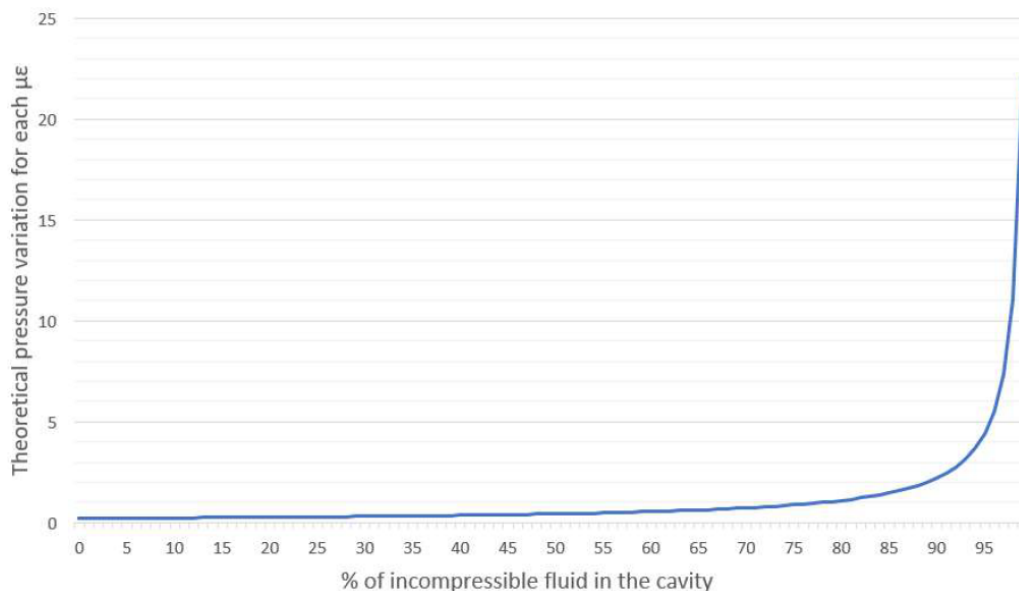


Figure 2.4: Comparison of pressure recorded by the *MEMS* with an increasing percentage of fluid in the cavity [12]

It is possible to see a rapid increases after a certain value of fluid inside the cavity. Thus, it has been necessary to understand which one is the optimal content that corresponds to a pressure increase or decrease that is capable to be detected by the *MEMS* when

the rebar is subjected to a tensile or a compressive stress. Hence, it is useful to balance the sensibility of the instrument with the range of pressure variation detectable. The study shows that the best sensibility that leaves the variation of pressure within the range detectable is 90,63% of fluid. So the interval between 77,50 % and 90,63 % inside the cavity gives the possibility to improve the sensibility in terms of pressure readings but more than that maintains the readings within the range feasible by the device. This is also due to the elastic-plastic behaviour of the bar and the hole cross section. According to this, the study reports a comparison based on the plasticity of the hole bar and the cross section. It shows that the plasticization of the entire bar corresponds to a strain of the cross section equal to  $18532 \mu\epsilon$ . Hence, it shows as the plasticization of the cross section happens firstly, while the hole bar is plasticized in a second time. To consider this behaviour it has been selected two different laws of the material, considering it isotropic linear elastic and plastic-multilinear comparing when the first plasticization happens in order to understand when the hole begins the plasticization. To do that it has been calculated an *angular coefficient* that shows how much the pressure changes with the variation of the strains in different steps as a difference in between the two different constitutive laws hypnotized above. The result shows that the angular coefficient is always linear for the first laws while it changes, increasing in a nonlinear shape, after the first plasticization of the cavity.

The study hypnotizes and also calculates the effect of the temperature on the rebar. In particular, this factor is considered as a variation of pressure alone and together with the mechanical load from the outside. Again the evaluation has been performed with the cavity empty and filled with the 90,63 % of fluid. The angular coefficient is also calculated in this case, pointing out a linear behaviour for both the conditions of the cavity but with a difference of  $37 Pa$ . Combining the mechanical and thermal actions it is possible to see how much the pressure variates with the variation of temperature for different load cases. The result of this analysis provides a different behaviour between the cavity empty and full of incompressible fluid. In particular, it shows an improvement in the reading with the cavity full of incompressible fluid because the presence of the fluid allows a bigger increase in pressure with the same variation of temperature.

## 2.4.Sensitivity of S3

As the previous studies have been pursuit, one of the most important parameters is the improvement of the sensitivity of the S3. In the previous chapter, it has been compared the different sensibility that is characteristics of the common SHM system such as *Strain Gauges* and *Fiber Optic System*. In this paragraph, an evaluation of the sensibility based on experimental data have been carried out in order to obtain the strain sensibility of the instrument and, eventually, compare the results with the previously mentioned devices.

In order to perform the evaluation of the sensibility it has been considered the model of MEMS used for the evaluation. The device is a miniaturized Digital Barometric Air Pressure Sensor. The properties of the sensor are displayed in the table below.

Table 2.1: Characteristics of the digital barometric air pressure sensor

Parameter	Value	Unit
Measurement range	1013.25	hPa
Accuracy	±0.1	hPa
Precision	±0.01	hPa
Resolution	0.01	hPa
Temperature range	-40 to 125	°C
Temperature coefficient	±0.01	hPa/°C
Measurement time	100	ms
Power consumption	100	µA
Output	I2C, SPI	-

It is possible to distinguish three types of sensibilities here. The absolute pressure accuracy corresponds to the accuracy related to the entire measurement range of the element while the relative is related to the measurement considered. The pressure sensor precision is the feature related to the sensitivity of the instrument and corresponds to the smallest possible variation that the instrument can record. It is important to point out range and accuracy of the temperature too and understand how the behaviour of the sensor under temperature changes is. Furthermore, variations of temperature influences pressure. The parameter to measure how much the temperature variate under increase or decrease of temperature is shown in the table. This is related to a reference temperature which is 25 °C, but it is expressed in Pa/K. Measurement time is able to express the velocity of output of the results from the sensor and helps to understand how many evaluations can be done in a certain amount of time.

As it has been mentioned in the previous paragraph the increases of load are set to be of 5 kN at each step. This is converted in a variation of pressure measured from the data equivalent to 50 Pa. In order to obtain the strain during the loading test, the applied force has been divided by the axial stiffness of the rebar. The axial stiffness of the element is calculated as a product between the effective area and the Young Modulus of the rebar.

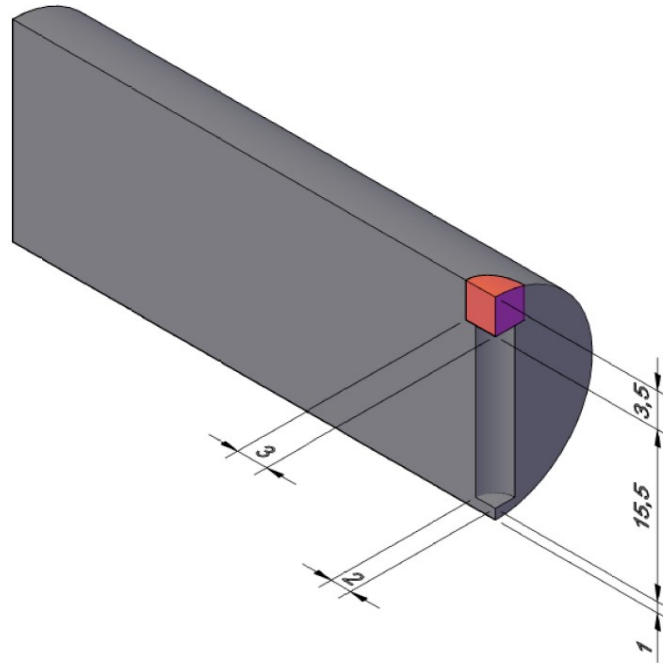


Figure 2.5: Dimension of the cavity [6]

The effective area is considered as the area perpendicular to the longitudinal tensile stress considering the section in correspondence with the cavity. The effective area is considered as:

$$A = \pi \left( \frac{D^2}{4} \right) = \pi \left( \frac{20^2}{4} \right) = 314,16 \text{ mm}^2$$

$$A_{cavity} = A_{void} + A_{sealant} = (3,5 \cdot 6) + (4 \cdot 15,5) = 21 + 62 = 83 \text{ mm}^2$$

$$A_{eff} = A - A_{cavity} = 314,16 - 83 = 231,16 \text{ mm}^2$$

The straining considering an elastic modulus equal to  $E = 200000 \text{ MPa}$  is:

$$\varepsilon = \frac{F}{A_{eff} \cdot E} = \frac{5000}{231,16 \cdot 200000} = 0,00010815 \varepsilon = 108,15 \mu\varepsilon$$

To evaluate the sensitivity, it should be taken into account the precision of the instrument in terms of force. In particular, the value of  $0,002 \text{ hPa}$  needs to be expressed in its equivalent in  $kN$  and then repeat the procedure above.

$$50 \text{ Pa}: 5 \text{ kN} = 0,2 \text{ Pa}: x$$

This gives the possibility to calculate the correspondent value in force, which is:

$$x = \frac{5 \cdot 0,2}{50} = 0,02 \text{ kN}$$

Adding this to the force corresponding to the step by step increase, once obtains.

$$\varepsilon_{\pm} = \frac{F_{\pm}}{A_{eff} \cdot E} = \frac{20}{231,16 \cdot 200000} = 0,00000043 \varepsilon = 0,43 \mu\varepsilon$$

## 2.5. Comparison between the sensitivities

The different sensitivities found for the devices that have been developed in this paper can now be compared together, in order to exploit the features of the systems.

Table 2.2: Sensitivity comparison

Device	Sensitivity
Strain gauge	0,003 $\mu\epsilon$
FOS	
SOFO	0,016 $\mu\epsilon$
SmartPatch	0,08 $\cdot 10^{-3}$ $\mu\epsilon$
SmartFBG	0,48 $\cdot 10^{-3}$ $\mu\epsilon$
MEMS	0,43 $\mu\epsilon$

The values of sensitivities of the instrument as it is possible to see in the table above are in the order of cents, thousands of microstrain and even smaller for the *FOS*. So it corresponds to the optimal device to consider for what concerns the sensitivity. It is important to understand and compare all the factors that affect the selection of the correct device for the monitoring of the deformations in the structure considered.

The first one, the *Strain Gauge*, corresponds to the most reliable and used device both for the simplicity of the use and the sensitivity as it is represented in the table above. The variation of 0,003  $\mu\epsilon$ , with respect to the minimum variance of resistance that can be detected, demonstrates that these tools are extremely accurate in the evaluation of the elongations. Furthermore, it is necessary to point out that the sensitivity increases with the increment of variation of resistance, so for small measurements it is possible to have readings that are more truthful.

The *FOS* devices are highly considered in the most recent techniques for the *SHM*. This, as it is possible to highlight from the table, is also due to important values in terms of sensitivities that are, especially for the *SOFO* technology, really close to the one calculated for the Strain Gauge. Even more quality is represented by the *SmartTech* devices that reach sensitivities of tens and cents of nanometer. It is important to point out that these values improve with the increase of the length of the instrument, assuming that, for the Smartfibres technology considered in this paper, it varies in a range that goes from tenths to cents of nanostrain. This high level of measurement is reached using a technology that needs to be applied in major part of the structure for a complete monitoring. Furthermore, these devices are displayed in cables that have a considerable cost, hence it influences the strategy of monitoring used for the structure designed.

The *MEMS* proposed in this paper has a sensitivity that is close to the one calculated for the *SOFO* technology. That means that in terms of truthfulness this innovative technology is capable to offer an important contribution to the *SHM*. This is correlated to the possibility of embedding the devices in the structure to guarantee a continuous

and solid monitoring of the elements. This option is, with respect to the *Strain Gauges*, a solid improvement because it gives the possibility to explore a monitoring of the structure that is more reliable and less inclined to failure due to exposition to the environment. The possibility to scatter the devices and the low cost of them is a great opportunity to provide a more complete monitoring of the structure. The great sensitivity of this element provides a truthful device that can compete with the *FOS* in these terms. With low cost and a high sensitivity it is possible to have a complete monitoring of the building and guarantying a strong role in the innovative Structural Health Monitoring techniques. Furthermore, studies that have been and will be performed aims to improve the reliability of the apparatus and increase the simplicity of application.

# Chapter 3

## 3. Case study

This chapter has the goal of describe the practical approach and the description of the case in which the device has been installed.

The preparation of the rebars has started from understanding the best procedure to seal the cavity that contains the *MEMS* in order to create an environment completely efficient. This was a key problem of the whole experience, because according to this it the system is able to improve the collection of the data.

In this sense, a series of experience has been carried out during the whole period, giving the possibility of finding the final scheme that allows the installation of the system in place.

During this period, there have been carried out experiences of monitoring of samples in controlled environment where it has been possible to observe the variation of Temperature and Pressure. In fact, understanding the behaviour of the system gives the chance to obtain a huge background of information that helps to figure out future interpretations that can come out during the installation.

### 3.1. Description of the bridge

The purpose of the thesis is the application of the device in the field in order to obtain data for what concern the analysis of stresses and deformations. For this reason the device has been installed into a bridge in order to have data related to the deformation due to the traffic load and the self-weight of the structure.



*Figure 3.1: Photo of the bridge where the application is carried out*





*Figure 3.3 Data logger used in the application*

The instrumented rebars have been sealed through an epoxy resin and transferred in the construction site. The bridge as described before, has a main structure composed by five beams reinforced by secondary beam bolted to the main frame. The slab is made by precast reinforced predalles.



*Figure 3.4 Reinforcement displaced in the slab*

As a first operation, an analysis of the reinforced bars has been done in the construction site. The main goal was the location of the instrumented rebars in correspondence with the center line of the span.



*Figure 3.5 Longitudinal beam number one*

According to the plan the rebars have been located in axis with the first and second main beam starting from the external limit of the bridge. In particular, the rebars have been scrolled in between the reinforcements already set in place and linked to the closest elements. The rebars in particular have the following characteristics:

- Rebars number 1: Containing sensors 10, 11, 12, 13, 14;
- Rebars number 2: Containing sensors 20, 21, 22, 23, 24;
- Rebars number 3: Containing sensors 40, 41, 42, 43, 44;
- Rebars number 4: Containing sensors 30, 31, 32, 33, 34.

In particular, rebars number 1 and 2 have been displaced in axis with the first longitudinal beam starting from the outside while rebars 3 and 4 have been displaced in axis with the second longitudinal beam. Once that the device has been set in place and locked to the reinforcement the cables have been unrolled wired to the transversal reinforcement in order to set an exit point in correspondence of the kerb of the bridge. There the cables have been connected to the data logger and since that moment it has been possible to collection of data.



*Figure 3.6: Position of the instrumented rebar with respect to the reinforcement*

The provisional position of the data logger connected with the rebars is shown in the image below. This will be corrected allocated after the casting of the concrete, which phase will be giving the possibility to confront the deformation of the structure with the data that comes from the device set in place.



*Figure 3.7: Position of the data logger with respect to the instrumented rebars*

In fact, as it will be shown in the further chapter, all the phases of installation, transportation and implementation of the device has been recorded and transmitted to the server. These operations allow to monitor the values of temperature and pressure of the cavity during this phase but most important during the phase of the cast in place of the concrete. This set a regime of efficiency and sensibility of the instrument that will be discussed in the following chapters.

# Chapter 4

## 4. Experimental phase

In this chapter the analysis of the “S3” sensor have been developed, in order to understand the behaviour of the sensor in the cavity and the response to the different external actions. In particular, a tensile test has been performed on the element in order to evaluate the variation of pressure inside the cavity alongside with the temperature. A comparing with the previous analysis has been carried out in order quantify the improvements that the experimental phase has produced. Furthermore, a model has been created, using the software Robot Structural Analysis in order to repropose the same loads which the rebars are exposed during the different phases and evaluate the solicitations compared with the one measured by the sensors in the bridge.

### 4.1. Mechanical characterization of the instrumented rebars

The characterization of the rebars have been carried out in laboratory. In order to understand the response of the system to the deformation the rebars undergo to a tensile test in which the elements are subjected to an increasing load in different steps that will not arrive to the failure of the specimen. In particular, the rebars undergoes to two cycles of loading and unloading. Each cycle is composed by 12 steps in which it is applied a force of 5 kN for 1 minute. In particular the test will be performed in:

- 4 steps of increasing the tensile load up to 20 kN;
- 4 steps of unloading in which the load is brought to 0 kN;
- 2 steps of loading in compression up to 10 kN;
- 2 steps of unloading up to 0 kN.

Two of this cycle are repeated for each bar. The bars that have been tested are twin bars that match the characteristics of the instrumented rebars that have been cast in place in the bridge deck. It is reported below, the equipment used for the mechanical characterization of the rebars.



Figure 4.1 Hydraulic machine used for the tensile test

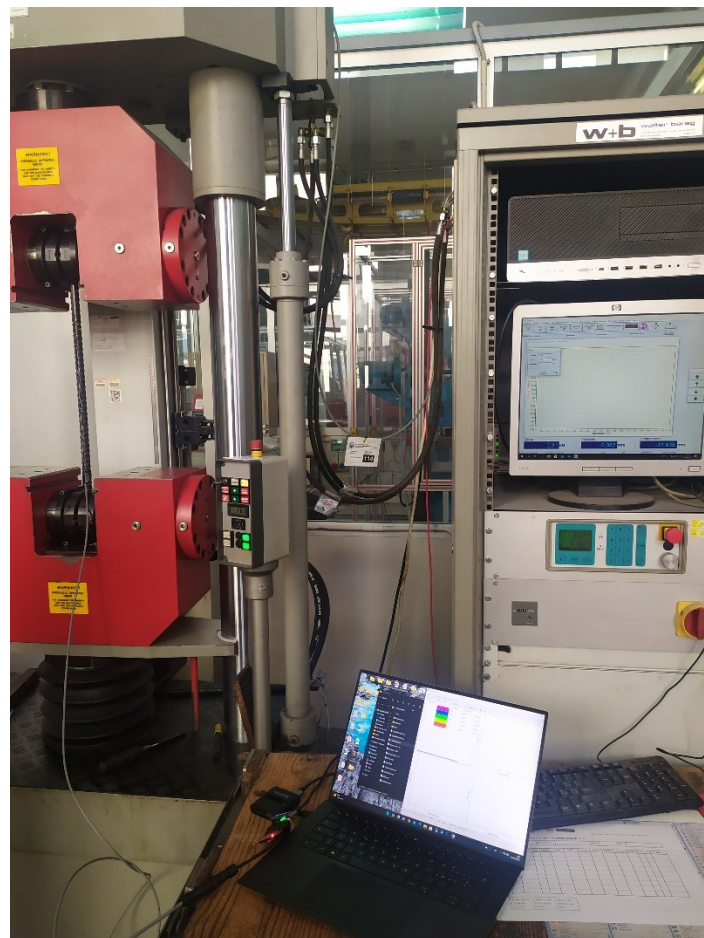


Figure 4.2 Full equipment used to perform the test on the rebars



*Figure 4.3 Detail of the rebars undergoing to the test*

In the photos it is possible to see the rebar embraced in the clamps of the tensile test machine. It possible to notice from the details of the images that the rebars have a groove dig for all their length which is completely sealed after the completion of the operation of embedding the sensor. The cable that come out from the bottom of the equipment represent the electronics system at which each sensor is linked through the PCB and then attached to a data logger to collect the data related to the monitoring. In this case, the data were collected by a wired acquisition system connected to a PC.

The test has been executed on four specimen which contains each one five cavities, for a total of 20 sensor available for the collection of the data. Furthermore, the elements have been exposed to a period of aging in controlled condition of temperature and pressure with the goal of monitoring the behaviour of the sensor in determined conditions.

Here below it is reported the experience on the second rebars which points out the results most significative in terms of temperature and pressure. The image as they come from the test describe a trend which is affected by the noise.

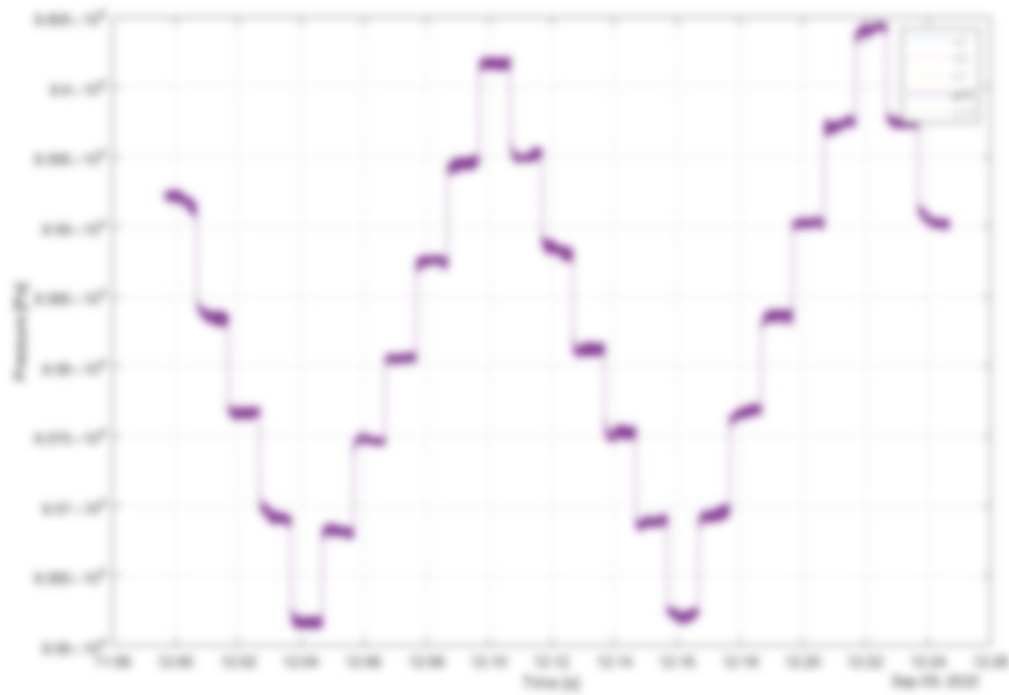


Figure 4.4: Sensor 11 in position 2 in rebar 2

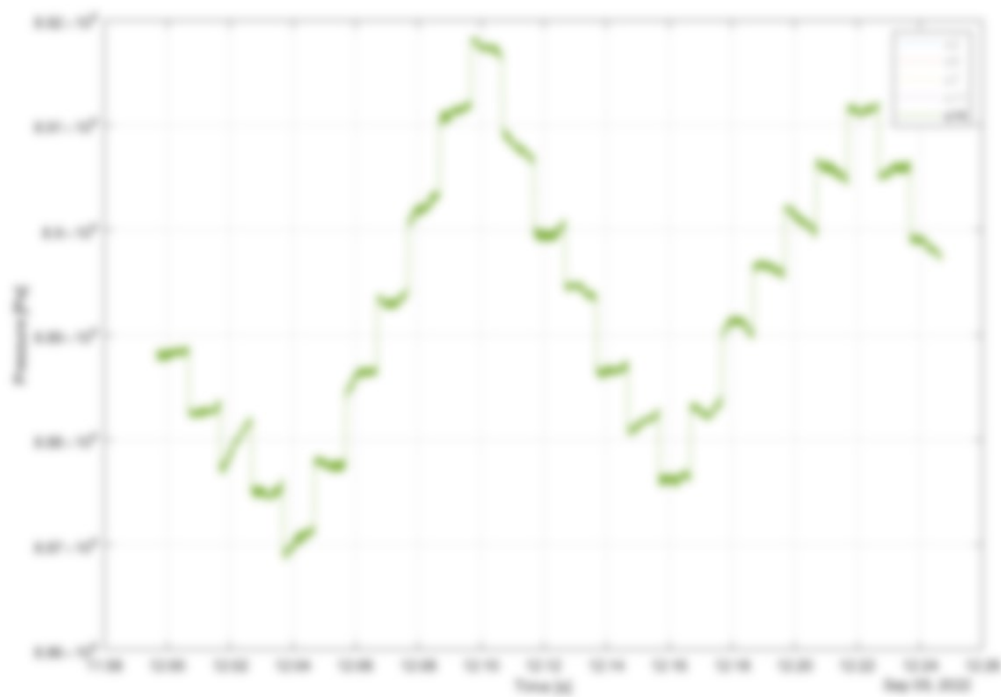


Figure 4.5: Sensor 14 in position 3 in rebar 2

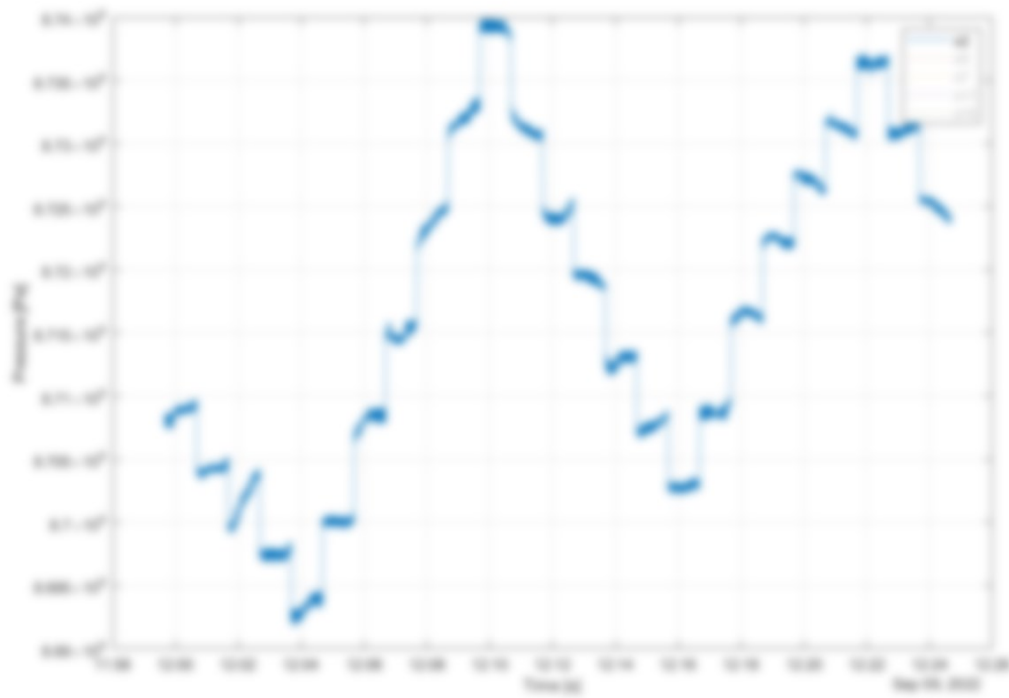


Figure 4.6: Sensor 2 in position 4 in rebar 2

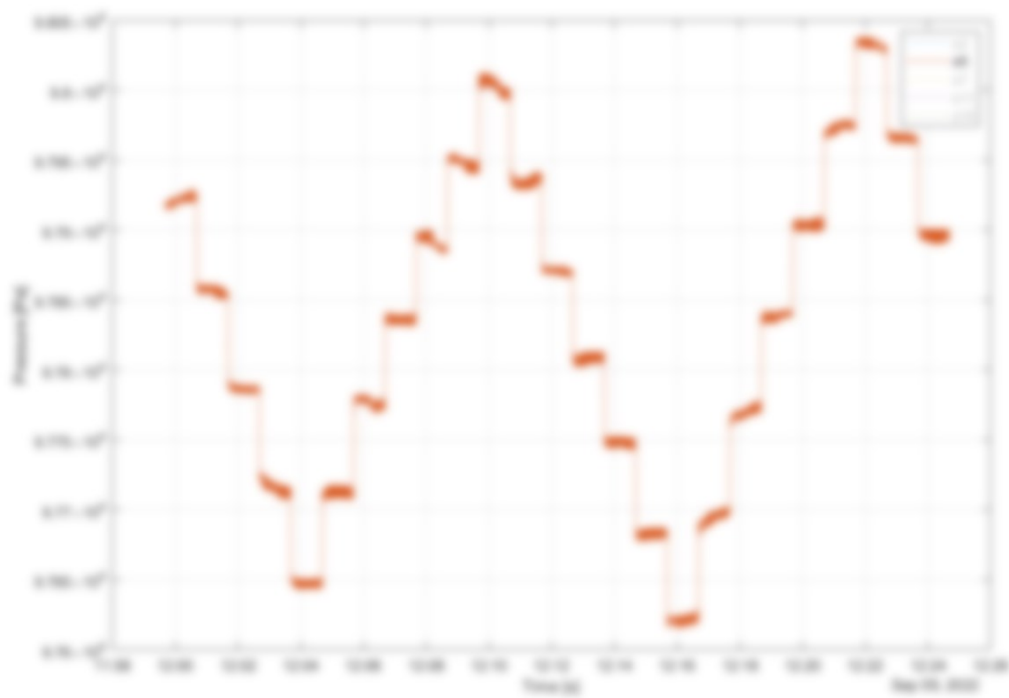


Figure 4.7: Sensor 5 in position 5 in rebar 2

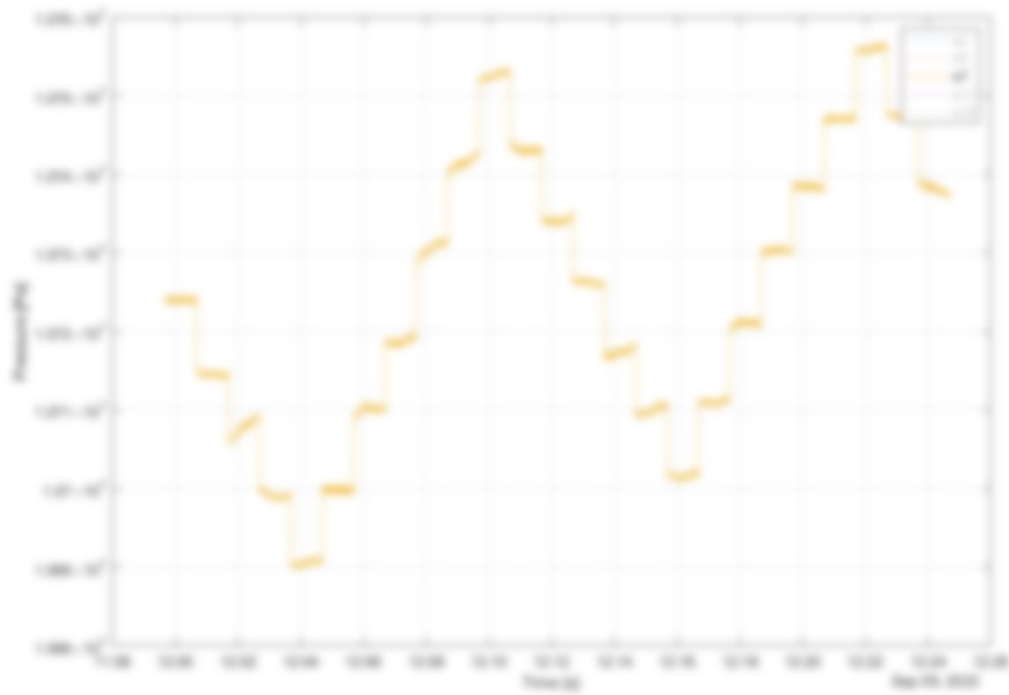


Figure 4.8: Sensor 7 in position 1 in rebar 2

The raw data underwent to a procedure of refining in order to smooth the final results and have a more linear representation of the values of pressure. Here below the data that passed through the improvement procedure.

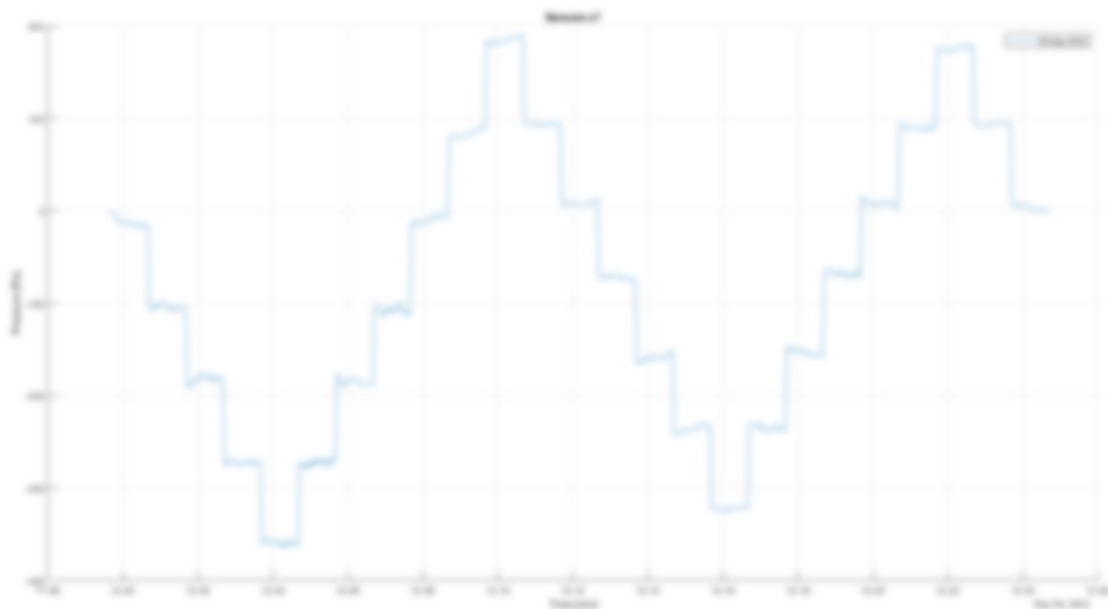


Figure 4.9: Sensor 7 in position 1 on rebar 2

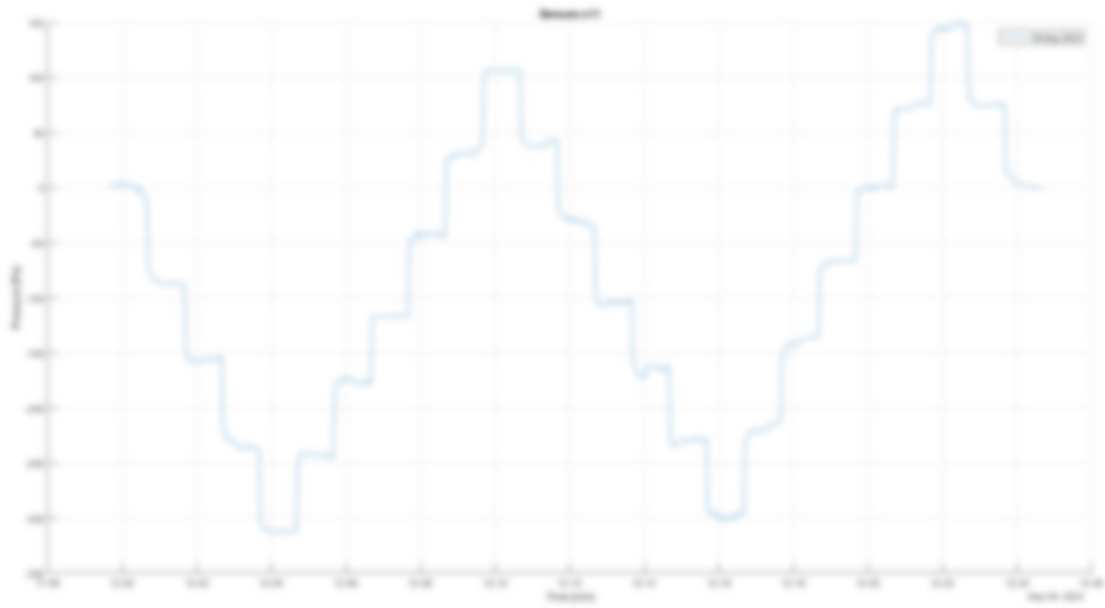


Figure 4.10: Sensor 11 on position 2 in rebar 2

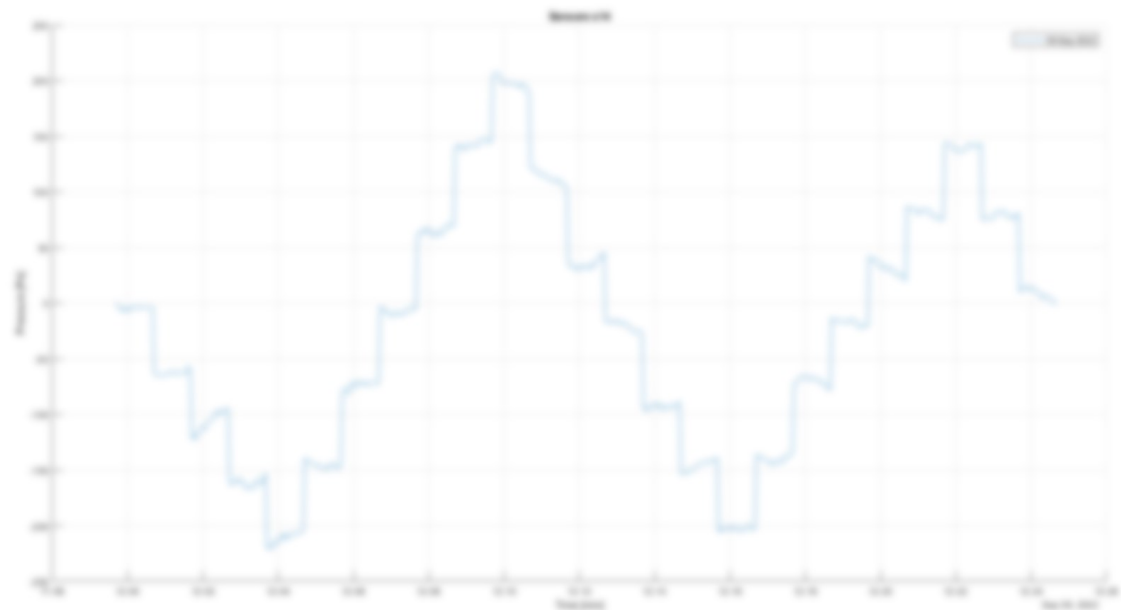


Figure 4.11: Sensor 14 in position 3 in rebar 2

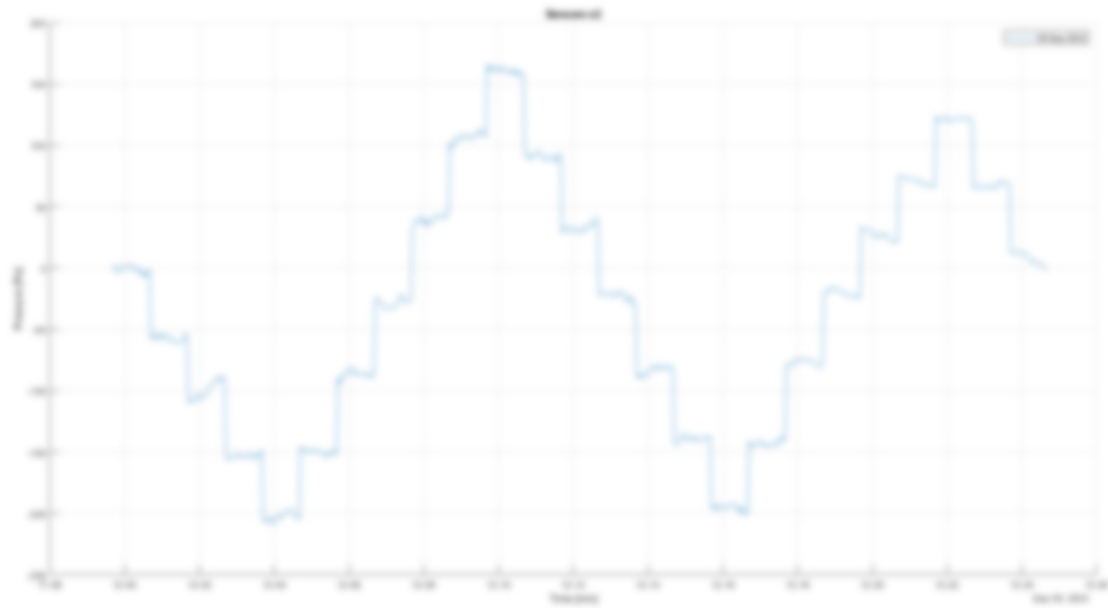


Figure 4.12: Sensor 2 in position 4 in rebar 2

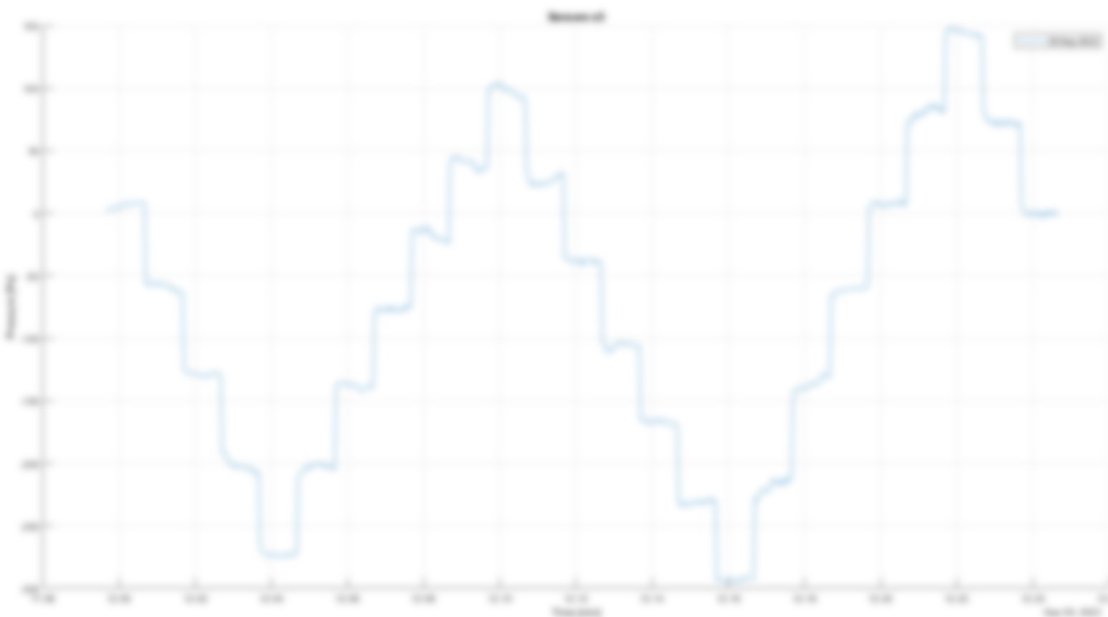


Figure 4.13: Sensor 5 in position 5 in rebar 2

As it is possible to see from the images the step recorded corresponding to a well-defined change in terms of pressure that is maintained almost constant for all the duration of the iteration. This means that the sensors have a solid performance allowing to detect an exact variation once that are subjected to a stress. I can be notice in the smoothed data that all the steps represent a determined quantity expressed in Pascal. In particular, it can be pointed out that the variation is always above the 50 Pa for every increase or decrease of 5 kN. This means that, with respect to the previous study from which it has been reported an increase of 50 Pa within each step it is possible to see an

improvement from a sensitivity point of view. This is well highlighted in the sensor number seven in the cavity number 1. Here, the steps are constant to a quantity equivalent to 100 MPa. To quantify the increase of sensitivity in this case it is reported the calculation represented also in the paragraph 2.42.4.

$$100 \text{ Pa}: 5 \text{ kN} = 0,2 \text{ Pa}: x$$

$$x = \frac{5 \cdot 0,2}{100} = 0,01 \text{ kN}$$

$$\varepsilon_{\pm} = \frac{F_{\pm}}{A_{eff} \cdot E} = \frac{10}{231,16 \cdot 200000} = 0,00000022 \varepsilon = 0,22 \mu\varepsilon$$

Thus, it is possible to see a sensitivity which is doubled with respect to the earlier stage of development of the system. In general it is possible to see mean value of step due to the application of the load in the rebar which is correspondent to 80 Pa. The difference between the sensor is related to the different configuration inside the cavity.

The resume of the strain sensitivity calculated on the base of the data collected in the tensile test is shown below. The column where the  $\varepsilon$  is calculated is referred to the sensitivity of the element

Table 4.1: Summary of the tensile test in the rebar number 2

The table report the value read for all the sensors that are embedded in the rebar number two. In particular, it is possible to notice in the first two columns the position in the rebar and the respective sensors displayed in it. In the third column it has been reported the percentage of fluid. It has been selected following the study made on the topic of Bandinelli [12] in order to improve the sensibility of the device.

An important outcome is represented by the variation of pressure corresponding to a step of 5 kN of increase in the rebar. This value, according to the precision of the sensor, need to be converted in kN as it has been shown in the chapter 2. The same procedure has been repeated per each sensor finding the force correspondent to that change and successively converted in microstrain to take into account of the sensitivity improvement. This showed that the best improvement is represented by the sensor 7 in position 3 of the rebars while it has an overall average of  $0,314 \mu\varepsilon$  detected considering the five sensors.

The same analysis has been repeated on 20 kN of difference representing the maximum force applied to the rebar during this test. The calculation on 20 Pa shown that the

average strain sensitivity slightly increases but remains on the same order of magnitude as support of the solid performance of the sensors.

As it has been mentioned before the specimen has been exposed to aging in controlled conditions. This operation is carried out in order to verify the sealing of the sensor in the specific cavity and to understand their behaviour with the new configuration.

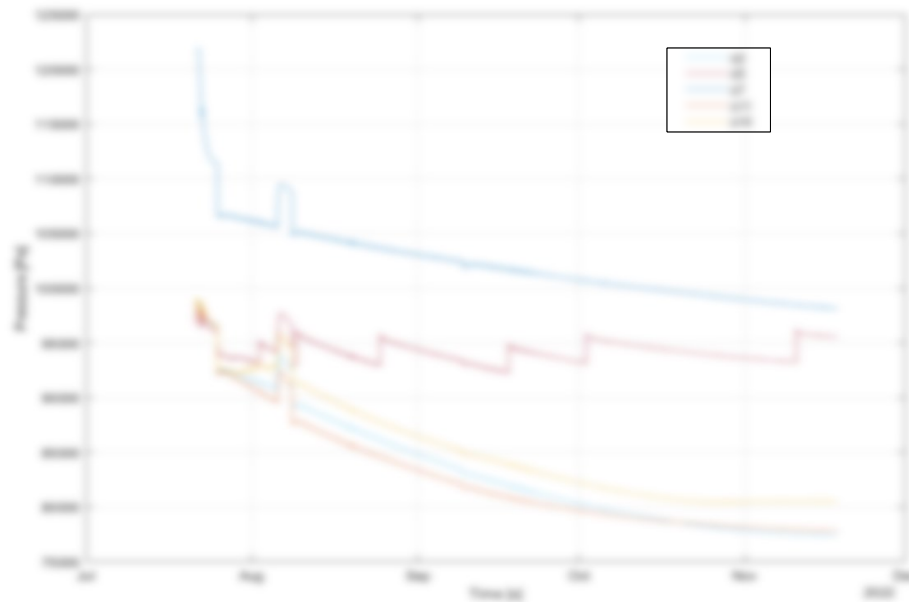


Figure 4.14: Monitoring of pressure of the rebar number 2

The monitoring of the rebar has started on July 21st, as it is possible to see from the diagram. It is possible to see the evolution of the pressure according to the time. A general behaviour can be extrapolated from this diagram. The behaviour of sensor 11, sensor 2 and sensor 14 have been almost identical for since the middle of August up to the last reading in 18<sup>th</sup> of November. In particular, it has shown a gradual decrease of the pressure that cope with the stabilization of the sensor and during the month of November it has been recorded an almost flat diagram due to the complete stabilization of the sensor in the diagram. Generally, this rebars has brought a constant behaviour of all the specimen embedded in the cavities. Exception made for the sensor 5 that, even though it follows the same descending trend, has shown some steps of increase of pressure maybe due to a possible technical problem. It is important to show that the sensors are subjected to the same peak in the first days of August due to the fact that has been moved from the aging chamber in order to test their condition in laboratory. This proved the solid response to a change of environment of the sensors and how their response will be helpful in the application in field.

As mentioned before the decreasing trend has last for the sensor up to the last days of October, showing a flat progress in terms of pressure that is compatible with the conditions of the chamber.

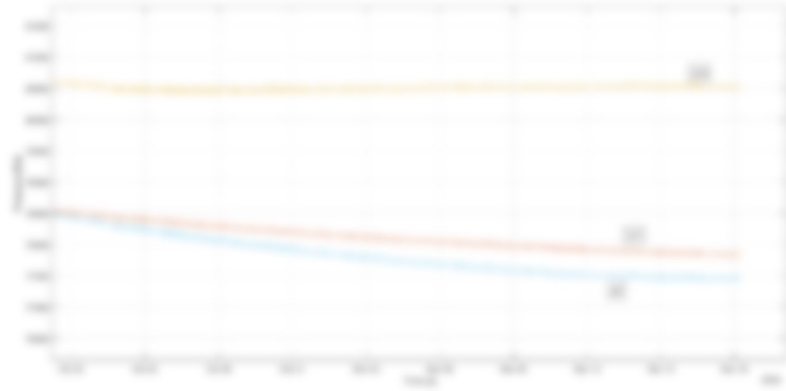


Figure 4.15: Final trend of the sensors 2, 11, 14

Here above, the zoom in of the last month of monitoring shows how there is a flat trend that settle the sensor s14 to a value of 80500 Pa, whilst the s11 and s2 that are not still completely settled, are showing a progress that is going to stop to approximately 77800 Pa for the s11 and 77500 Pa for the sensor s2.

On the other hand, the sensor s7 that has started the collection of data to a higher value of pressure has not showed yet a flattening of the curve of decreasing of pressure even though if it is gradually decreasing the gradient of decreasing of pressure.

A more uniform behaviour has shown in the monitoring of the temperature. Instead, this has been more constant than the pressure showed in the image below.



Figure 4.16: Monitoring of temperature of the rebar number 2

The diagram above confirms the stability in terms of reading of the temperature of the cavity in which the sensors have been displaced. This show the robustness of the sensors in reading of the temperature since the reading has been always constant to 19°. The only peak is due to the phase which has been already mentioned above in

which the rebars have been moved in laboratory to be analysed. Also here is important to point out the response of the sensors that recognise the higher temperature due to the summer season.

#### 4.2. Monitoring of the instrumented rebar in the bridge

As it has been reported in the chapter 3 the rebars has been displaced in the middle of the span of the bridge. There are for rebars containing each one 5 sensors within a distance of 25 cm one from the other. According to the schematization already given in chapter 3 it has been possible to evaluate the behaviour of the sensor in relation with the rebar but more important with the position of the instrumentation with respect to the slab. From the moment of the seal of the cavity the sensors started the acquisition of the data of pressure and temperature in order to proceed with the same step of the twin rebars that have been talked in the paragraph 4.7. Down below it is shown the behaviour of the specimen before the installation of them in the bridge's span.

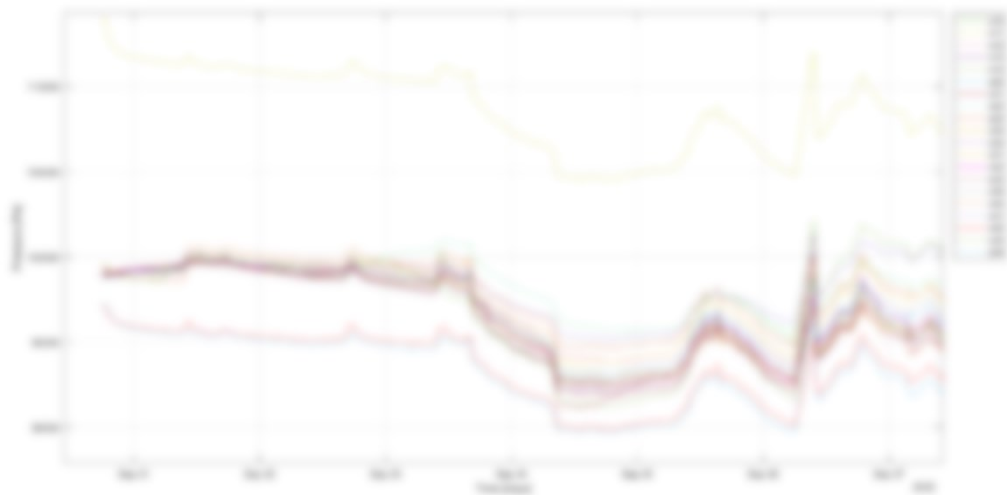


Figure 4.17: Monitoring of pressure before the installation

It is possible to highlight that from the moment of the beginning of the acquisition of the element the rebars are essentially more linear than the previous rebar shown in the paragraph before. This is essentially due to the fact that the instrumented rebars will undergo to another process that do not request the monitoring in an aging chamber in controlled conditions. During the first day, up to the 21<sup>st</sup> of September at around midday it is possible to see a decreasing of the values of pressure and temperature that is also recognisable in the rebar 2 previously mentioned. During these early days of monitoring the trend, even if slightly descending, it shows an almost constant behaviour that is symptom of stability. The small peaks recorded up to the 23<sup>rd</sup> of September are due to operation in the laboratory at which the specimens responded correctly.

It is particular important to point out the behaviour recorded in between 23<sup>rd</sup> and the 25<sup>th</sup> of September. In fact, in these days it has been registered a lowering of the pressure due to the environmental conditions. The temperature, and alongside of it the pressure,

has lowered due to a rain precipitation that brought a decrement of few thousand of Pascals inside the cavities. After these days, the pressure is increased again and in the last day before the installation the progress does not follow a particular trend because the instrumented rebars have been moved outside and checked for the last details before the cast in place in the site.

At the same time a diagram of the temperature has been recorded, producing the following outcome.

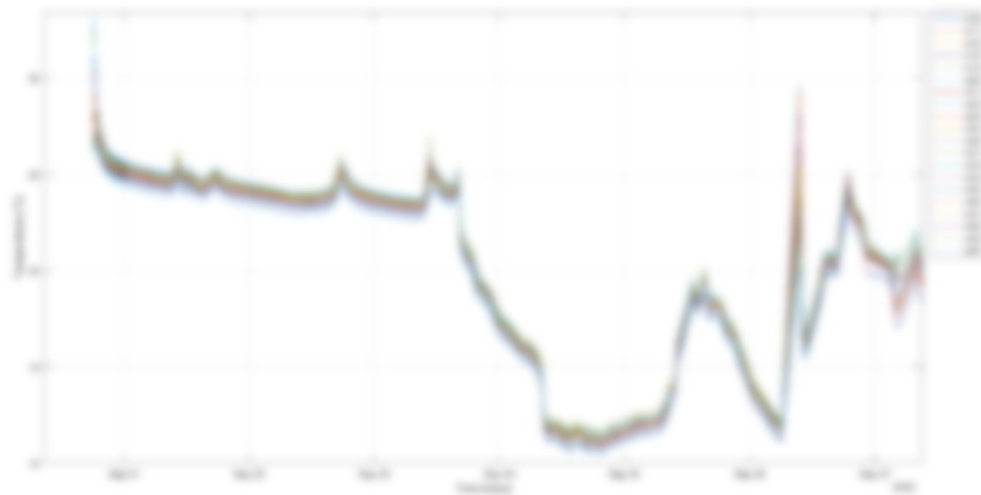


*Figure 4.18: Monitoring of pressure before the installation*

As it is possible to see from the image, the trend of the sensor's acquisitions confirms what has been discussed before. In fact, the lowering of the environmental temperature due to the rain precipitation on these days produced a lowering in temperature up to almost  $10^{\circ}$ . The lowering in temperature affects only the two days previously mentioned. After those it is possible to see a peak in temperature due to the movement of the rebars outside. This can be evinced from the abrupt peak, that is in common with the pressure, in the morning of the 26<sup>th</sup> of September and after this because of the more oscillating behaviour of the data.

The installation has been operated in the midday of the 27<sup>th</sup> of September. Here below it is reported the diagram of the acquisitions made in the construction site.

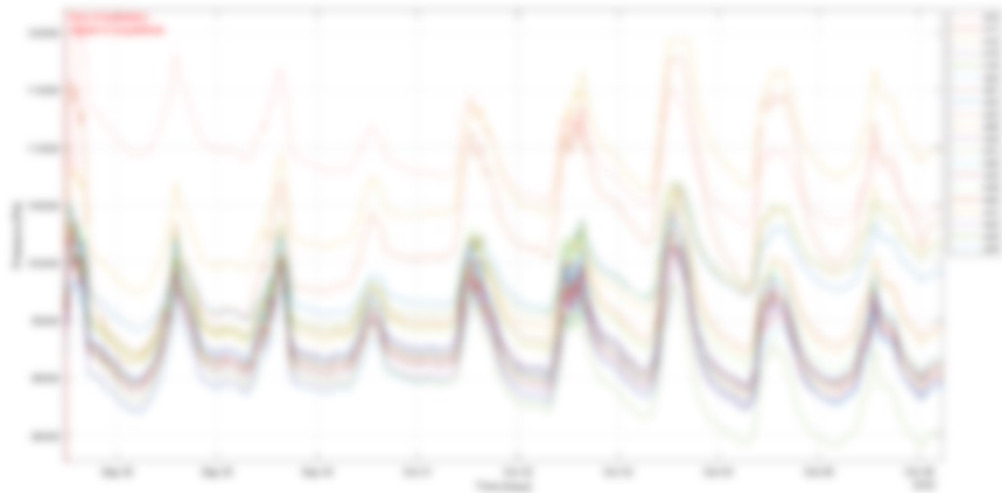


Figure 4.19: Monitoring of pressure after the installation in the construction site

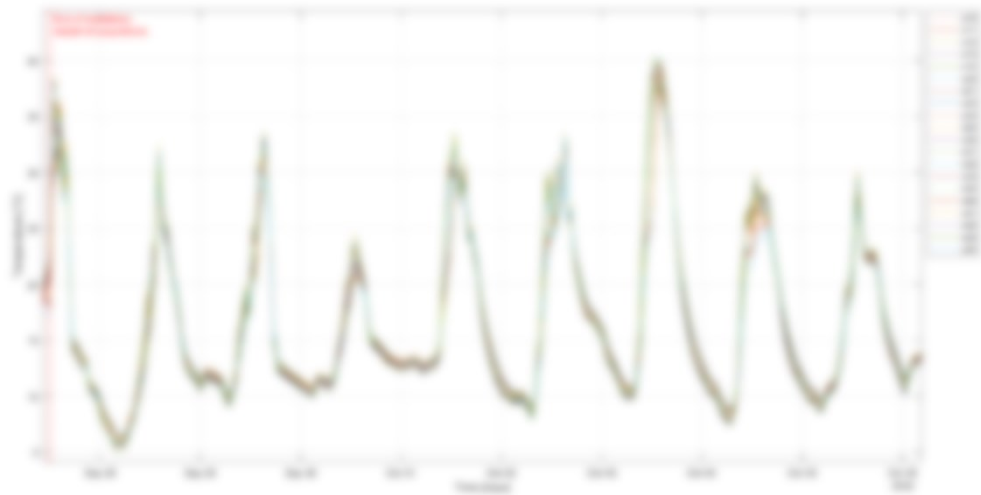


Figure 4.20: Monitoring of temperature after the installation in the construction site

The trend that is highlighted by the two diagram above represents the analogy in behaviour of the sensor in the reading of the changes in temperature and pressure. The sinusoidal progress during the days shows how pressure inside the cavity follows the path of the temperature decreasing during the nights and having a peak after midday. It is possible to highlight that the lowest temperature each day corresponds to the first hours of the morning and in particular around 4 of the morning. The trend of increasing of temperatures in the morning is almost vertical showing how the sensors' response is immediate with the changing of the environmental characteristics. On the other side, it is noticeable a difference in compactness in the pressure reading of the sensors that is not present in the temperature's readings. This is due to different conditions inside the cavity of the sensors that increase the value of pressure of the environment. Furthermore, it is possible to point out the average of the temperature during these days, that is around  $22^{\circ}\text{C}$ , highlighting that the sensors recognise properly the variation

of temperature and the trend of the season. This feature is really important and will be more visible in the following paragraph.

An important image of the work performed by the sensor can be pointed out in September the 30<sup>th</sup>. In fact, it is possible to see how both in pressure and temperature it is not possible to see the peaks that characterize the other days. This response is to attribute to the rain fell in this day that decrease the temperature of the environment.

Although it is already seen a positive trend in terms of increase of pressure for one sensor in particular which is number 12 highlighted by the yellow colour. This behaviour is to incriminate to a possible technical problem which will bring to an elimination of the sensor form the one that are valuable for the data. From these days up to the moment in which the concrete has been casted the rebars have been exposed to the environment and some of the sensor has stopped working. More evident will be the behaviour since the moment in which the concrete has been casted providing the failure of some of the specimens, hence the discarding from the acquisition of valuable data. Here below it is represented the trend of the sensors that continued to work properly since the casting.

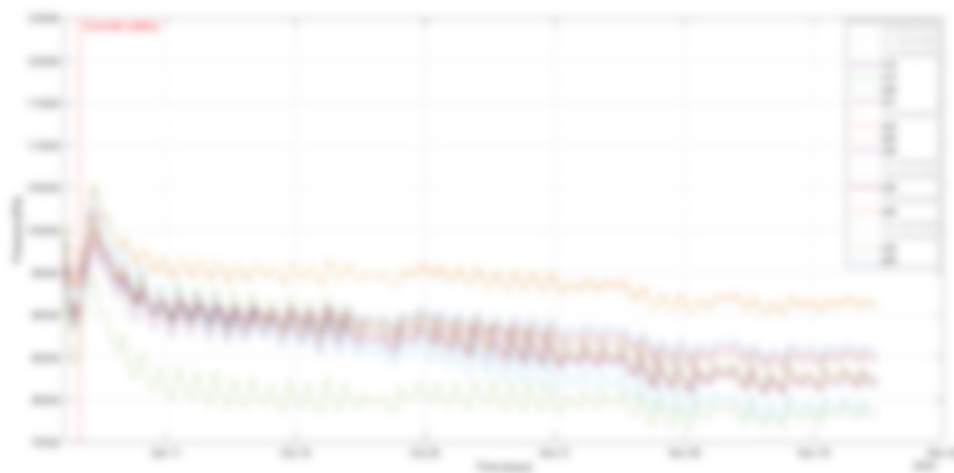


*Figure 4.21: Monitoring in pressure after the concrete casting*

From the diagram above it is important to highlight the uniform response to the casting of concrete operated on October 6<sup>th</sup>. In fact the sensor considered reacted all in the same way to the exposition to an increase of temperature of the concrete casted. It is possible to detect a strong difference between the first days of casting, going from the up to the 9<sup>th</sup> of October. During the first 3 days the heat generated by the concrete hydration brought up the pressure recorded by sensor, with the sinusoidal trend saw in the previous days that is slightly perceptible. Up to the 9<sup>th</sup> of November is almost impossible to highlight the trend of pressure that alternate the night and the days. After these early days, in the early stage of the hardening phase, the concrete conforms the characteristics to the environment and it is noticeable the change in behaviour of the sensors that have the possibility of highlighting the alteration of nights and days visible from the path of the curves. It is strongly evident how the presence of concrete generates a thermic inertia that halves the delta in pressure. At the same time it is

evident the functioning of the sensors in between October the 21<sup>st</sup> and October the 24<sup>th</sup> where the pressure is subjected to a decrease of delta from day to night. This decrease is due to a rain precipitation in the area of the installation that will generate this response in the instrumented rebars.

More important to highlight is the behaviour of the sensors when the season changes start to decrease the average pressure measured. In fact, the change in temperature as already seen before brought a decrease in the average pressure measured inside the cavity showing how the instrumented rebars are sensible to the change of environmental conditions. It is possible to imagine that this trend will continue following the monitoring with the approach of the winter and will follow a revers path with the beginning of spring. It is important to point out that the path will be subjected to modification due to the next phases of the construction of the bridge.

The behaviour described is also more evident considering the trend of temperature that shows off a more compact response as it has been described in the previous paragraphs.

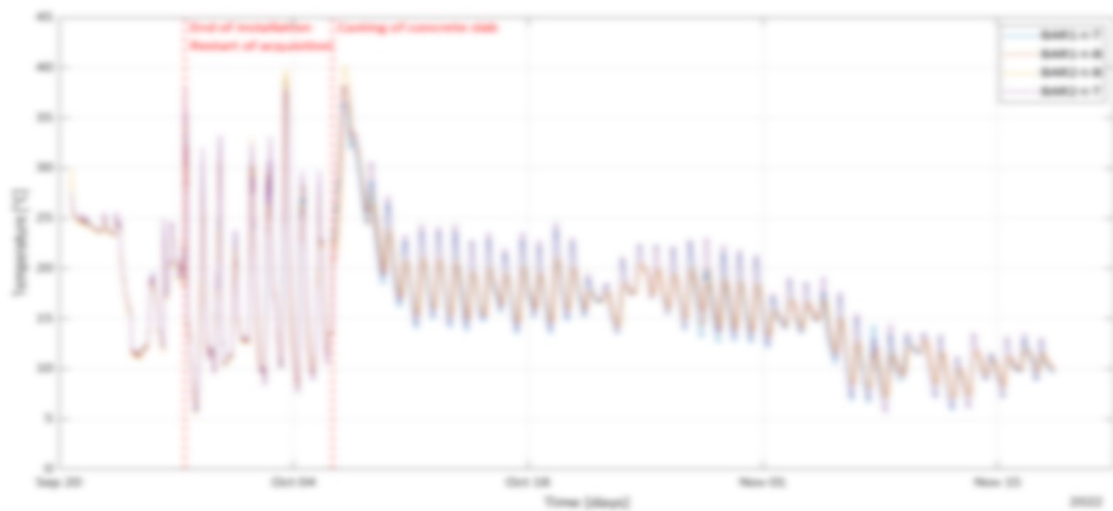


Figure 4.22: Average temperature per instrumented rebar; the final part of the name represents the position in the slab: T=Top, B=Bottom

The diagram shown above considers at the end the average of temperature of the sensors finally considered the sensors that kept working properly after the concrete casting. The position of the rebar considered has been indicated considering the longitudinal beam in which they are displaced. In fact, the position one, which represents the first longitudinal beam starting from the edge, contains the bar number 1 and number 2, respectively indicated with the letter T (Top) and B (Bottom). The same scheme has been considered with the second longitudinal beam.

From the diagram represented above it is evident how the thermic inertia halves the differences in temperature between the data collected before the concrete casting and those collected after. The diagram shows a difference of around 10°C in the first days of hardening, attenuated for the rainy days already mentioned before from the 22<sup>nd</sup> and the 24<sup>th</sup> of October. It is even more evident that the change of temperature from the beginning of November affected the temperature measured by the sensors causing a lowering of the average. This change of season is also noticed in the lowering of the

delta between the higher temperature in the morning and the lowest temperature of the nights. This trend which respects what already saw in the comment of pressure is the confirm of the proper work developed so far by the sensor displaced in the rebars.

### 4.3. Finite Element Model

The FEM model has been created on the software Robot Structural Analysis released by Autodesk. This software is load analysis software that is able to create different combinations of load according to different specifications related to the country. In this model has been possible to create the basic structure of the bridge described in the chapter 3 and apply the load related to the self-weight of the structure and various load cases of traffic load.

The generation of the model is schematized by defining first of all the axis of references of in which the main structure of the bridge will be model. The axes of references are modelled according to the drawing. In particular, the axes are defined in correspondence of the main structural frame and the transverse reinforcement. More than that it has been necessary the creation of axis of references related to the perimeter of the slab and in correspondence of the internal curb limit.

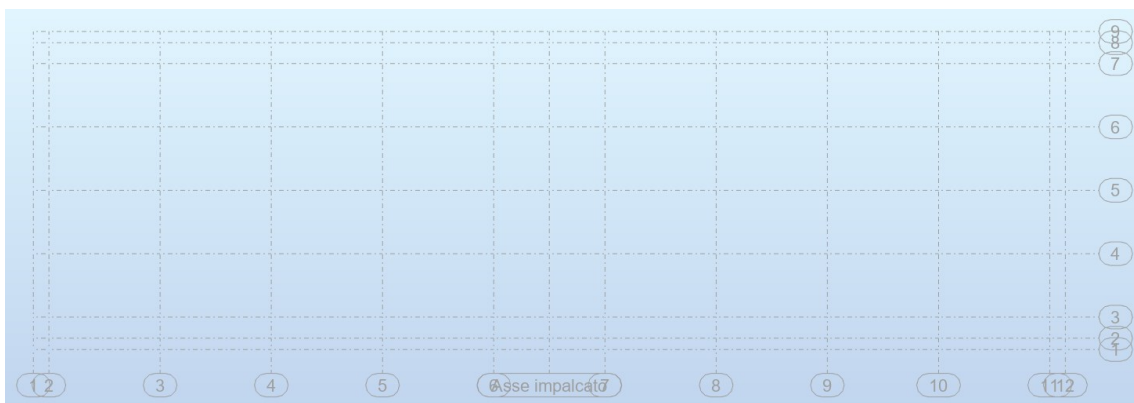


Figure 4.23 Reference axis of the deck

The next step was the definition of the geometry of the element. It is necessary to point out that the bridge has a composed material structure. In particular, the longitudinal beams and the transverse reinforcements are made in steel while the slabs are made of reinforced concrete. From the menu “Geometry”, “Property” and “Section” it is possible to create the geometry requested by the project. In particular three sections are created:

1. Longitudinal beam;
2. Transverse beam;
3. Edge transverse beam.

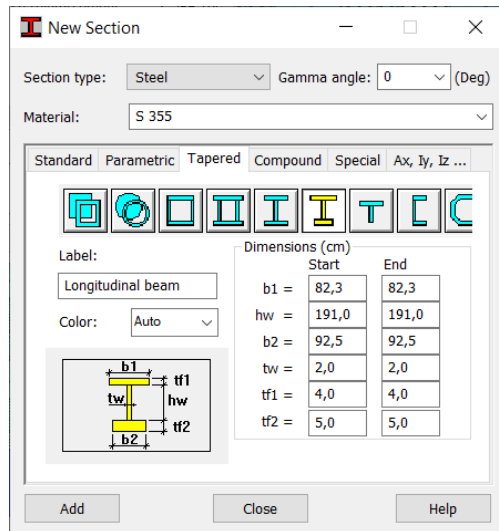


Figure 4.24 Cross section of the longitudinal beams

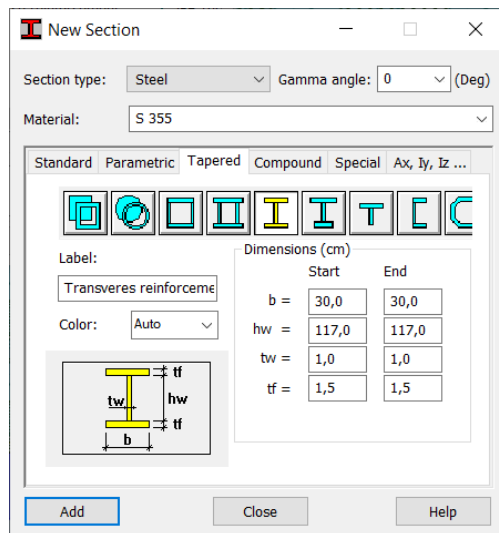


Figure 4.25 Cross section of the transverse beams

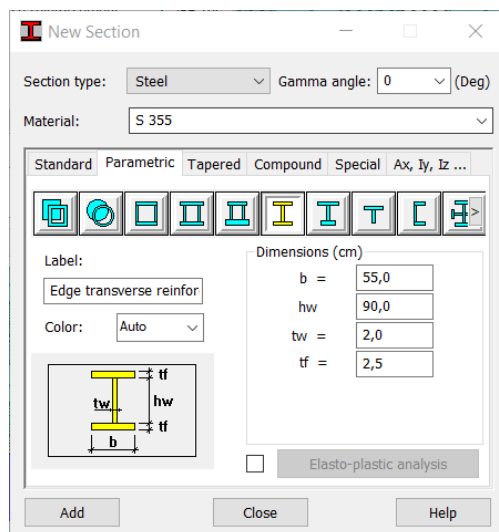


Figure 4.26: Cross section of the edge transverse beam

Once that the elements have been created it has been possible to define the position of them in the structure. The main deck has been created displaying the beam according to the structural axis defined before. The longitudinal beams have a distance of 4,02 m, while the edge transverse beam is placed at 0,7 m from the beginning of the longitudinal beam and with a distance of 5 one from the other in the other one. The result is shown down below.

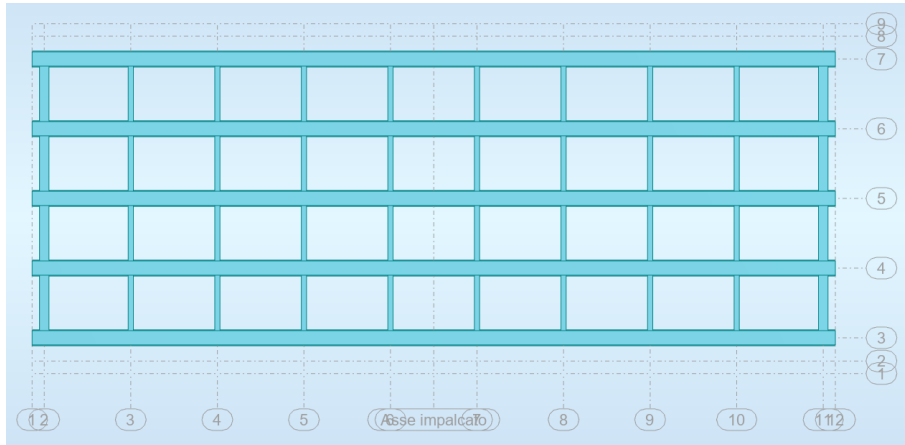


Figure 4.27 Modelling of the main structure of the bridge

The next step has been the creation of the slabs. To perform this step it has been used the features of the program that allow the design of a slab from the menu “Geometry” and “Floors”. The material selected is a concrete class C35/45, with a thickness of 30 cm, that include the reinforced concrete slab and the precast predalles, the model has been defined as a “shell”. Once that the parameters have been defined the next step is the definition of the contour. The slab has the dimensions defined by the structural axes drawn before, more specifically the floor has 20,20 m width and 46,40 m length. The structural scheme is shown below.

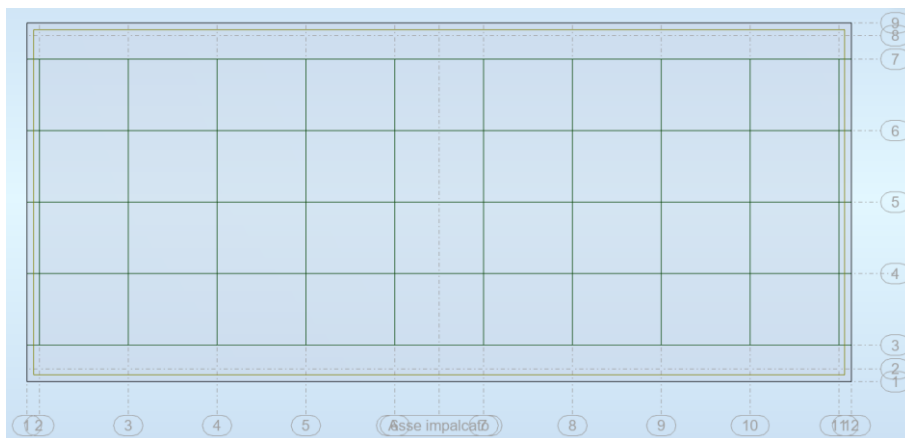


Figure 4.28: Modelling of the slab

After the definition of the structure the constrains have been determined. In particular, it has been chosen to define the structure as a simply supported beam. Hence, it has been chosen a hinge and a carriage per longitudinal beam. In this way the structure has been consider as isostatic.

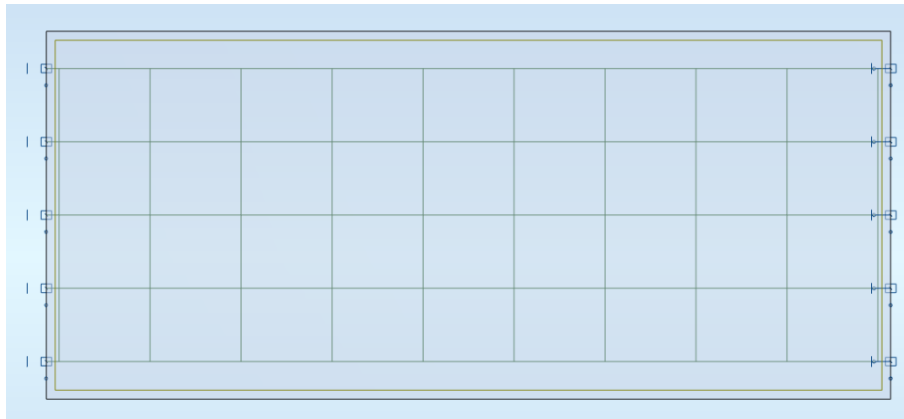


Figure 4.29: Modelling of the constraints

The structure is now defined but it is still not conformed to the real structure. In fact the slab and the beams are defined according to their barycentric axis. Hence the beams have to be shifted in the correct position. This can be done in two ways: the first procedure, the one which is adopted for the model designed, consists in the definition of an offset to apply at the longitudinal and transversal beam. This can be done from the menu “geometry”, “additional attributes” and “Offset”. In this case the beams have been moved along the z axis by a quantity which is equal to the distance between the two centroids of the two elements. This distance is equal to 1,26 cm. The second procedure can be carried out by define the two different group of elements, the slab and the beams, at the correct distance at which they are displaced. Then from the menu “geometry”, “additional attributes” and “Rigid link” it is possible to create a rigid link between the steel beams and the slab. In this way the structure behaves as a solid continuous structure.

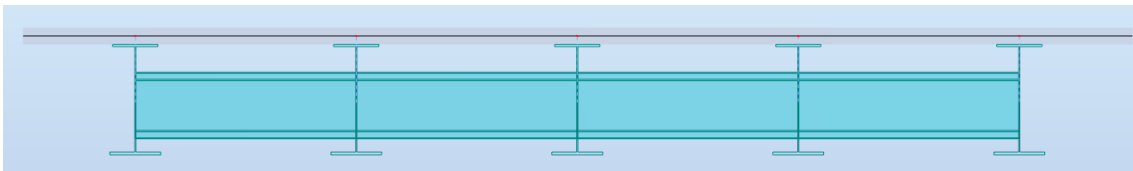


Figure 4.30: Transverse scheme of the deck

Once that the structure has been completely defined the next step is the definition and the application of the loads. First passage for this goal is the creation of the load types in from the menu “Loads” than “Load types”. Here is possible to define all the types of loads that can be applied. In particular the first two load defined has been:

1. G1: self-weight plus the reinforcement of the slab
2. G2: Pavement, curb, and barrier loads

To define this the calculation started from the definition in a computational sheet of the element geometry and density. Then it has been possible to find out the value that needed to be inserted in the model. The material used have the following characteristics.

Table 4.2 Structural material used in the calculations

Material		
Reinforced concrete		
Weight	25,0	kN/m <sup>3</sup>
Class	C35/45	-
Rck	45,0	MPa
Fck	37,4	MPa
Ecm	34625,5	MPa
Steel		
Class	S355	-
Weight	78,5	kN/m <sup>3</sup>
fyk	355,0	MPa
ftk	510,0	MPa
Es	210000,0	MPa
Reinforcement rebars		
Class	B450C	-
Density	2,0	kN/m <sup>2</sup>
Ftk	540,0	MPa
Fyk	450,0	MPa
Es	210000,0	MPa

Table 4.3: Non-structural material used in the calculation

Non-structural material		
Pavement		
Binder	1700	kg/m <sup>3</sup>
Wear layer	2400	kg/m <sup>3</sup>
Barrier		
Glass	25	kN/m <sup>3</sup>
Barrier	0,7848	kN/m

Table 4.4: Geometry of the deck

Geometry		
Slab		
Height	0,24	m
Height predalles	0,06	m
Length	46,40	m
Width	20,20	m
Span	1,00	m
Curb		
Height	0,20	m
Length	46,40	m
Width	0,72	m
Barrier		
Width	0,62	m
Length	3,00	m

Height	1,62	m
Thickness	0,01	m
Section length	3,86	m
Volume	0,12	m
Glass		
Height	2,00	m
Length	3,00	m
Depth	0,10	m
Volume	0,60	m <sup>3</sup>
Pavement		
Binder	0,09	m
Wear layer	0,05	m

The barriers considered for the calculation are MDS Segard H4b W3 with an integrated anti-noise panel in glass. The barrier is considered anchored with a distance in between the risers of 3 m. Hence, the punctual force applied in correspondence of the riser is related to 1,5m of barrier in both directions and 1,5 m of glass in both directions.

Down below the table with the different structural load are indicated.

Table 4.5: Permanent load applied to the structure

Structural loads		
Slab		
30 cm concrete	7,50	kN/m <sup>2</sup>
Reinforcement	2,00	kN/m <sup>2</sup>
Non-structural permanent loads		
Binder	1,50	kN/m <sup>2</sup>
Wear layer	1,18	kN/m <sup>2</sup>
Curb	5,00	kN/m <sup>2</sup>
Right barrier edge	5,78	kN/m <sup>2</sup>
Left barrier edge	1,00	kN/m <sup>2</sup>

Once that the structural load has been defined the next step is the definition of the accidental load. In this scenario, the load cases defined are the traffic vehicle that run across the deck of the bridge. For a first calibration of the model it has been defined 3 cases considering a case of testing of a real bridge. In particular, it has been chosen to place in the middle of the span, positioned close to the beam where the device is installed, the following loads:

- 4 trucks, coupled in two different roadways;
- Car acting in the middle span.

Table 4.6: Static traffic load

Traffic loads		
Truck	20.00	t
Car	2.00	t

The mass of the vehicles have been converted in a force multiplying by the acceleration of gravity and then divided by the point of application of the load on the deck that correspond to the four wheels of each means of transport. Hence, the forces placed in each combination of load are the following.

$$F_{truck} = \frac{m \cdot g}{4} = \frac{20 \cdot 9.81}{4} = 49.05 \text{ kN}$$

$$F_{truck} = \frac{m \cdot g}{4} = \frac{2 \cdot 9.81}{4} = 4.91 \text{ kN}$$

The different elements considered have been combined in order to obtain the values to apply on the structure.

Table 4.7: Load applied to the model

Loads		
G1	9,50	kN/m <sup>2</sup>
G2 pavement	2,68	kN/m <sup>2</sup>
G2 curb	5,00	kN/m <sup>2</sup>
G2 punctual forces of the barrier	17,35	kN
Truck	49,05	kN
Car	4,91	kN

Before the application of the loads, another important step is the definition of the nodes in correspondence of the sensors embedded in the slabs. The 10 nodes are created in the middle span of the two beams close to the right edge of the deck. The nodes are placed in the middle of the span and two nodes for side at a distance of 25 cm each one.

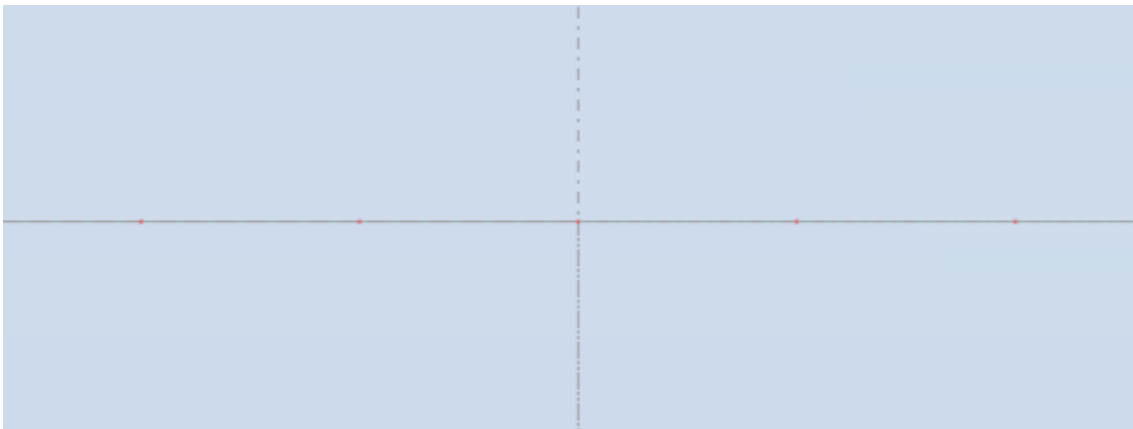


Figure 4.31: Points where the sensors are displaced

The mesh is generated at 25 cm in order to refine the texture of the results and have solid results for the extrapolation of the reaction force.

## 4.4. Application of the structural and non-structural loads

According to the values reported above it is now possible to assign the load to the structure and analyse the results and stresses that will be compared to the actual values extracted from the sensors placed in the field. The images shown below are from the left side of the building, hence it will be shown the prospect of the deck in the direction of the traffic.

### 4.4.1. Self-weight and reinforcement rebar load

The loads considered in this scheme are:

- Self-weight of the slab;
- Reinforcing rebars as a distributed load:  $2,00 \text{ kN/m}^2$ .

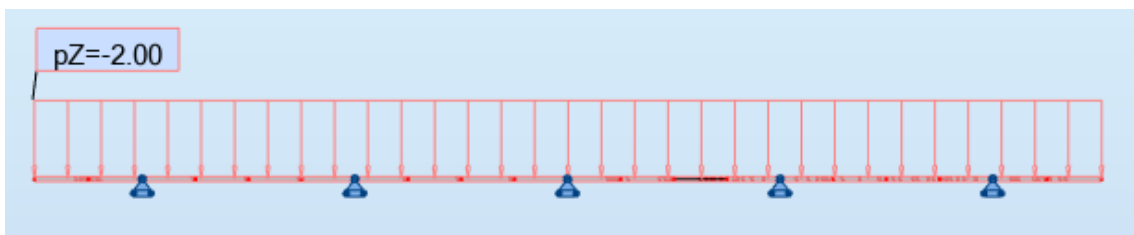


Figure 4.32: Self-weight and reinforcement

### 4.4.2. Curbs

The second element considered is the curb. This will be composed by two elements, one per side of the deck. The loads are:

- Curb:  $5,00 \text{ kN/m}^2$ .



Figure 4.33: Right curb

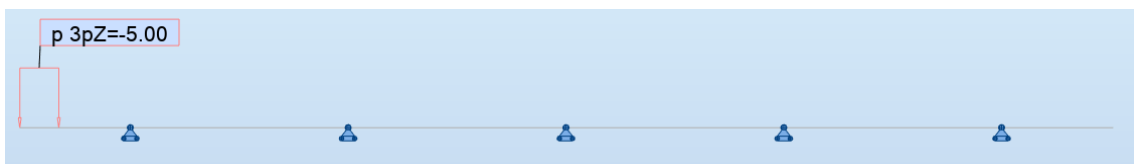


Figure 4.34: Left curb

#### 4.4.3. Barriers

This is the first asymmetric load, that is due to the two different barriers:

- Right edge of the bridge, integrate barrier with FOA:  $5,78 \text{ kN/m}^2$ ;
- Left edge of the bridge, simple barrier:  $1,00 \text{ kN/m}^2$ .



Figure 4.35: Right barrier



Figure 4.36: Left barrier

#### 4.4.4. Binder

This layer is the base of the pavement displaced on the deck of the bridge. The value is:

- Binder:  $1,50 \text{ kN/m}^2$ .

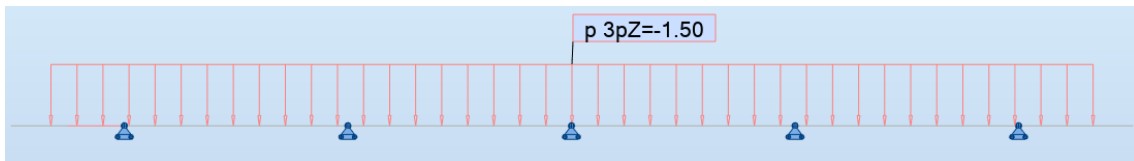


Figure 4.37: Binder

#### 4.4.5. Wearing layer

The top layer of the pavement is bitumen and the load considered is:

- Wearing layer:  $1,18 \text{ kN/m}^2$ .

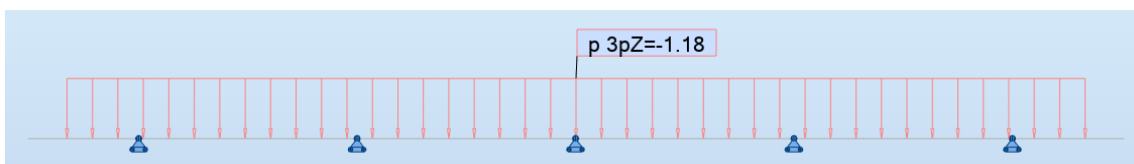


Figure 4.38: Wear layer

## 4.5.Short and long term effects

The first loads that are read by the sensor displaced in the rebars are the shrinkage of the concrete that will start after the concrete casting. The goal of the task is the calculation of the stresses that belongs to the deformation effects do to drying of the concrete.

The calculation of this effects is performed following the Eurocode [23], in particular the section 3.1.4 and the appendix B concerning the deformation due to the viscosity and the shrinkage. The performance of this analysis has been done considering the following section.

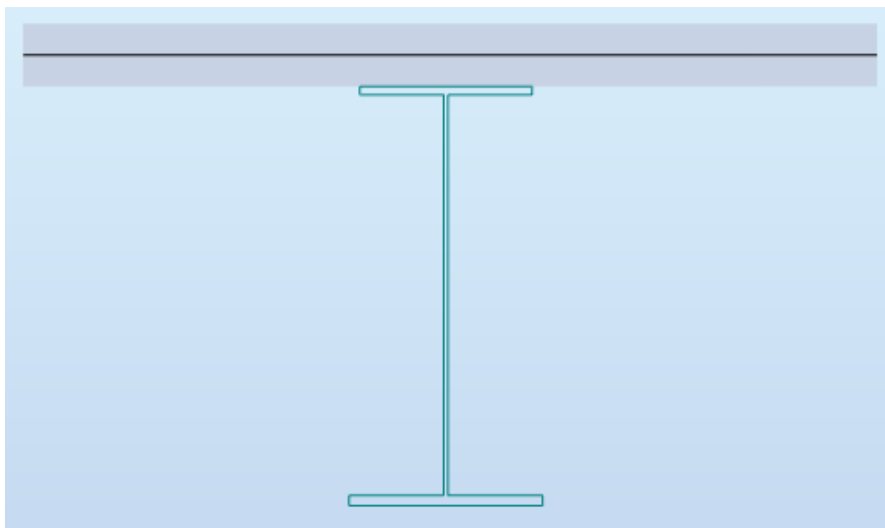


Figure 4.39: Cross section considered for the calculation of the loads

The cross section considered include the effective base width that interest the beams considered. In particular, the devices have been displayed into the first and second beam from the right edge of the beam. The calculation has been provided by considering the first cross section with an effective width that goes from the edge of the deck to the middle of the span between the longitudinal beams. The second effective width is slightly less and considers the distance between the two middle points of the spans that involves the second beam. In the model the first beam is indicated as beam 23, the second is called beam 64. The calculation is shown below.

$$A_{C1} = b_{eff1} \cdot h_c = 4,08 \cdot 0,30 = 1,22 \text{ m}^2$$

$$A_{C2} = b_{eff2} \cdot h_c = 4,04 \cdot 0,30 = 1,21 \text{ m}^2$$

The perimeter exposed to the drying of the concrete has been considered the upper surface. Hence, it has been considered  $u = 4,08 \text{ m}$ . With this data it has been possible to calculate the notional size of the member  $h_0$  which need to be expressed in mm

$$h_{0,1} = \frac{A_{C1}}{u} = \frac{1,22}{4,08} = 0,600 \text{ m} = 600 \text{ mm}$$

$$h_{0,2} = \frac{A_{c2}}{u} = \frac{1,21}{4,04} = 0,600 \text{ m} = 600 \text{ mm}$$

The relative humidity considered for the environmental conditions is  $RH = 80\%$ .

According to the Table 3.3 of the Eurocode 2 [23] is possible the definition of the coefficient that is related to the notional size of the element.

$h_0$	$k_h$
100	1.0
200	0.85
300	0.75
$\geq 500$	0.70

Figure 4.40: Definition of the coefficient  $k_h$

Finally, the initials values that are necessary for the calculation of the creep and shrinkage coefficients, considering the  $f_{cm} = f_{cm} + 8 = 45,4 \text{ MPa}$ , are:

Table 4.8 Long and short term effects

Long and short term effects		
Initial Values		
RH	80	%
u	4,080	m
$A_c$	1,224	$\text{m}^2$
$h_0$	0,600	m
$k_h$	0,7	-
$f_{cm}$	45,4	MPa

The following step is the determination of the creep and shrinkage coefficient necessary to calculate the forces that these phenomena imply in the concrete. By considering the EC2 [23], it has been calculated all the parameters that allows this result.

It has been started with the calculation of the coefficients that consider the influence of the concrete strength:

$$\alpha_1 = \left[ \frac{35}{f_{cm}} \right]^{0,7} = \left[ \frac{35}{45,4} \right]^{0,7} = 0.834$$

$$\alpha_2 = \left[ \frac{35}{f_{cm}} \right]^{0,2} = \left[ \frac{35}{45,4} \right]^{0,2} = 0.949$$

$$\alpha_3 = \left[ \frac{35}{f_{cm}} \right]^{0,5} = \left[ \frac{35}{45,4} \right]^{0,5} = 0.878$$

These parameters need to be used for the calculation of two coefficients: the factor that takes into account the relative humidity of the environment and the coefficient that depends on the relative humidity and the notional member size.

The first one, for  $f_{cm} > 35MPa$ , is calculated as follows.

$$\varphi_{RH} = \left[ 1 + \frac{1 - \frac{RH}{100}}{0,1 \cdot \sqrt[3]{h_0}} \cdot \alpha_1 \right] \cdot \alpha_2 = \left[ 1 + \frac{1 - \frac{80}{100}}{0,1 \cdot \sqrt[3]{600}} \cdot 0.834 \right] \cdot 0.949 = 1.137$$

The second one, for  $f_{cm} > 35MPa$ , is calculated as follows.

$$\beta_H = 1.5 \cdot [1 + (0.012 \cdot RH)^{18}] \cdot h_0 + 250 \cdot \alpha_3 \leq 1500 \cdot \alpha_3$$

$$\beta_H = 1.5 \cdot [1 + (0.012 \cdot 80)^{18}] \cdot 600 + 250 \cdot 0.878 = 1551.149 > 1500 \cdot \alpha_3$$

$$= 1317.035$$

Hence,  $\beta_H = 1317.035$ .

The notional creep coefficient is calculated considering three parameters that takes into account the relative humidity, the concrete strength and the age of the concrete at which the effect is measured. The formula from the Eurocode [23] is:

$$\varphi_0 = \varphi_{RH} \cdot \beta(f_{cm}) \cdot \beta(t_0)$$

The factor  $\varphi_{RH}$  has been already calculated above. The next step is the calculation of the factor concerning the concrete strength at the notional creep coefficient. This is calculated as follows.

$$\beta(f_{cm}) = \frac{16.8}{\sqrt{f_{cm}}} = \frac{16.8}{\sqrt{45.4}} = 2.493$$

The last parameter to calculate is the  $\beta(t_0)$  is the coefficient that takes into account the age of concrete at loading time  $t_0$ . To calculate this element it as been necessary an intermediate step. First of all it has been considered another parameter  $t_t$  which takes into account of the effect of the temperature in the maturity of concrete. The equation is shown below:

$$t_t = \sum_{i=1}^n e^{-\left[\frac{4000}{(273+T(\Delta t_i))}\right]^{-13.65}} \cdot \Delta t_i$$

Where:

- $\Delta t_i$  period of time in days where it is recorded a temperature T
- $T(\Delta t_i)$  temperature T during the  $\Delta t_i$

The values of  $T(\Delta t_i)$  has been chosen as the average between the minimum and the maximum temperature during the autumn season. Thus, it has been considered  $15^\circ$ . The interval of time it has been considered as one day, hence it is the day at which the shrinkage load has been applied. Considering these two values and only one interval the values of  $t_t$  is:

$$t_t = 0.788$$

Although, the  $t_t$  is set to increase according to the time considered during the different phases of the stage, hence it is considered the value referred to the first day of application.

Following this value it has been possible to obtain the value of  $t_0$ . This depends on the type of cement. In particular, it can be:

- Class S, which correspond to a coefficient  $\alpha = -1$
- Class N, which correspond to a coefficient  $\alpha = 0$
- Class R, which correspond to a coefficient  $\alpha = 1$

For simplifying the calculation it has been considered a cement type N, hence with the  $\alpha = 0$ . The formula to calculate  $t_0$  is shown below.

$$t_0 = t_t \cdot \left( \frac{9}{2 + t_t} \right)^\alpha \geq 0.5 = 0.788 \cdot \left( \frac{9}{2 + 0.788} \right)^0 = 0.778 > 0.5$$

Once that these two values have been calculated it is possible the evaluation of  $\beta(t_0)$ .

$$\beta(t_0) = \frac{1}{(0.1 + t_0^{0.20})} = \frac{1}{(0.1 + 0.788^{0.20})} = 0.949$$

Hence it has been possible to calculate the final value of the notional creep coefficient as the formula above.

$$\varphi_0 = 1.137 \cdot 2.493 \cdot 0.949 = 2.691$$

The creep coefficient is considered according to how much time has passed since the application of the load. The coefficient takes into account the time passed since the load application and the curing time of the element. These values vary from 0 at the initial time up to 1 at infinite time. Hence, at infinite time the creep coefficient is:

$$\varphi(\infty, t_0) = 2,691$$

The resume of the creep values calculated are shown in the table below.

Table 4.9: Creep values

Creep		
$\alpha_1$	0,834	-
$\alpha_2$	0,949	-
$\alpha_3$	0,878	-
$\varphi_{RH}$	1,137	-
$\beta(\text{fcm})$	2,493	-
$t_t$	0,788	d
$t_0$	0,788	d
$\beta(t_0)$	0,949	-
$\varphi_0$	2,691	-
$\varphi(\infty, t_0)$	2,691	-

The second phenomena considered is the shrinkage. Taking in consideration the Eurocode [23] and in particular the appendix B2 and the paragraph 3.1.4. The shrinkage strain is composed by two parts:

- $\varepsilon_{ds}$ , drying strain shrinkage and autogenous strain shrinkage that develops slowly in time and it is due to the tendence of the water to move through the grains of concrete already hardened;
- $\varepsilon_{as}$ , autogenous strain shrinkage, that develops in the first days of hardening of concrete and is responsible for the early drying of the material.

Hence, the total shrinkage is:

$$\varepsilon_s = \varepsilon_{ds} + \varepsilon_{as}$$

The drying shrinkage depends on the constrain that the hardened concrete has and it is due to the motion of the water in the dried matrix of concrete. The basic drying shrinkage strain is calculated starting from the consideration of two coefficients that are related to the class of concrete. As it has been mentioned before the class considered is the  $N$ , hence these two vales are:

$$\alpha_{ds1} = 4$$

$$\alpha_{ds2} = 0.12$$

The value of the  $\varepsilon_{cd,0}$  is calculated as:

$$\varepsilon_{cd,0} = 0.85 \left[ (220 + 110 \cdot \alpha_{ds1}) \cdot \exp\left(-\alpha_{ds2} \cdot \frac{f_{cm}}{f_{cm0}}\right) \right] \cdot 10^{-6} \cdot \beta_{RH}$$

Where:

- $f_{cm0} = 10MPa$
- $\beta_{RH} = 1.55 \left[ 1 - \left(\frac{RH}{RH_0}\right)^3 \right] = 1.55 \left[ 1 - \left(\frac{80}{100}\right)^3 \right] = 0.756$

Hence,

$$\varepsilon_{cd,0} = 0.85 \left[ (220 + 110 \cdot 4) \cdot \exp\left(-0.12 \cdot \frac{45.4}{10}\right) \right] \cdot 10^{-6} \cdot 0.756 = 2.461 \cdot 10^{-4}$$

The strain due to the drying shrinkage of the material are calculated as:

$$\varepsilon_{cd}(t) = \beta_{ds}(t, t_s) \cdot k_h \cdot \varepsilon_{cd,0}$$

$\beta_{ds}(t, t_s)$  depends on the time at which it is calculated. It is calculated as:

$$\beta_{ds}(t, t_s) = \frac{(t - t_s)}{(t - t_s) + 0.04 \cdot \sqrt{h_0^3}}$$

The assumption the value of  $t_s$  (time of concrete at the beginning of the drying shrinkage) depends on the time at which the concrete develops the full strength due to the hydration. Hence, the begin of the drying shrinkage has been considered after 28

days of the casting of the concrete. Starting from this day  $t_s$  is considered equal to 1. In this specific case, considering the shrinkage at infinite time the coefficient  $\beta_{ds}(t, t_s)$  is considered equal to 1. Hence the drying shrinkage will be:

$$\varepsilon_{ca}(t) = k_h \cdot \varepsilon_{cd,0} = 0.7 \cdot 2.461 \cdot 10^{-4} = 1.723 \cdot 10^{-4}$$

The autogenous shrinkage is calculated as:

$$\varepsilon_{ca}(t) = \beta_{as}(t) \cdot \varepsilon_{ca}(\infty)$$

Where,

- $\beta_{as}(t) = 1 - e^{(-0.2 \cdot t^{0.5})}$  depends on the time considered;
- $\varepsilon_{ca}(\infty)$  depends on the concrete strength and its value is:

$$\varepsilon_{ca}(\infty) = 2.5 \cdot (f_{ck} - 10) \cdot 10^{-6} = 2.5 \cdot (37.4 - 10) \cdot 10^{-6} = 6.84 \cdot 10^{-5}$$

The value of the strain due to shrinkage at infinite time is:

$$\varepsilon_s = \varepsilon_{ds} + \varepsilon_{as} = 1.723 \cdot 10^{-4} + 6.84 \cdot 10^{-5} = 2.406 \cdot 10^{-4}$$

The resume of the calculation for the determination of the shrinkage strain is shown in the table below.

Table 4.10: Shrinkage values

Shrinkage		
$\alpha_{ds1}$	4	-
$\alpha_{ds2}$	0,12	-
$\beta_{RH}$	0,756	-
$\varepsilon_{cd,0}$	2,461E-04	-
$\varepsilon_{ca,0}$	6,84E-05	-
$\varepsilon_{cs}(\infty)$	2,406E-04	-

The same procedure it has been carried out for the beam number 64 which has a concrete transverse area slightly smaller than the beam 23. The difference in area do not affect the further calculation with noticeable changes, thus it has been chosen to consider the same values for both the beam.

#### 4.6. Geometrical characteristics

Once that the loads on the structure have been applied, the stresses acting on the cross-section have been evaluated. The stresses have been calculated, considering the various construction phases of the bridges during these months and how they will affect the deformation that the S3 devices displayed in the rebar.

For the evaluation of the stresses the geometrical parameters have been considered in order to obtain the barycentric position of the composite concrete-steel section and obtain the geometry characteristics that will be used for the calculation.

The first step of calculation is the determination of the total area. Since the cross section have been composed by two different material the material should be homogenized. For the steel cross section is equal for both the beams considered in the calculation:

$$A_s = \sum_{i=1}^3 a_i = 0.117 \text{ m}^2$$

Where  $a_i$  represents the areas of each simple rectangle composing the “double T” cross section. The concrete areas have been already calculated before and are:

$$A_{C1} = b_{eff1} \cdot h_c = 4,08 \cdot 0,30 = 1,224 \text{ m}^2$$

$$A_{C2} = b_{eff2} \cdot h_c = 4,04 \cdot 0,30 = 1,212 \text{ m}^2$$

To calculate the total area of the cross section it has been chose to homogenize the section according to the concrete. For this reason the homogeneous coefficient has been calculated as follows.

$$n = \frac{E_s}{E_{cm}} = \frac{210000}{34625.5} = 6.065$$

The total area of the element will be:

$$A_{TOT1} = A_{C1} + n \cdot A_s = 1.224 + 6.025 \cdot 0.117 = 1.936 \text{ m}^2$$

$$A_{TOT2} = A_{C2} + n \cdot A_s = 1.212 + 6.025 \cdot 0.117 = 1.924 \text{ m}^2$$

To proceed in the calculation of the geometric center it is necessary the calculation of the static moment of the two elements composing the cross section. To do this it has been determined the reference line, considered as the top of the cross-section, and the two static moments have been calculated with respect to this axis. To perform this analysis the centroid of the steel section has been defined following the theory of homogeneous cross section and results with respect of the upper surface of the entire cross section as:

$$x_s = 1.408 \text{ m}$$

The next step consists in the evaluation of the static moment of the whole composed cross section. To obtain this value the area of the two distinct cross sections have been multiplied by the distance from the axis that correspond to the upper surface of the concrete slab. This iteration gives the following results.

$$S_{c1} = A_{C1} \cdot \frac{d_t}{2} = 1.224 \cdot \frac{0.3}{2} = 0.184 \text{ m}^3$$

$$S_{c2} = A_{C2} \cdot \frac{d_t}{2} = 1.212 \cdot \frac{0.3}{2} = 0.182 \text{ m}^3$$

$$S_s = A_s \cdot x_s = 0.117 \cdot 1.408 = 0.165 \text{ m}^3$$

The static moment of the entire cross section is calculated homogenising the area with respect to the concrete.

$$S_1 = S_{c1} + n \cdot S_s = 0.184 + 6.065 \cdot 0.165 = 1.186 \text{ m}^3$$

$$S_2 = S_{c2} + n \cdot S_s = 0.182 + 6.065 \cdot 0.165 = 1.184 \text{ m}^3$$

The barycentre of the two sections is obtained from the following formula.

$$x_{g1} = \frac{S_1}{A_1} = \frac{1.186}{1.936} = 1.688$$

$$x_{g2} = \frac{S_2}{A_2} = \frac{1.186}{1.936} = 1.685$$

The same procedure has been applied for the calculation of the inertia modulus, for steel concrete and then summed together homogenising the section with respect to the concrete.

$$I_a = \sum_{i=1}^3 \frac{b_i \cdot h_i^3}{12} + a_i \cdot d_i^2$$

Where:

- $b_i$  is the base of each simple cross section that compose the double T steel cross section;
- $h_i$  is the height of each simple cross section that compose the double T steel cross section;
- $a_i$  is the area of each simple cross section that compose the double T steel cross section;
- $d_i$  is the distance from the barycentre of each simple cross section that compose the double T steel cross section and the barycentre of entire cross section;

The value of the moment of inertia for steel cross section is:

$$I_a = 0.086 \text{ m}^3$$

The moment of inertia of the concrete is:

$$I_{c1} = \frac{b_1 \cdot h^3}{12} = \frac{4.08 \cdot 0.30^3}{12} = 0.00918 \text{ m}^4$$

$$I_{c2} = \frac{b_2 \cdot h^3}{12} = \frac{4.04 \cdot 0.30^3}{12} = 0.00909 \text{ m}^4$$

The total modulus of inertia homogenized with respect to the concrete is:

$$I_1 = I_{c1} + n \cdot I_s + n \cdot A_s \cdot (x_s - x_g)^2 + A_c \cdot (x_c - x_g)^2 = 1.244 \text{ m}^4$$

$$I_1 = I_{c1} + n \cdot I_s + n \cdot A_s \cdot (x_s - x_g)^2 + A_c \cdot (x_c - x_g)^2 = 1.212 \text{ m}^4$$

## 4.7. Analysis of the results from the model

Basing the calculation on these values obtained through the geometrical analysis of the structure it has been performed the analysis on Robot Structural Analysis. In this way it has been extracted all the reaction force from the different load cases and then converted to stress and deformation with a computational sheet. In order to proceed with this evaluation it has been necessary to test the model and compare it with the actual deformation that are calculated from the theory

### 4.7.1. Evaluation of the model

To extrapolate the expected strain that will be read in the instrumented rebars the model has been tested to understand the response in terms of stiffness. To obtain this results a second model has been defined that respects the same geometrical characteristics of the cross section of the beam and of the slab but refer to one single element of the deck of the bridge. In particular, considering the parameters that are given by the calculation above. The cross section of the calculation's scheme is reported below.

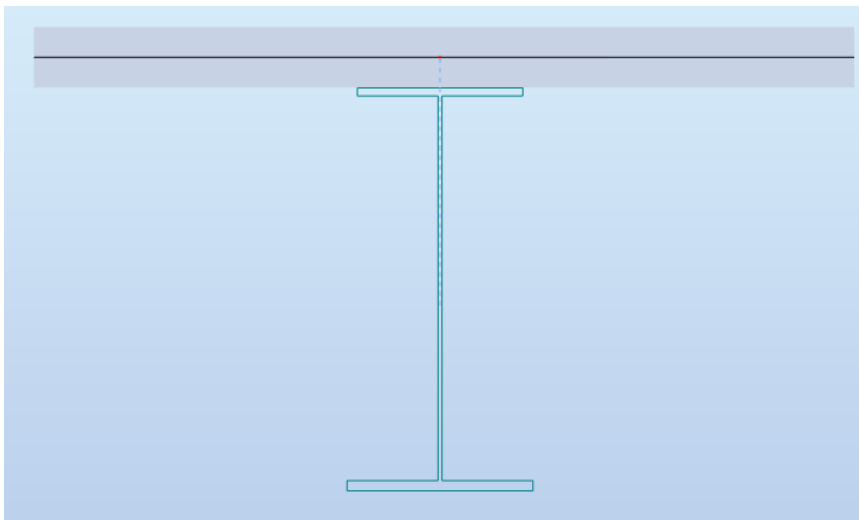


Figure 4.41: Cross-section of the single beam

The section has been modelled by defining the cross section of the beam according to the reference line already tracked. In order to build a truthful model in terms of stiffness it has been applied an offset to the longitudinal beam. Then the slab has been modelled above the beam as a bi-dimensional element with a thickness of 30 cm. The slab has been considered as a rigid diaphragm in order to take into account of the realistic deformation of the element.

The first analysis of the element has been considered with the self-weight of the slab. In particular the slab is composed of two materials: concrete class C35/45 and the reinforcement rebars in steel. The software automatically assigns self-weight of the concrete as it has been defined in the previous paragraph, thus  $24 \frac{kg}{m^3}$ . To take into account the weight of the reinforcement it has been considered the first load-case

defined above, hence a distributed load of  $2 \frac{kN}{m^2}$ . The analysis brought the following deformation.

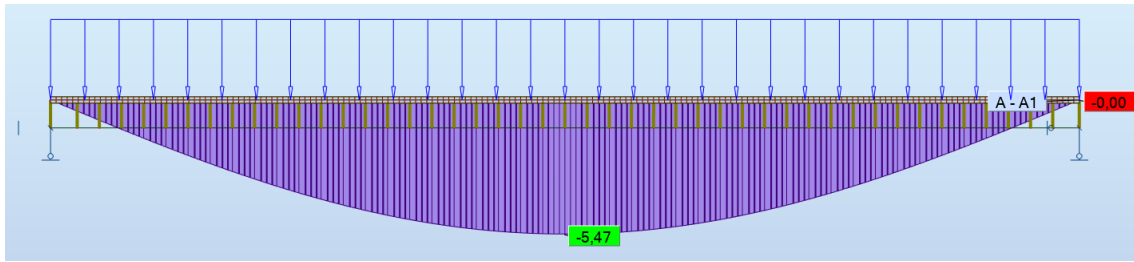


Figure 4.42: Deformation in correspondence of the beam

According to the calculations the displacement calculated in the middle of the span has been obtained as follows. The load considers is  $7,50 \frac{kN}{m^2}$  for the concrete and  $2 \frac{kN}{m^2}$  for the reinforcement. The deflection in the middle of the span is:

$$\delta = \frac{5}{384} \cdot \frac{ql^4}{E_c I_0}$$

Where:

- $l$  is the span length, equal to  $46,4 m$ ;
- $q$  is the summation of the two loads multiplied by the width of influence which corresponds to  $4,08 m$ ;
- $E_c$  is the Young modulus of the concrete used for the homogenization of the cross section with respect to this material;
- $I_0$  is the modulus of inertia of the element homogenized with respect to the concrete;

$$\delta = \frac{5}{384} \cdot \frac{ql^4}{E_c I_0} = \frac{5}{384} \cdot \frac{(7.5 + 2) \cdot 4.08 \cdot 46.4^4}{34625.5 \cdot 1.244} = 5.44 \text{ cm}$$

Comparing this with the previous results obtained from the model it is possible to affirm that the model works, hence it is possible to proceed with the analysis.

#### 4.8. Determination of the solicitation and stresses

The elaboration of the model has the goal of determination of the stresses and the strains determined for each phase of the construction of the bridge. The phases elaborated considers the sequence of the different elements that are already completed and that will be built towards the completion of the bridge. As it will be show in the chapter 4.9 it has been registered the completion of the slab of the bridge, which is subjected to the phenomena of shrinkage and creep generated by the shrinkage.

At the moment the load cases studied from the load-cases studied and showed above only two of them have already been completed, hence it is possible to compare the calculation with the data collected by the instrumented rebar in the field. The load-cases involved so far with the collection of the data are:

- Self-weight of the slab and reinforcement rebars;
- Long term effect caused by shrinkage and creep;

Hence, it will be evaluated the strain induced by the solicitations above and according to the geometry and the load will be gave a measure of the expected stress and strain that is possible to highlight from the different construction phases. From the menu “Results” and “Forces”, for each load-case it has been considered the moment agent on the beam number 23 and number 64. It has been considered each single load and then the sum of the load with the previous stages of construction already completed.

#### 4.8.1. Self-weight and reinforcement

From the model it has been extrapolated the following solicitations. The solicitations concern the longitudinal beam number one and number 2, respectively in the model number 23 and 64.

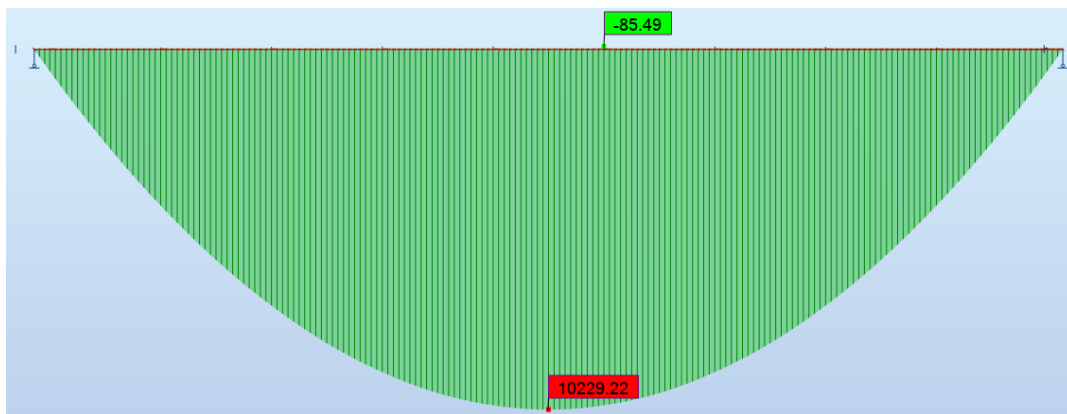


Figure 4.43: Diagram of moment [kNm] expected with self-weight of the slab and the reinforcement displaced

The table considering the different values read in correspondence of the five points in which the sensors are displaced is reported below.

Table 4.11: Table of the first load-case

Moment values [kNm]		Axis position (m)				
		22,7	22,95	23,2	23,45	23,7
Beam number	23	10224,35	10228,01	10229,20	10227,92	10224,17
	64	10109,40	10112,60	10113,63	10112,49	10109,18

Since the application of the load, hence since the casting of the concrete, the rebars which are object of study will not be affected by the load. In the early stages, the first hour after the casting of the concrete, the concrete is still fluid, hence the sensors will read the hydration heat of the concrete that will be discussed in the following chapter. The first solicitations that will be read by the rebars are the effects of the shrinkage which is object of study of the next load-case.

It is interesting to see the tension generated by the cast of the concrete in the longitudinal beam in order to have an idea of the stresses that are developed at the

interface between the slab and the beam. Using the Navier equation it has been determined the stress in the upper part of the flange of the steel beam.

$$\sigma_{s,sup} = n \cdot \left(\frac{M}{I}\right) \cdot (2 - x_G)$$

Table 4.12: Stress expected at the interface in between the longitudinal beams and the slab

$\sigma_{s, sup}$ [MPa]		Axis position (m)				
		22,7	22,95	23,2	23,45	23,7
Beam number	23	15,57	15,58	15,58	15,58	15,57
	64	15,40	15,40	15,40	15,40	15,40

Table 4.13 Strain expected at the interface in between the longitudinal beams and the slab

$\epsilon_{s, sup}$ [ $\mu\epsilon$ ]		Axis position (m)				
		22,7	22,95	23,2	23,45	23,7
Beam number	23	74,16	74,18	74,19	74,18	74,15
	64	73,32	73,35	73,35	73,34	73,32

#### 4.8.2. Short and long term effects

The first valuable effects in which the sensors will start to work is the short terms effects related to the shrinkage of the material. The initial shrinkage is the parameters that in this sense will be considered more in terms of load applied to the element. The different parameters for what concern the shrinkage and the creep have been evaluated in the previous paragraph. Each parameter, and as a consequence the forces acting on the S3 system installed, depends on how much time passed since the casting.

Hence a first evaluation can be done when the concrete just begins to harden. At one day from the concrete casting it has been evaluated the forces acting on the structure and the table below reports the analysis.

Table 4.14: Value at one day of the casting of the concrete

t		Coefficients	Values	N	e	M
d		-	-	kN	m	kNm
1	Shrinkage parameters	$\beta_c(t, t_s)$	0,00E+00	38,26	0,49	18,85
		$\epsilon_{cd}(t)$	0,00E+00			
		$\beta_a(t, t_s)$	0,18			
		$\epsilon_{ca}(t)$	1,24E-05			
		$\epsilon_{cs}(t)$	1,24E-05			
	Creep parameters	$\beta(t, t_0)$	0,073			
		$\varphi(t, t_0)$	0,20			
		$\epsilon_{cs, tot}$	9,03E-07			

The major apport to the shrinkage coefficient is given by the autogenous shrinkage while the drying shrinkage still have a minor apport to the stress generated. The creep coefficient affects the homogenization coefficient which will gradually affect the

characteristics of the section in terms of Inertia Modulus and barycentre. In particular, the homogenization coefficient depends on the type of load considered. The calculation of the modular ratio depending on the load type. In particular:

$$n_l = n_0 \cdot (1 + \varphi_0 \varphi(t, t_0))$$

Where:

- $\varphi_0 = 1,1$  for permanent load
- $\varphi_0 = 0,5$  for shrinkage

In this case, it has been analysed the creep effects at one day from the drying of the concrete. The modular ratio it is equal to:

$$n_l = n_0 \cdot (1 + \varphi_0 \varphi(t, t_0)) = 6.065 \cdot (1 + 0.55 \cdot 0.196) = 6.719$$

Hence it has been possible to calculate:

$$N = \varepsilon_{cs} \cdot A_c \cdot E_{cm}$$

$$e = 2.15 - x_g$$

$$M = N \cdot e$$

These forces have been applied to the cross section of the composite deck of the beam and it has been possible the evaluation of the expected stress state and strain of the point in correspondence with the two instrumented rebars.

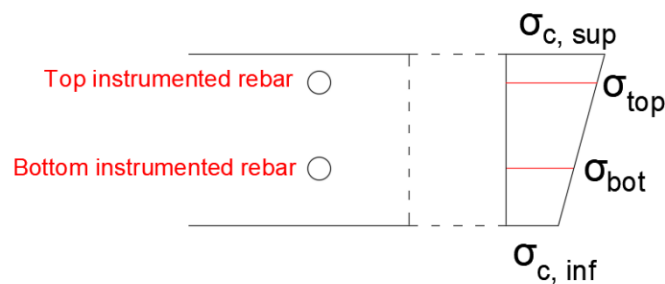


Figure 4.44: Stresses in the instrumented rebars

According to the position of the rebars it has been evaluated the stresses and strains obtained by the applications of the shrinkage and creep load.

$$\sigma_{top} = \left( -\frac{N}{A} + \frac{M \cdot (2,25 - x_g)}{I} + \frac{N}{A_c} \right) \cdot n_l$$

$$\sigma_{bot} = \left( -\frac{N}{A} + \frac{M \cdot (2,10 - x_g)}{I} + \frac{N}{A_c} \right) \cdot n_l$$

The procedure it has been repeated for both the beam giving the following results in terms of stress and strain.

Table 4.15: Stress and strain due to shrinkage at 1 day in beam 23

Beam 23		
$\sigma_{top, c}$	0,14	MPa
$\sigma_{bot, c}$	0,14	MPa
$\epsilon_c$	0,69	$\mu\epsilon$
$\epsilon_c$	0,69	$\mu\epsilon$

Table 4.16: Stress and strain due to shrinkage at 1 day in beam 64

Beam 64		
$\sigma_{top, c}$	0,27	MPa
$\sigma_{bot, c}$	0,27	MPa
$\epsilon_c$	1,34	$\mu\epsilon$
$\epsilon_c$	1,34	$\mu\epsilon$

In the beginning it is possible to notice how the only parameter that affect the stress in the rebar is the autogenous shrinkage. This is because of what described in the paragraph 4.3. Hence in the early stage, the shrinkage has a small impact in the determination of the stresses. Also, is important to notice that the small difference in geometry do not affect the value of stress obtained. This is due to the uniform application of the shrinkage considered.

The operation has been repeated at 16 days, in order to understand how the parameters has changed.

t		Coefficients	Values	N	e	M
d		-	-	kN	m	kNm
16	Shrinkage parameters	$\beta_c(t, t_s)$	0,00E+00	266,81	0,50	134,35
		$\epsilon_{cd}(t)$	0,00E+00			
		$\beta_a(t, t_s)$	0,55			
		$\epsilon_{ca}(t)$	3,77E-05			
		$\epsilon_{cs}(t)$	3,77E-05			
	Creep parameters	$\beta(t, t_0)$	0,17			
		$\varphi(t, t_0)$	0,27			
		$\epsilon_{cs, tot}$	6,30E-06			

As it has been mentioned before, the autogenous shrinkage is the only component that affect the shrinkage load in this phase. It is possible to notice a small increase of this value that generate an increase in the forces. At 16 days the straining of the concrete increase and according to the values in the tables

Table 4.17: Stress and strain due to shrinkage at 16 day in beam 23

Beam 23		
$\sigma_{top, c}$	2,09	MPa
$\sigma_{bot, c}$	2,09	MPa
$\epsilon_c$	10,47	$\mu\epsilon$
$\epsilon_c$	10,47	$\mu\epsilon$

Table 4.18: Stress and strain due to shrinkage at 16 day in beam 64

Beam 64		
$\sigma_{top, c}$	3,72	MPa
$\sigma_{bot, c}$	3,72	MPa
$\epsilon_c$	18,58	$\mu\epsilon$
$\epsilon_c$	18,58	$\mu\epsilon$

Now, according to the sensitivity of the sensors, the straining is clearly visible even if it is really small at the moment.

#### 4.8.3. Curb load-case

At complete maturation of the concrete in the slab, hence at 28 days, it has been considered the expected construction phase of the curbs. The stages are considered separately in order to understand the influence on the rebar of each curb and then summed up together in order to evaluate the complex force agent on the rebars.

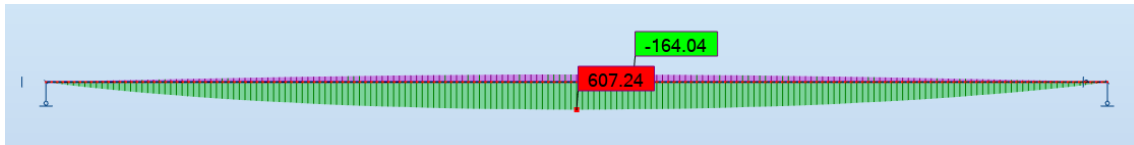


Figure 4.45: Right curb load-case



Figure 4.46: Left curb load-case

The moment generated by the right curb is:

Table 4.19 Right curb load moment

Moment values [kNm]		Axis position (m)				
		22,70	22,95	23,20	23,45	23,70
Beam number	23	606,83	607,14	607,24	607,13	606,83
	64	371,18	371,18	371,18	371,18	371,19

The moment generated for the left curb is:

Table 4.20 Left curb load moment

Moment values [kNm]		Axis position (m)				
		22,70	22,95	23,20	23,45	23,70
Beam number	23	-163,13	-163,13	-163,13	-163,13	-163,13
	64	-14,40	-14,40	-14,40	-14,40	-14,40

From the table above it is possible to see how the moment is really similar in the five points in which the sensors are displaced. For the negative load, due to the load in the left part of the deck that generate a tension in the right beams, the values are exactly the same. Hence, it is expected a state of stress and a straining of the concrete really similar.

This load is a permanent, non-structural, load agent on the structure. Hence the value of  $\varphi_0$  for the calculation of the modular ratio is 1.1. The modular ratio is:

$$n_L = 11,64$$

For the right curb once has.

Table 4.21: Stress and strain generated by the right curb on beam 23

Beam number 23					
Distance [m]	22,70	22,95	23,20	23,45	23,70
$\sigma_{top, c}$ [MPa]	5,82	5,82	5,83	5,82	5,82
$\sigma_{bot, c}$ [MPa]	5,30	5,30	5,30	5,30	5,30
$\epsilon_c$ [ $\mu\epsilon$ ]	168,18	168,22	168,23	168,22	168,18
$\epsilon_c$ [ $\mu\epsilon$ ]	153,14	153,17	153,18	153,17	153,14

Table 4.22: Stress and strain generated by the right curb on beam 64

Beam number 64					
Distance [m]	22,70	22,95	23,20	23,45	23,70
$\sigma_{top, c}$ [MPa]	7,15	7,15	7,15	7,15	7,15
$\sigma_{bot, c}$ [MPa]	6,83	6,83	6,83	6,83	6,83
$\epsilon_c$ [ $\mu\epsilon$ ]	206,58	206,58	206,58	206,58	206,58
$\epsilon_c$ [ $\mu\epsilon$ ]	197,36	197,36	197,36	197,36	197,36

For the left curb once has.

Table 4.23: Stress and strain generated by the left curb on beam 23

Beam number 23					
Distance [m]	22,70	22,95	23,20	23,45	23,70
$\sigma_{top, c}$ [MPa]	2,46	2,46	2,46	2,46	2,46
$\sigma_{bot, c}$ [MPa]	2,60	2,60	2,60	2,60	2,60
$\epsilon_c$ [ $\mu\epsilon$ ]	71,07	71,07	71,07	71,07	71,07
$\epsilon_c$ [ $\mu\epsilon$ ]	75,12	75,12	75,12	75,12	75,12

Table 4.24: Stress and strain generated by the left curb on beam 64

Beam number 64					
Distance [m]	22,70	22,95	23,20	23,45	23,70
$\sigma_{top, c}$ [MPa]	5,46	5,46	5,46	5,46	5,46
$\sigma_{bot, c}$ [MPa]	5,47	5,47	5,47	5,47	5,47
$\epsilon_c$ [ $\mu\epsilon$ ]	157,62	157,62	157,62	157,62	157,62
$\epsilon_c$ [ $\mu\epsilon$ ]	157,98	157,98	157,98	157,98	157,98

The stresses, obtained with the Navier formula, comprehend the pressure generated in the longitudinal rebar by the load considered plus the shrinkage at the time of application of the load.

As it is possible to see, the expected stresses are congruent with the load applied and generate a straining in the concrete acceptable for the evaluation carried out. In particular, comparing this strain with the potential of the sensors it is clearly possible to understand the utility of the sensor in the monitoring of the phases of the structure

#### 4.8.4. Barrier load-case

The installation of the barrier it has been considered at 64 days. The modular ratio hence will be equal to:

$$n_L = 13,18$$

The barrier load-cases are shown below.

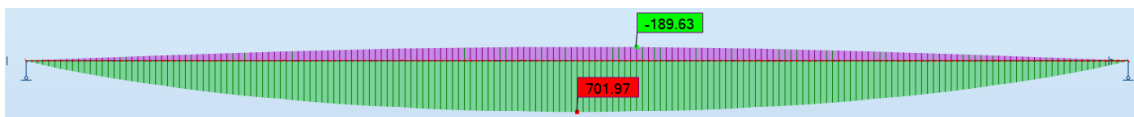


Figure 4.47: Right barrier load-case

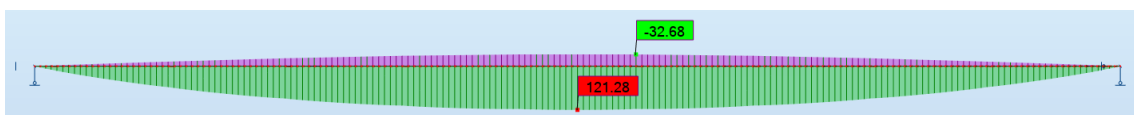


Figure 4.48: Left barrier load-case

The moment generated by the right barrier is:

Table 4.25 Right curb load moment

Moment values [kNm]		Axis position (m)				
		22,70	22,95	23,20	23,45	23,70
Beam number	23	701,50	701,85	701,97	701,85	701,49
	64	429,09	429,08	429,08	429,08	429,1

The moment generated for the left barrier is:

Table 4.26 Left curb load moment

Moment values [kNm]		Axis position (m)				
		22,70	22,95	23,20	23,45	23,70
Beam number	23	-32,63	-32,63	-32,63	-32,63	-32,63
	64	-2,88	-2,88	-2,88	-2,88	-2,88

The stresses and strain for the right barrier are shown below.

Table 4.27: Right barrier stresses and strains on beam 23

Beam number 23					
Distance [m]	22,70	22,95	23,20	23,45	23,70
$\sigma_{top, c}$ [MPa]	10,62	10,62	10,62	10,62	10,62
$\sigma_{bot, c}$ [MPa]	9,99	9,99	10,00	9,99	9,99
$\epsilon_c$ [ $\mu\epsilon$ ]	306,61	306,66	306,67	306,66	306,61
$\epsilon_c$ [ $\mu\epsilon$ ]	288,62	288,66	288,67	288,66	288,62

Table 4.28: Right barrier stresses and strains on beam 64

Beam number 64					
Distance [m]	22,70	22,95	23,20	23,45	23,70
$\sigma_{top, c}$ [MPa]	14,34	14,34	14,34	14,34	14,34
$\sigma_{bot, c}$ [MPa]	13,96	13,96	13,96	13,96	13,96
$\epsilon_c$ [ $\mu\epsilon$ ]	414,27	414,27	414,27	414,27	414,27
$\epsilon_c$ [ $\mu\epsilon$ ]	403,24	403,24	403,24	403,24	403,24

The stresses and strain for the left barrier are shown below.

Table 4.29: Left barrier stresses and strains on beam 23

Beam number 23					
Distance [m]	22,70	22,95	23,20	23,45	23,70
$\sigma_{top, c}$ [MPa]	7,13	7,13	7,13	7,13	7,13
$\sigma_{bot, c}$ [MPa]	7,16	7,16	7,16	7,16	7,16
$\epsilon_c$ [ $\mu\epsilon$ ]	205,93	205,93	205,93	205,93	205,93
$\epsilon_c$ [ $\mu\epsilon$ ]	206,77	206,77	206,77	206,77	206,77

Table 4.30: Left barrier stresses and strains on beam 64

Beam number 64					
Distance [m]	22,70	22,95	23,20	23,45	23,70
$\sigma_{top, c}$ [MPa]	12,28	12,28	12,28	12,28	12,28
$\sigma_{bot, c}$ [MPa]	12,28	12,28	12,28	12,28	12,28
$\epsilon_c$ [ $\mu\epsilon$ ]	354,65	354,65	354,65	354,65	354,65
$\epsilon_c$ [ $\mu\epsilon$ ]	354,72	354,72	354,72	354,72	354,72

Also in this case the strains are congruent with the load considered and the application of this load will generate a variability in the curve pressure-time and temperature time that have been showed in the previous paragraphs.

#### 4.8.5. Binder load-case

The laying of the binder layer it has been considered alongside the installation of the barrier so at 64 days. The modular ratio hence will be equal to:

$$n_L = 13,18$$

The binder load-cases are shown below.

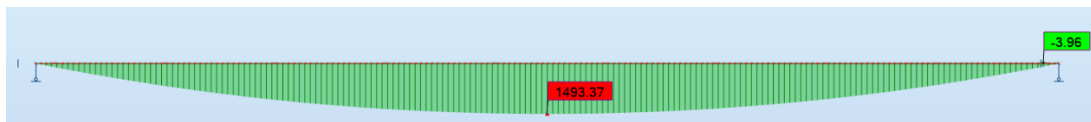


Figure 4.49: Binder load-case

The moment generated by the binder is:

Table 4.31 Binder load moment

Moment values [kNm]		Axis position (m)				
		22,70	22,95	23,20	23,45	23,70
Beam number	23	701,50	701,85	701,97	701,85	701,49
	64	429,09	429,08	429,08	429,08	429,1

The stresses and strain for the binder are shown below.

Table 4.32: Binder stresses and strains on beam 23

Beam number 23					
Distance [m]	22,70	22,95	23,20	23,45	23,70
$\sigma_{top, c}$ [MPa]	14,32	14,32	14,32	14,32	14,32
$\sigma_{bot, c}$ [MPa]	13,00	13,01	13,01	13,01	13,00
$\epsilon_c$ [ $\mu\epsilon$ ]	413,54	413,61	413,63	413,60	413,54
$\epsilon_c$ [ $\mu\epsilon$ ]	375,56	375,61	375,63	375,61	375,56

Table 4.33: Binder stresses and strains on beam 64

Beam number 64					
Distance [m]	22,70	22,95	23,20	23,45	23,70
$\sigma_{top, c}$ [MPa]	19,41	19,41	19,41	19,41	19,41
$\sigma_{bot, c}$ [MPa]	18,09	18,09	18,09	18,09	18,09
$\epsilon_c$ [ $\mu\epsilon$ ]	560,60	560,67	560,69	560,67	560,59
$\epsilon_c$ [ $\mu\epsilon$ ]	522,31	522,37	522,39	522,37	522,31

Also in this case the strains are congruent with the load considered and the application of this load will generate a variability in the curve pressure-time and temperature time that have been showed in the previous paragraphs.

#### 4.8.6. Wear layer load-case

The laying of the wear layer has been considered at 80 days. The modular ratio hence will be equal to:

$$n_L = 13,66$$

The barrier load-cases are shown below.

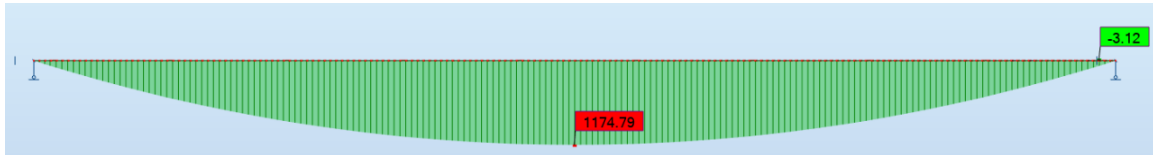


Figure 4.50: Wear layer load-case

The moment generated by the wear layer is:

Table 4.34 Wear layer load moment

Moment values [kNm]		Axis position (m)				
		22,70	22,95	23,20	23,45	23,70
Beam number	23	1165,26	1165,64	1165,76	1165,63	1165,24
	64	1171,49	1171,89	1172,02	1171,88	1171,47

The stresses and strain for the wear layer are shown below.

Table 4.35: Wear layer stresses and strains on beam 23

Beam number 23					
Distance [m]	22,70	22,95	23,20	23,45	23,70
$\sigma_{top,c}$ [MPa]	14,39	14,39	14,39	14,39	14,39
$\sigma_{bot,c}$ [MPa]	13,35	13,35	13,35	13,35	13,35
$\epsilon_c$ [ $\mu\epsilon$ ]	415,58	415,64	415,66	415,64	415,58
$\epsilon_c$ [ $\mu\epsilon$ ]	385,41	385,46	385,47	385,46	385,41

Table 4.36: Wear layer stresses and strains on beam 64

Beam number 64					
Distance [m]	22,70	22,95	23,20	23,45	23,70
$\sigma_{top,c}$ [MPa]	20,33	20,33	20,33	20,33	20,33
$\sigma_{bot,c}$ [MPa]	19,28	19,28	19,28	19,28	19,28
$\epsilon_c$ [ $\mu\epsilon$ ]	587,14	587,20	587,21	587,19	587,14
$\epsilon_c$ [ $\mu\epsilon$ ]	556,72	556,77	556,79	556,77	556,72

Also in this case the strains are congruent with the load considered and the application of this load will generate a variability in the curve pressure-time and temperature time that have been showed in the previous paragraphs.

## 4.9. Application of traffic loads

In this section, it will be shown the three different load cases considered as a first assumption of test of the bridge deck. It is important to point out that the loads are considered specifically close to the area where the sensor are installed in order to evaluate the variations of stresses due to the loads. For this test it has been considered the static load generated by four trucks displaced in the middle of the span and a case of moving load of a truck in order to understand the stresses and strain read by the sensors.

### 4.9.1. Four trucks load-case

As mentioned before, the mass is converted in a force by multiplying it for the acceleration of gravity and then divided by the contact points between the wheel and the deck. This case has been considered directly applied on the slab in a test for the evaluation of the structural safeness of the bridge.

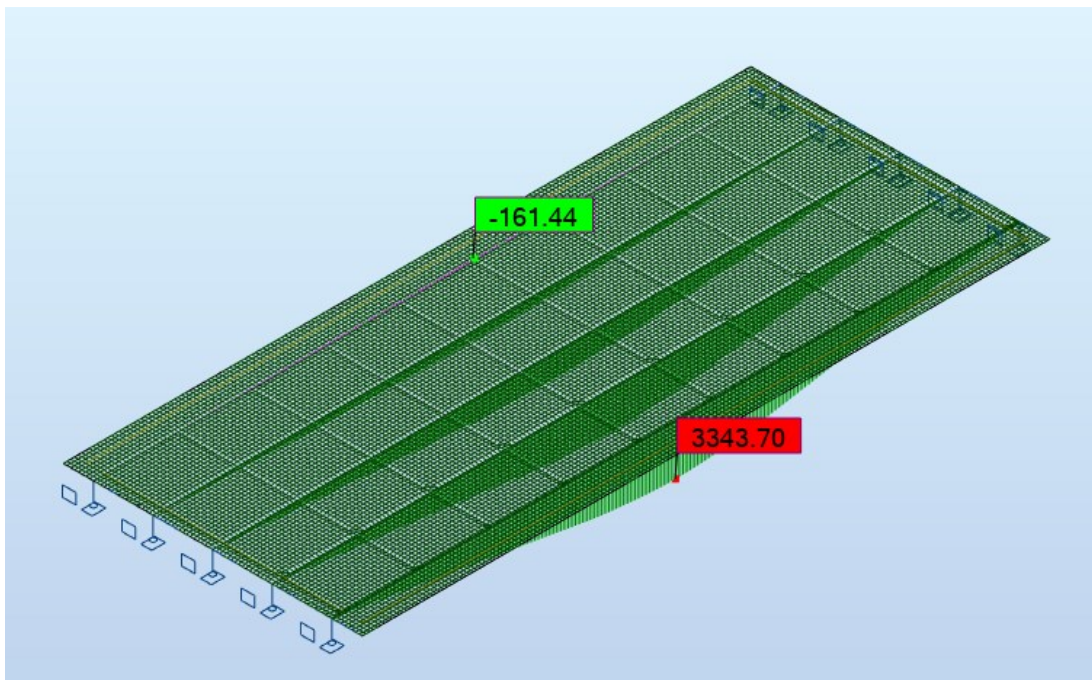


Figure 4.51: Static load of the trucks

As it is possible to see a static test of the bridge will generate a moment of 3340 kN in the middle of the span. This converted has been converted in stress as it has been calculated before.

The moment generated in the 5 points corresponding to the sensors' position are:

Table 4.37: Moment generated by the static load of four trucks

Moment values [kNm]		Axis position (m)				
		22,70	22,95	23,20	23,45	23,70
Beam number	23	3339,78	3342,74	3343,69	3342,72	3339,69
	64	2510,08	2513,35	2514,4	2513,33	2509,96

The stresses generated by the 4 trucks is shown below.

Table 4.38: Stresses and strain generated on the beam number 23

Beam number 23					
Distance [m]	22,70	22,95	23,20	23,45	23,70
$\sigma_{top, c}$ [MPa]	9,16	9,16	9,17	9,16	9,16
$\sigma_{bot, c}$ [MPa]	6,71	6,72	6,72	6,72	6,71
$\epsilon_c$ [ $\mu\epsilon$ ]	264,45	264,68	264,76	264,68	264,44
$\epsilon_c$ [ $\mu\epsilon$ ]	193,93	194,10	194,15	194,10	193,92

Table 4.39: Stresses and strain generated on the beam number 64

Beam number 64					
Distance [m]	22,70	22,95	23,20	23,45	23,70
$\sigma_{top, c}$ [MPa]	6,93	6,94	6,94	6,94	6,93
$\sigma_{bot, c}$ [MPa]	5,09	5,10	5,10	5,10	5,09
$\epsilon_c$ [ $\mu\epsilon$ ]	200,20	200,46	200,54	200,46	200,19
$\epsilon_c$ [ $\mu\epsilon$ ]	147,08	147,28	147,34	147,27	147,08

As seen in the previous paragraph the sensitivity of the system is of the order of a tens of a microstrain. The presence of 4 trucks in static position is easily detect by the sensors whose generate a straining of almost hundred time the variation detected. This give to the sensor a strong robustness, being able to easy detect the presence of the test load on the bridge. The strain generated by this load are important and it will be expected an important variation of the curves showed on the diagram before.

#### 4.9.2. Car Load-case

In order to take into account of the normal vehicle that run across the bridge it has been considered the case of a car positioned in the middle of the span. In this way it has been possible to evaluate the response expected by a normal load acting on the deck of the bridge. In order to consider this load it has been calculated the force generated by a car considering a distributed load acting on a surface equal to the print of the wheel. This last value it has been considered as a squared surface of  $0.4\text{ m}$  of length.

In the driving line number 3, it has been considered the displaying of  $Q_k = 4.9\text{ kN}$  acting on each wheel, considering the mass of the car of 2 ton, distributed on a surface of  $A = 0.16\text{ m}^2$ . This information has been tested on the model in order to evaluate the presence of the vehicle on the deck. The value obtained by the application of this load is equal to:

$$q_k = \frac{Q_k}{A} = \frac{4.91}{0.16} = 30\text{ kPa}$$

This is the scheme reported below.

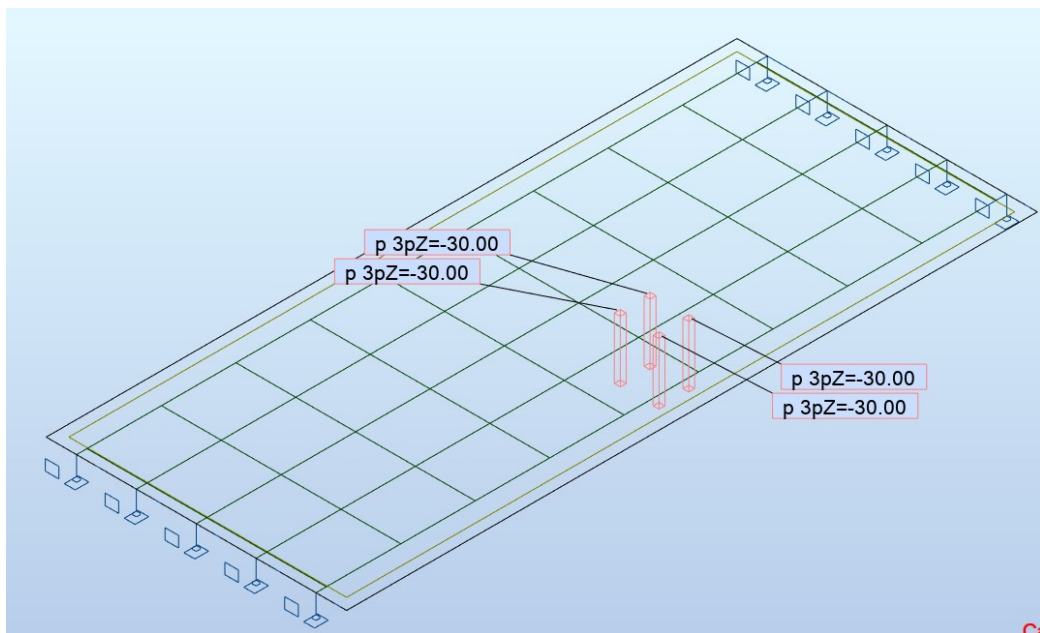


Figure 4.52: Scheme of the application of the car load

Once that this passage has been completed the next step is the extrapolation of the moment generated by this case and then the stresses and strain, following what has been done in the paragraph above. The moment obtained from the load application is shown below.

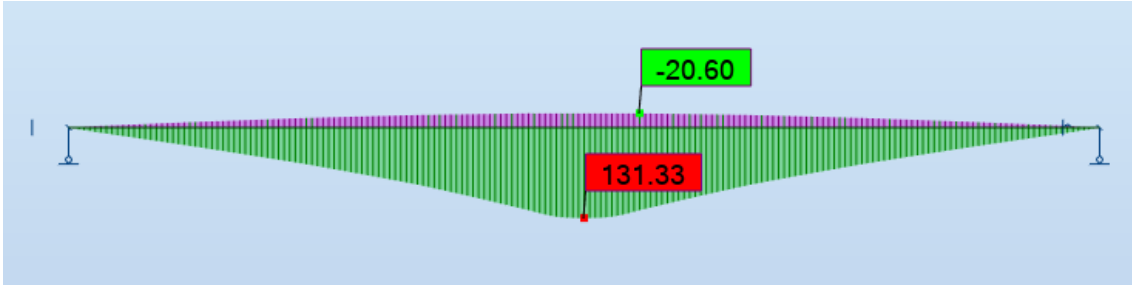


Figure 4.53: Moment generated by the car on the structure

The schematization of the moment is reported on the following table for the 5 points considered.

Table 4.40: Moment acting on the two beams considered from the moving load

Moment values [kNm]		Axis position (m)				
		22,70	22,95	23,20	23,45	23,70
Beam number	23	117,53	117,91	118,10	118,13	118,01
	64	69,40	69,56	69,65	69,67	69,62

This generates the following stresses and strain.

Table 4.41: Car load-case stresses and strain on beam 23

Beam number 23					
Distance [m]	22,70	22,95	23,20	23,45	23,70
$\sigma_{top, c}$ [MPa]	0,32	0,32	0,32	0,32	0,32
$\sigma_{bot, c}$ [MPa]	0,24	0,24	0,24	0,24	0,24
$\epsilon_c$ [ $\mu\epsilon$ ]	9,31	9,34	9,35	9,35	9,34
$\epsilon_c$ [ $\mu\epsilon$ ]	6,82	6,85	6,86	6,86	6,85

Table 4.42: Car load-case stresses and strain on beam 64

Beam number 64					
Distance [m]	22,70	22,95	23,20	23,45	23,70
$\sigma_{top, c}$ [MPa]	0,19	0,19	0,19	0,19	0,19
$\sigma_{bot, c}$ [MPa]	0,14	0,14	0,14	0,14	0,14
$\epsilon_c$ [ $\mu\epsilon$ ]	5,54	5,55	5,56	5,56	5,55
$\epsilon_c$ [ $\mu\epsilon$ ]	4,07	4,08	4,08	4,08	4,08

Once again, the strain generated by the passage of the vehicle calculated using the specification at the moment of the passage of the vehicle on the point where the sensors are displayed shows how, considering the performance of the system, the vehicle are easily detected. This means that it will be possible to monitor constantly the bridges and to understand which kind of vehicle passes on the structure according to the variation of pressure registered in the cavity. More important it could be exploring the deterioration of the bridge and the behaviour of the deck exposed to cycle loads. This can be deepened in the following study in which it will be explored the experimental values coming from the monitoring of the structure.



# Chapter 5

## 5. Conclusions

In this thesis it has been evaluated a field in strong developing during this year. The Structural Health Monitoring has seen an important upgrade that walk alongside with the technological development. It has been shown different instrument that nowadays are considered as classical devices to monitor the deformation, the stresses, the crack propagation, the corrosion etc. It has also been shown how the new technology, such as Fibre Optic device are largely diffusely nowadays due to their performances.

This thesis focused on the new technology developed by professor Tondolo [1] and the studies that followed up [12] [6]. In particular, it has been showed how the displacement of microscopic sensors inside a cavity dig into the steel reinforcement of the concrete allows the measurement of stresses and strain with an incredible degree of robustness and precision. In particular it has been shown how the improvement made in the last years has brought to a sensitivity of  $0.43 \mu\epsilon$  and then after the study conducted in this paper improved to a maximum value of  $0.22 \mu\epsilon$ . This value, although is slightly bigger than some of the fibre optical system and the strain gauge, it is extremely robust. More important, the data collected with this device can be obtained through a constant measurement and with a low-cost device which is a key feature in order to improve the diffusion of the monitoring of small and big structures and infrastructures. It is also important to highlight that this measurement can be detected also remotely, hence it does not require the presence of an operator in the field.

In the second part of this thesis, it has been shown how the installation phase has been performed on the bridge that has been objected of study. It has been described the procedure of installing of the rebars in the bridge and how this ease the mechanisms of casting in of the instrumented rebars. The images showed the exact position and how the cable has been displaced in the field in order to be linked to the data logger. Data logger which is the main component of the electronic and is able to send that information remotely in order to assure the monitoring.

The study conducted on the system brought to an improvement of the minimum sensitivity, which has been tested in the laboratory, and produced a value of  $0.22 \mu\epsilon$  and a general mean value on a rebar of  $0.31 \mu\epsilon$ . Following studies will be focus on the procedure and on the definition of a better scheme in order to improve this value and the characterization of the device.

It has been analysed the load-cases that are conformed to the final geometry of the bridge considering the different phase of construction of the bridge in order to understand the expected deformation, stresses and strains that each step will measure. Each phase has been evaluated and displayed in a model built with the software Robot Structural Analysis in order to extrapolate the solicitation and apply them into a computational sheet from where it has been evaluated the stresses produced and the straining of the rebar. This analysis compared to the sensitivity measurement defined above showed how every load-case can be detected easily by the system with a high margin of safeness. With future deepening of the study it will be possible to compare the result obtained from experimental acquisition with the theoretical values measured in this paper in order to understand the quality of the acquisition that have been made.

## References

- [1] F. Tondolo, "Embedded system for measurements of strain/stress in one-dimensional. Patent n° 102016000118077, Italy [Patent].," 2016.
- [2] H.-P. Chen and Y.-Q. Ni, *Structural Health Monitoring of Large Civil Engineering Structures*, John Wiley & Sons, 2018.
- [3] A. Zaki, H. K. Chai, D. G. Aggelis and N. Alver, "Non-Destructive Evaluation for Corrosion Monitoring in Concrete: A Review and Capability of Acoustic Emission Technique," *Sensor*, 5 August 2015.
- [4] U. B. Halabe, K. R. Maser and E. A. Kausel, "Condition Assessment of Reinforced Concrete Structures Using Electromagnetic Waves," 1993.
- [5] T. Nachazel, "What is a Strain Gauge and How Does it Work?," 2020. [Online]. Available: <https://www.michsci.com/what-is-a-strain-gauge/?cn-reloaded=1>.
- [6] F. N. Battistoni, "Structural Health Monitoring using low cost sensors: experimental and numerical study," 2018.
- [7] M. Enckell, "Structural Health Monitoring using Modern Sensor Technology- Long-term Monitoring of the New Årsta Railway Bridge," 2006.
- [8] S. Arar, "All about circuits," 2021. [Online]. Available: <https://passive-components.eu/linear-variable-differential-transformers-lvdt-explained/>.
- [9] H. M. Lee, J. M. Kim, K. Sho and H. S. Park, "A wireless vibrating wire sensor node for continuous structural health monitoring," *Smart Materials and Structures*, 2010.
- [10] J. M. Lopez-Higuera, L. R. Cobo, A. Q. Incera and A. Cobo, "Fiber Optic Sensor in Structural Health Monitoring," *Journal of Lightwave Technology*, p. 589, 15 February 2011.
- [11] J. Lopez-Higuera, A. Cobo, A. Quintela and F. Madruga, "Fiber optics in Structural Health Monitoring," *Proceedings of SPIE - The International Society for Optical Engineering*, 2010.
- [12] C. Bandinelli, "Structural Health Monitoring using innovative devices: numerical and experimental study," 2020.
- [13] X. Zhang, W. Wang, H. Chen, Y. Tang, Z. Ma and K. Wang, "Two-parameter Elliptical Fitting Method for Short-Cavity Fiber Fabry-Perot Sensor Interrogation," *Sensor*, 2019.

- [14] "Fibre Bragg grating sensor technology," [Online]. Available: <https://scaime.com/fibre-bragg-grating-technology>.
- [15] P. Corvaglia, A. Largo, M. Caponero and G. Maddaluno, "Development and Some Investigative Testing of Smart Structural FRP Devices with Embedded Fiber Optic Sensor for Health Monitoring of Civil Structures," *Structural Engineering*, 2010.
- [16] C. M. Monsberger, W. Lienhart and M. Hayden, "Distributed fiber optic sensing along driven ductile piles: Design, sensor installation and monitoring benefits," *Journal of Civil Structural Health Monitoring*, 2020.
- [17] M. Quiertant, A. Khadour, F. Baby and F. Toutlemonde, "Deformation Monitoring of Reinforced Bars with a Distributed Fibre Optic Sensor for the SHM of Reinforced Concrete Structures," *ResearchGate*, 2012.
- [18] Z. Wang, D. Chen, L. Zheng, L. Huo and G. Song, "Influence of Axial Load on Electromechanical Impedance (EMI) of Embedded Piezoceramic Transducers in Steel Fiber Concrete," *Sensors*, 2018.
- [19] A. Meoni, A. D'Alessandro, A. Downey, E. Garcia-Macias, M. Rallini, A. L. Materazzi, L. Torre, S. Laflamme, R. Castro-Triguero and F. Ubertini, "An Experimental Study on Static and Dynamic Strain Sensitivity of Embeddable Smart Concrete Sensors Doped with Carbon Nanotubes for SHM of Large Structures," *sensors*, 2018.
- [20] C. G. Karayannis, C. E. Chalioris, G. M. Angeli, N. A. Papadopoulos, M. J. Favvata and C. P. Providakis, "Experimental damage evaluation of reinforced concrete steel bars using piezoelectric sensors," *Elsevier*, 2015.
- [21] F. Tondolo, E. Matta, A. Quattrone and D. Sabia, "Experiment test on an RC beam equipped with embedded barometric pressure sensor for strain measurement," 2019.
- [22] European Committee for standardization, "Eurocode 2: Design of concrete structures - Part 1-1: General rules and rules for buildings," 2004.
- [23] s.n., "Silicon Designs Model 1010," 2012. [Online]. Available: <https://pdf.directindustry.com/pdf/silicon-designs/silicon-designs-model-1010/20945-306315.html>.
- [24] s.n., "Accelerometro Force Balance AFB," [Online]. Available: <https://www.solgeo.it/it/prodotti-per-monitoraggi-sismici-e-indagini-geofisiche/sensori-per-il-monitoraggio-dinamico/accelerometro-force-balance-afb>.

- [25] s.n., "SmartFBG," 2021. [Online]. Available:  
<https://www.smartfibres.com/products/smartfbg>.
- [26] s.n., "SmartPatch," 2021. [Online]. Available:  
<https://www.smartfibres.com/products/smartpatch>.
- [27] M. d. i. e. d. trasporto, Norme Tecniche per le Costruzioni, 2018.